Dissertation

submitted to the
Combined Faculties for the Natural Sciences
and for Mathematics
of the Ruperto-Carola University of Heidelberg, Germany
for the degree of
Doctor of Natural Sciences

Put forward by

Laura Victoria Klein

Born in: Neuss, Germany

Oral examination: 16.11.2023

Patient Risk–Minimizing Tube Current Modulation in X–Ray Computed Tomography

Referees: Prof. Dr. Jürgen Hesser

Prof. Dr. Marc Kachelrieß

Patient Risk–Minimizing Tube Current Modulation in X–Ray Computed Tomography

This dissertation proposes a patient–specific tube current modulation for computed tomography (CT) that minimizes the individual patient risk (riskTCM). Modern CT scanners use automatic exposure control (AEC) techniques including tube current modulation (TCM) to reduce the radiation dose delivered to the patient while maintaining image quality. Today's TCM implementations aim at minimizing the tube current–time (mAs) product as a surrogate for patient dose, which is why they are referred to as mAsTCM hereafter. However, the actual patient risk, e.g., in the form of risk measures such as the effective dose D_{eff} representing the sensitivity of individual organs with respect to ionizing radiation, is not taken into account. In order to be able to optimize the effective dose D_{eff} or another biologically meaningful measure, organ doses must be estimated before the actual CT scan in order to compute an optimized riskTCM curve. This can be achieved using a machine learning approach and based on these information, the new patient risk–minimizing TCM curve can be obtained. The proposed riskTCM algorithm was evaluated in a simulation study for circular scans and compared against the current gold standard method mAsTCM and to a constant tube current as well as an organ–specific tube current modulation technique. The results illustrate that all anatomical regions can benefit from riskTCM and a reduction of effective dose of up to 30 % can be expected compared to mAsTCM. Furthermore, riskTCM was extended to a spiral trajectory that is commonly used in clinical routine and initial measurements with phantoms have been performed. The introduction of riskTCM into clinical practice would only require a software update since almost all CT systems are already capable of modulating the tube current.

Patientenrisko-minimierende Röhrenstrommodulation für die Röntgen-Computertomographie

In dieser Dissertation wird eine patientenspezifische Röhrenstrommodulation für die Computertomographie (CT) entwickelt, welche das individuelle Patientenrisko minimiert (riskTCM). Moderne CT–Scanner verfügen über Techniken zur automatischen Belichtungssteuerung (AEC) einschließlich der Röhrenstrommodulation in Röhrenwinkel–Richtung (TCM), um die an den Patienten abgegebene Strahlungsdosis bei gleichbleibender Bildqualität zu verringern. Die heutigen TCM–Implementierungen zielen auf die Minimierung des Röhrenstrom–Zeit–Produkts (mAs) als approximatives Surrogat für die Patientendosis ab, weshalb sie im Folgenden als mAsTCM bezeichnet werden. Das tatsächliche Patientenrisiko, z. B. in Form von Risikomaßen wie der effektiven Dosis D_{eff}, wird dabei jedoch nicht berücksichtigt. Um die effektive Dosis D_{eff} oder ein anderes biologisch sinnvolles Dosis– oder Risikomaß optimieren zu können, müssen die Organdosen vor dem eigentlichen CT–Scan geschätzt werden. Dies kann mit Methoden des maschinellen Lernens erreicht werden. Anschließend kann die geschätzte effektive Dosis pro Röhrenwinkel berechnet werden, welche die Grundlage für die neue patientenspezifische risikominimierende Modulation darstellt. Der riskTCM–Algorithmus wurde in einer Simulationsstudie für Kreisscans evaluiert und gegen den gängigen TCM–Algorithmus mAsTCM und einen konstanten Strom sowie eine klinisch verfügbare organspezische Röhrenstrommodulation verglichen. Die Ergebnisse zeigen, dass alle anatomischen Regionen von riskTCM profitieren können und mit einer Reduktion der effektiven Dosis von bis zu 30 % verglichen zu mAsTCM, abhängig von Körperregion und Spannung, gerechnet werden kann. Anschließend wurde riskTCM noch auf eine Spiraltrajektorie erweitert und erste Messungen mit Phantomen wurden durchgeführt. Die Einführung von riskTCM in die Praxis wäre mit Software-Anpassungen möglich, da alle gängigen Systeme bereits fähig zur Modulation des Röhrenstroms sind.

Contents

List of Acronyms **IX**

List of Figures **XI**

List of Tables **XIII**

1 Introduction **1**

2 Fundamentals **5**
2.1 X–Ray Imaging and CT 5
2.1.1 X–Ray Generation 5
2.1.2 X–Ray Interaction with Matter 6
2.1.3 CT System Setup 8
2.1.4 CT Image Reconstruction 11
2.1.5 CT Image Representation 12
2.2 Dose Metrics in CT 14
2.2.1 Biological Interactions of Radiation 14
2.2.2 Physical Dose Quantities 15
2.2.3 CT Dose Index and Dose Length Product 15
2.2.4 Effective Dose 18
2.2.5 Size–Specific Dose Estimate 19
2.3 Tube Current Modulation Techniques 20
2.3.1 Standard Tube Current Modulation 20
2.3.2 Clinical Implementation of TCM Techniques 22
2.3.3 Organ–specific Tube Current Modulation 23

3 Material and Methods **25**
3.1 Conventional Tube Current Modulation 25
3.2 Risk–minimizing Tube Current Modulation 27
3.2.1 Basic Principle 27
3.2.2 Reconstruction from Topograms 28
3.2.3 Organ Segmentation 29
3.2.4 Dose–Per–View Estimation 29
3.2.5 riskTCM in Classical Reconstruction Algorithms 30

3.2.6 riskTCM in Modern Reconstruction Algorithms 30
3.3 Simulation Study 32
3.3.1 Scanner Geometry 32
3.3.2 Patient Population and Scan Protocols 34
3.4 Phantom Measurements 35

4 Results **39**
4.1 riskTCM as a Function of the Body Region 39
4.2 riskTCM as a Function of the Tube Voltage 46
4.3 riskTCM Compared to Organ–Specific TCM 48
4.4 Extension to Spiral Trajectory 50
4.5 Phantom Measurements 53

5 Discussion **55**
5.1 Potential Effective Dose Reduction with riskTCM 55
5.2 Limitations 57
5.3 Optimizing riskTCM 58
5.4 Dose Considerations 59

6 Summary and Outlook **61**

Bibliography **65**

List of Acronyms

C	Center
W	Width
a.p.	Anterior–posterior
AAPM	American Association of Physicists in Medicine
AEC	Automatic exposure control
BFGS	Broyden–Fletcher–Goldfarb–Shanno
CT	Computed tomography
CTDI	CT dose index
DDE	Deep dose estimation
DLP	Dose length product
DNA	Deoxyribonucleic acid
FBP	Filtered backprojection
FOM	Field of measurement
GPU	Graphics processing unit
ICRP	International Commission on Radiological Protection
KERMA	Kinetic energy released per unit mass
LAT	Lateral
mAsTCM	mAs–minimizing tube current modulation
MC	Monte Carlo
noTCM	Constant tube current
osTCM	Organ–specific tube current modulation

PMMA . . . . . Polymethyl methacrylate

RBE . . . . . Relative biological effectiveness

riskTCM . . . . . Risk–minimizing tube current modulation

ROI . . . . . Region of interest

SSDE . . . . . Size–specific dose estimate

TCM . . . . . Tube current modulation

List of Figures

2.1 Schematic of an x–ray source 6
2.2 Attenuation coefficient as function of photon energy for different interactions with matter 7
2.3 Setup and components of a CT system 9
2.4 CT scan trajectories 10
2.5 CT image reconstruction 11
2.6 Window/level settings in CT 13
2.7 Image of a CTDI phantom 16
2.8 Principle of tube current modulation 21
2.9 Principle of an organ–specific tube current modulation 23

3.1 Workflow of riskTCM 28
3.2 Color coding for the organ segmentations 29
3.3 XCare algorithm 34
3.4 Pictures of the phantom measurements. 36

4.1 Reconstructions for the different TCM methods for the head with arms 40
4.2 Reconstructions for the different TCM methods for the head w/o arms 41
4.3 Reconstructions for the different TCM methods for the neck 42
4.4 Reconstructions for the different TCM methods for the thorax 43
4.5 Reconstructions for the different TCM methods for the abdomen 44
4.6 Reconstructions for the different TCM methods for the pelvis 45
4.7 Reconstructions for the different TCM methods including osTCM for the first example patient 49
4.8 Reconstructions for the different TCM methods including osTCM for the second example patient 50
4.9 Coronal reconstructions for the spiral trajectory 51
4.10 Axial reconstructions for the spiral trajectory in the abdomen region . . 51
4.11 Axial reconstructions for the spiral trajectory in the shoulder region . . 52
4.12 Axial reconstructions for one example slice of the phantom measurements 54

List of Tables

2.1 CT–values for different tissues 13
2.2 Tissue weighting factors 18
2.3 D_{eff} conversion factors 19
2.4 AEC techniques provided by different manufacturers 22

4.1 D_{eff} values for all body regions for 70 kV 39
4.2 D_{eff} values for all TCM approaches given for all body regions and tube voltages. 47
4.3 D_{eff} and D_{Breast} values for a comparison between riskTCM and osTCM. 48

1 Introduction

The discovery of x–rays by Wilhelm Röntgen in 1895 [1] led to the development of several highly innovative technologies [2]. One of them is computed tomography (CT), invented by Hounsfield in the 1970s [3]. While the first CT scanner only provided a field of measurement (FOM) covering the human head and was prone to long examination times, today's CT scanners are able to acquire cross–sectional images of the entire body in only a few seconds, with a spatial resolution in the order of less than a millimeter, and provide high image quality with relatively low levels of radiation exposure [4], [5]. The basic physics of CT are described in chapter 2.1. Furthermore, a description of the setup of a CT system is given therein, and the basics of data reconstruction and interpretation of the resulting images are described.

Since the exposure of patients to ionizing radiation remains a concern to public health [6], a variety of methods have been developed to reduce the administered radiation dose in CT examinations. Besides iterative reconstruction methods [7]–[17], deep-learning based reconstruction methods [18]–[26], the introduction of adaptive filters [27], [28], improved prefilters [29]–[34] or entirely new detector technologies such as photon–counting CT [35]–[42], a major improvement for CT examinations are automatic exposure control (AEC) techniques [43]–[48]. These include automatic tube current and tube voltage selection as well as tube current modulation (TCM) techniques in angular and longitudinal directions. I.e., the x–ray tube is automatically controlled in a way to minimize radiation exposure while maintaining image quality. Usually, the used exposure parameters are chosen more or less automatically, e.g., with regard to a standard patient, or based on topograms that are acquired prior to any CT acquisition. The aim of TCM thereby is either to improve image quality while maintaining radiation dose or, conversely, to reduce radiation dose while maintaining image quality in terms of noise. Using TCM results in a much more homogeneous noise texture and therefore reduces noise–induced streak artifacts and thereby improves diagnostic confidence in the resulting reconstructions. In general, TCM takes into account anatomical inhomogeneities in angular or longitudinal direction, i.e., when the scanned region is highly variable in angular direction (α-direction) or in the longitudinal direction (z-direction). This is the case, for example, when scanning from the neck to the shoulders or when comparing lateral and anterior–posterior (a.p.) projections in the shoulder region. In other words, these techniques modulate the tube current as a function of attenuation. The longitudinal dependence is typically chosen empirically

by the manufacturers to avoid excessive tube power requirements for obese patients and to accommodate the need for less image noise for paediatric patients due to their small anatomical details. Since today's TCM implementations aim to minimize the tube current–time (mAs) product, they will therefore be referred to as mAs–minimizing tube current modulation (mAsTCM). The use of mAsTCM has been shown to reduce the total mAs–value by up to 60 %, depending on the body region and scan protocol, compared to a scan with no modulation of the tube current [49]. This will be denoted as constant tube current (noTCM) in the following. The consideration of tube current is also a very simple but highly approximate surrogate for the patient dose. However, it does not take into account the actual radiation sensitivity of different organs or anatomical structures in the FOM since the total mAs–value is minimized instead of minimizing the radiation risk. In most cases, this will also result in a reduction of effective dose and therefore risk, but this is not necessarily the case and cannot be guaranteed. A detailed description of state–of–the–art TCM methods will be provided in chapters 2.3 and 3.1.

Although many improvements have been made since the initial introduction of CT systems, the ionising radiation used in CT imaging remains a concern given its potential to induce health risks [50]–[54]. Common dose metrics to quantify this risk in CT imaging are described in chapter 2.2. Many are based solely on physical quantities but there are also other dose measures that are patient–specific. The effects of ionising radiation on the human body, including the risk of inducing cancer, have been extensively studied since 1945 [55], and the International Commission on Radiological Protection (ICRP) provides reference tissue weighting factors that describe the relative risk of radiation inducing cancer in individual organs. Using the ICRP weighting factors, it is possible to estimate the effective dose as the weighted sum of all organs and relate it to the stochastic health risk for the whole body. Hence, effective dose is often used to quantify the patient–specific risk resulting following CT examinations in clinical practice.

The importance of dose reduction is also evident when considering the number of CT scans and collective doses in Germany. The 2019 annual report published by the "Federal Ministry for the Environment, Nature Conservation, Nuclear Safety and Consumer Protection" provides insights into the development of x–ray diagnostics and the dose received by German residents [56]. The average effective dose a person receives from x–ray examinations is about 1.6 mSv on average per inhabitant in Germany. In 2016, computed tomography accounted for 9 % of x–ray–based diagnostic examinations. However, its share in the collective effective dose was 67 %. In general, the average effective dose per inhabitant in Germany due to x–ray diagnostics is increasing. One reason is that the number of CT scans is also increasing. From 2007 to 2016, the number of CT examinations increased by about 45 %. The increase of the effective dose only from CT scans, on the other hand, was by about 30 %, which indicates that the effective dose per CT scan is slowly decreasing.

The aim of this thesis is to use the effective dose as a patient–specific radiation risk measure and to define a new tube current modulation method that overcomes the drawbacks of current approaches. This new risk–minimizing tube current modulation

(riskTCM) method shall reduce the effective dose or some other meaningful biologically motivated parameter and thus provides a way to reduce the risk of radiation–induced cancer and other undesirable side effects caused by CT examinations while maintaining the high image quality achieved when using other state–of–the–art TCM methods. In chapter 3, riskTCM and all required methods and algorithms are introduced. Furthermore, this chapter describes methods and studies that were conducted in the scope of this thesis to evaluate the potential dose reduction achievable by this method. Chapter 4 presents the results obtained using this new method. In particular, the potential effective dose reduction of riskTCM compared to the case of constant tube current and a conventional gold–standard tube current modulation, i.e., mAsTCM, is evaluated for different anatomical regions from the pelvis to the head. A possible dependence of effective dose reduction on chosen tube voltage is investigated and riskTCM is also compared with a clinically available organ–specific tube current modulation (osTCM) technique in terms of effective dose and dose reduction to the female breast. In a consecutive step, a first evaluation of an extension of riskTCM to a spiral trajectory, which is more common in clinical practice, as well as initial measurements with phantoms, are presented. Chapter 5 discusses the results which are then summarized in chapter 6. An outlook on possible further research is also provided in chapter 6.

2 Fundamentals

2.1 X–Ray Imaging and CT

2.1.1 X–Ray Generation

X–rays inside a CT system are typically generated using dedicated x–ray tubes. Inside such an evacuated tube, a cathode, usually made of tungsten, is heated and emits electrons. These electrons form the so–called tube current I and are accelerated towards an anode by the application of the tube voltage U. The tube voltage is typically chosen between around 70 kV to 150 kV in clinical CT systems. The electrons hit the anode which is also typically composed of tungsten and the interaction of the electrons with the anode causes the emission of bremsstrahlung [57]. However, only about 1 % of the electrons' energy is converted into bremsstrahlung though. The rest results in heating of the anode and hence cooling the anode is therefore of crucial importance [58]. One approach to achieve this is the rotation of the anode. The anode is constantly rotating to avoid irradiating only one spot of it. Furthermore, the tube is also surrounded by a cooling medium. Historically, the cooling medium was not in direct contact with the anode which limited the performance and resulted in dead–times of the system. Today, the tubes in CT systems are designed such that the rotating mechanics and large parts of the anode are directly coupled to a cooling medium, e.g., oil, allowing for much higher tube powers and an improved heat dissipation [59]. The design of such a modern x–ray tube is sketched in figure 2.1. A bremsstrahlung photon emitted from the anode can have the maximum energy of the applied tube voltage times the electric charge of the electron $e = 1.602 \cdot 10^{-19}$ C, i.e., the maximum energy is given as $e \cdot U$. The bremsstrahlung spectrum is continuous up to the maximum energy, although the spectrum itself shows some additional characteristic peaks. These peaks are the result of accelerated electrons colliding with electrons from the inner shells of the atoms of the anode material. Such a shell electron might be ejected causing an electron from an outer shell to take its place in the inner shell since this state is energetically favorable. This results in the emission of photons with a characteristic energy. The most prominent peaks are the $K_{\alpha,1}$ and $K_{\alpha,2}$ peaks. Here, K is the shell number. The K–shell is the closest to the nucleus. The subscript α means that the electron has moved up from the second closest shell, namely the L–shell, while β would indicate a transition from the third or M–shell. The additional numerical index describes the involved sub–shell and explains small energetic differences among the emitted photons.

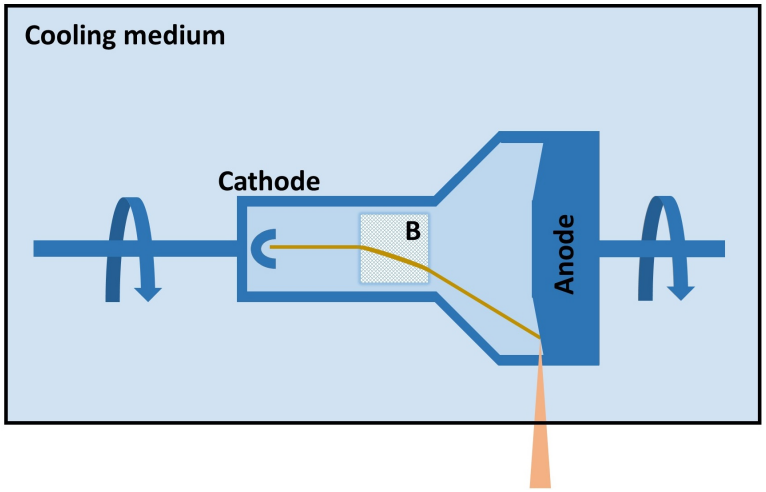

Figure 2.1: Schematic of an x–ray source. Electrons are emitted from the cathode through thermionic emission and are deflected through the magnetic field B. The electron beam hits the anode and bremsstrahlung in form of a continuous photon spectrum and characteristic x–rays is emitted. The evacuated tube is placed inside of a cooling medium to which the anode has direct contact. Additionally, the anode rotates to avoid hitting the same focal spot which would make cooling more difficult.

2.1.2 X–Ray Interaction with Matter

Depending on the energy of the x–ray photons, different mechanisms dominate their interaction with matter. In general, there are three main interactions that are relevant for the photon energies in clinical CT which are at most 150 keV. These are Rayleigh scattering, the photoelectric effect and Compton scattering. Figure 2.2 illustrates all interaction probabilities as a function of photon energy E. The effect of pair production is neglected since it requires photon energies of more than 1022 keV [60]. The total attenuation coefficient $\mu(E)$ describing all possible interactions is thus composed of the attenuation coefficient contributions of these three interaction processes, i.e.,

$$\mu(E) = \mu_{\mathrm{RS}} + \mu_{\mathrm{PE}} + \mu_{\mathrm{CS}}. \tag{2.1}$$

Therein, μ_{RS} is the attenuation coefficient of the Rayleigh scattering, μ_{PE} of the photoelectric effect, and μ_{CS} of Compton scattering. Alternatively, the attenuation coefficient can also be described by the following formula

$$\mu(E) = \frac{\rho N_{\mathrm{A}}}{A}\sigma(E). \tag{2.2}$$

Therein, ρ is the mass density of the material, A is the atomic mass, N_A is the Avogadro–number and σ is the cross–section describing the probability of interaction. In the following, these three main interactions and their cross–sections, and thus their contributions to the photon energy–dependent attenuation coefficient, are briefly described.

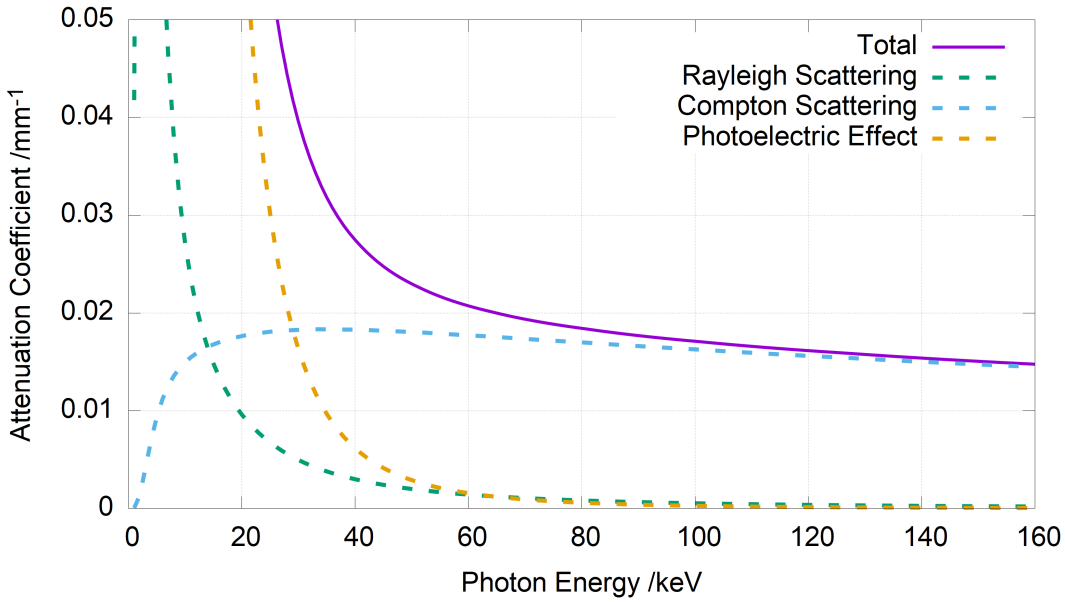

Figure 2.2: Contribution of the photon interactions with matter to the attenuation coefficient as function of photon energy. In particular, the photoelectric effect, Compton, and Rayleigh scattering are displayed as well as the total attenuation coefficient composed of all three effects.

Rayleigh Scattering

Rayleigh scattering is also called elastic scattering because the photon scatters off an atom without losing any of its energy [61]–[64]. Only its trajectory is changed by a small angle. This happens because the mass of the atom is much larger than that of the photon, so the momentum of the atom changes only slightly during the collision. The cross–section is given as

$$\sigma_{\mathrm{RS}}(E) \propto \frac{Z^2}{E^2} \tag{2.3}$$

where Z describes the atomic number and E the energy of the incident photon [65]. Rayleigh scattering plays a very small role in the total attenuation coefficient $\mu(E)$, as can be seen in figure 2.2, and could therefore also be neglected. Since the photon does not lose energy during the interaction, Rayleigh scattering does not contribute to the patient dose but might be relevant when considering scattered radiation.

Photoelectric Effect

The photoelectric effect describes the absorption of a photon by the electron of an inner shell [66]. If the energy of the photon exceeds the binding energy of the electron, the

electron will leave the atom, creating a vacancy in the inner shell. An electron from an outer shell takes its place since the resulting state is energetically more favorable. Consequently, a photon with the excess energy is released. The cross–section of the photoelectric effect is

$$\sigma_{\mathrm{PE}}(E) \propto \frac{Z^n}{E^m} \tag{2.4}$$

wherein n is about 4 and m about 3 for 100 keV [65]. Since the dependence of the cross section on the atomic number is very high, it is most pronounced for high–Z materials such as lead with Z = 82. Therefore, the absorption of high–Z materials is very high. The dependence on the inverse of the photon energy E results in the photoelectric effect being most prominent in photons with lower energies.

Compton Scattering

Compton scattering is the inelastic scattering of photons with electrons from the outer shells of atoms [67]. Kinetic energy is transferred from the photon to the electron causing the electron to be emitted from the atom and the photon to lose part of its energy. The corresponding cross–section is given as

$$\sigma_{\mathrm{CS}}(E) \propto \frac{Z}{E^m} \tag{2.5}$$

wherein m is between 0 and 1, resulting in a low energy and material dependence [65]. To prevent Compton scattering from affecting image quality, detectors are equipped with anti–scatter grids.

Beer-Lambert Attenuation Law

The Lambert–Beer Law of Attenuation describes the number of photons N after an initial number of photons N_0 has travelled the length L through a material with the attenuation coefficient μ [68], [69]. In particular, the number of photons decreases exponentially via

$$N(L) = N_0 \cdot e^{-\mu \cdot L}. \tag{2.6}$$

Equation (2.6) is valid for monochromatic attenuation. In reality, photons of different energies are emitted from the tube. Since the attenuation coefficient is also energy–dependent, the formula becomes

$$N(E, L) = N_0(E) \cdot e^{-\mu(E) \cdot L}. \tag{2.7}$$

2.1.3 CT System Setup

In figure 2.3 a sketch of a CT system can be seen. The main components of a CT system are the gantry with the x–ray tube mounted on one side and the x–ray detector

on the other. The gantry rotates around the patient. The distance between source and detector is usually about 50 cm to 70 cm in conventional clinical CT systems. The rotation time t_{rot} of the gantry is about 0.25 s to 1 s per revolution which poses a multitude of technical challenges. The fast rotation time of the gantry results in very high centrifugal acceleration. For example, for a diameter of 60 cm and a rotation time t_{rot} of 1 s, the centrifugal acceleration equals about 2.4 times the gravitational acceleration g, whereas for $t_{\text{rot}} = 0.25$ s it is about $38.6g$. The CT components which typically weigh several hundred kilograms have to withstand such accelerations and forces to maintain equipment and, more importantly, patient safety [70]. CT systems

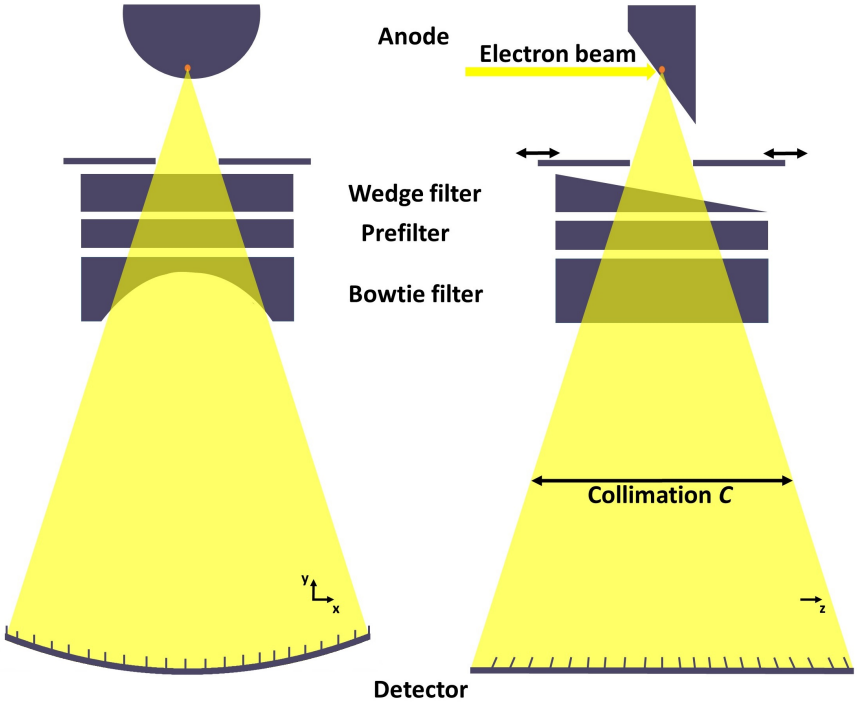

Figure 2.3: Setup of a CT system including the x–ray source with its anode, prefilter and bowtie filter as well as the detector.

today typically use a cone–beam geometry. The detector consists of many rows and columns. The columns are aligned in lateral direction to form a FOM that covers the entire patient. The longitudinal– or z–coverage is about 32 to 64 rows, each with a size of about 0.2 mm to 0.6 mm in the center of rotation (isocenter) for standard CT systems. These values differ between older and newer systems and across different vendors [4]. During an examination, the patient is positioned on a table with adjustable height. This is important for placing the patient in the center of the FOM and to ensure the best possible image quality and dose distribution. Furthermore, the table can be translated in longitudinal direction. This is an important feature in clinical practice since the detector usually does not cover the entire region of interest (ROI) in longitudinal direction and hence the patient has to be moved during the measurement. To overcome this drawback,

scans are either performed as a sequence scan consisting of several circle scans with intermediate table motions or as spiral scans with a continuous table motion during image acquisition [70]. Particularly in case of the circular scan mode, the table does not move during image acquisition. I.e., data are acquired using a circular trajectory. In a next step the table is moved, followed by data acquisition, followed by table motion and so forth until the desired scan range is achieved. One of the drawbacks of this approach are motion artifacts, e.g., due to breathing, caused by prolonged scan times and issues of patient comfort due to the stop–and–go approach. Hence, usually spiral scans are performed in clinical practice. In case of such a spiral scan, the table moves continuously in longitudinal direction while the tube rotates around the patient [71]. For spiral scans, a pitch value p is defined, which describes the table feed per 360° gantry rotation divided by the beam collimation in the isocenter, i.e.,

$$p = \frac{d}{C} \tag{2.8}$$

with C being the collimation and d the table feed. Figure 2.4 illustrates the difference between sequence and spiral scan. Between the x–ray tube and the patient, several

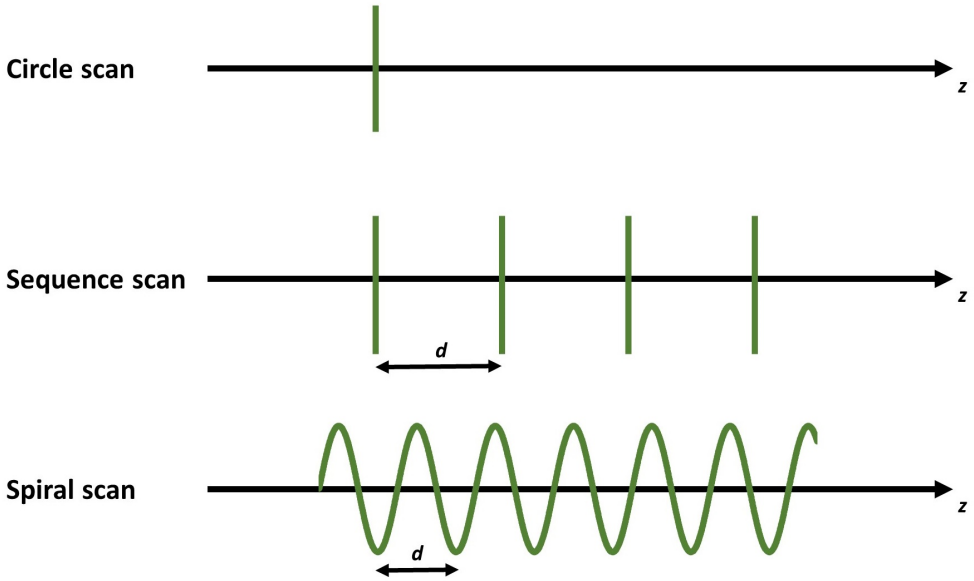

Figure 2.4: Different CT scan trajectories used in clinical CT. The spiral trajectory is the most commonly used trajectory while circular and sequence scans are only performed in special applications.

prefilters are usually placed. These prefilters, e.g., made of aluminium, aim at absorbing low energy photons before they can interact with the patient. These low–energy photons would not be able to penetrate the patient and reach the detector, but would rather be absorbed in the patient without contributing to the image, hence, only contributing to the patient dose. Therefore, all modern CT systems use such prefilters to optimize the dose delivered to the patient.

2.1.4 CT Image Reconstruction

Clinical CT systems typically use a fan–beam or cone–beam geometry and the scan is performed using a spiral trajectory. Data reconstruction is thus complex. Therefore, the basic of image reconstruction will be detailed only using a 2D parallel beam geometry in the following [70], [72]. Figure 2.5 illustrates how such parallel beams are parameterized.

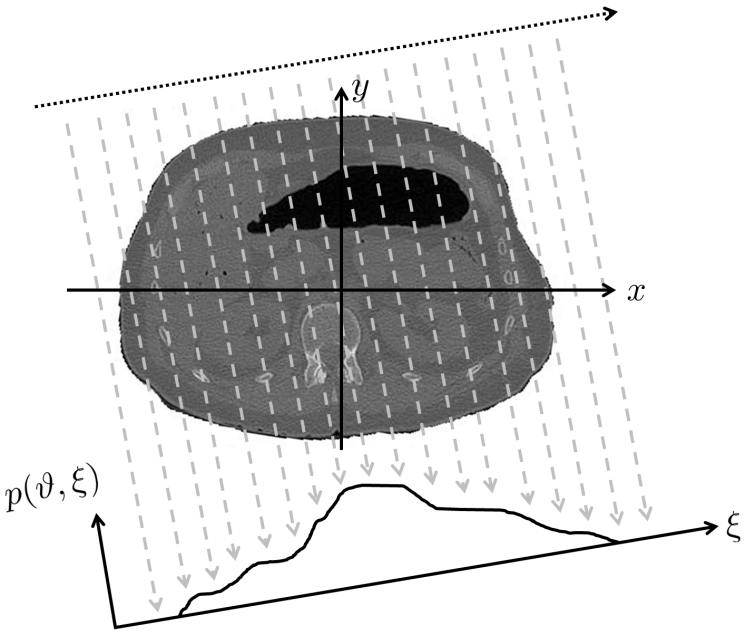

Figure 2.5: Principle of CT image acquisition and reconstruction for a parallel beam geometry. The source emits a pencil beam and is shifted in lateral direction to acquire a single detector image, followed by an incremental rotation and an acquisition of the next projection.

The variable ϑ describes the angle to the y–axis while ξ is the distance to the center of rotation with $\xi = x\cos(\vartheta) + x\sin(\vartheta)$ being a line through the patient. The measurement or projection $p(\vartheta, \xi)$ can be described by the following equation

$$p(\vartheta, \xi) = \int dxdyf(x, y)\delta(x\cos(\vartheta) + y\sin(\vartheta) - \xi). \tag{2.9}$$

Here, $f(x, y)$ represents the desired image, e.g., the distribution of the linear attenuation coefficient of a patient, and δ describes the Dirac delta distribution. I.e., equation (2.9) describes the line integral through the function $f(x, y)$ and corresponds to the measurement of the considered parallel beam CT system. To obtain the desired image $f(x, y)$, this equation has to be inverted. To do so, first, a Fourier transform $\mathcal{F}$ of p has to be carried out with respect to ξ. I.e.,

$$P(\vartheta, u) = (\mathcal{F}p)(\vartheta, \xi) \tag{2.10}$$

$$= \int d\xi \int dxdyf(x, y)\delta(x\cos(\vartheta) + y\sin(\vartheta) - \xi)e^{-2\pi iu\xi}. \tag{2.11}$$

Since the delta distribution ensures that $\xi = x\cos(\vartheta) + x\sin(\theta)$, it follows that

$$P(\vartheta, u) = \int dxdy f(x,y) e^{-2\pi i u(x\cos(\vartheta)+y\sin(\vartheta))} \tag{2.12}$$

$$= F(u\cos(\vartheta), u\sin(\vartheta)). \tag{2.13}$$

This relates the Fourier transforms of f and p and is also known as the Fourier–Slice theorem. The image f is now given by

$$f(x,y) = \int_0^\pi d\vartheta \int_\infty^{-\infty} du P(\vartheta, u)\,|u|\, e^{2\pi i u(x\cos(\vartheta)+y\sin(\vartheta))}. \tag{2.14}$$

Herein, $|\,u\,|$ follows from the conversion of polar to cartesian coordinates and the Jacobian used in this conversion. Since $P(\vartheta, u)\,|u|$ is a product in frequency domain, it can be reformulated as convolution in spatial domain, i.e.,

$$f(x,y) = \int_0^\pi d\vartheta p(\vartheta, \xi) * k(\xi). \tag{2.15}$$

The function $k(\xi)$ is also called reconstruction kernel and is given as

$$k(\xi) = \mathcal{F}^{-1}K(u) = \int du\,|u|\, e^{2\pi u\xi} = -\frac{1}{2\pi^2\xi^2} \tag{2.16}$$

in spatial domain. Hence, image reconstruction generally consists of two parts: a filtering of the acquired rawdata with a kernel $k(\xi)$ and a backprojection denoted by the integral over ϑ. Therefore, this type of image reconstruction is also referred to as filtered backprojection (FBP).

2.1.5 CT Image Representation

In case of the reconstruction method described in the previous section, the image $f(x,y)$ would represent the distribution of the linear attenuation coefficient. However, in clinical practice, images do not show attenuation coefficient values but rather CT–values measured in Hounsfield Units (HU) [73]. CT–values are obtained from attenuation values as

$$\text{CT–value} = \frac{\mu_{\text{tissue}} - \mu_{\text{water}}}{\mu_{\text{water}}} \cdot 1000\,\text{HU}, \tag{2.17}$$

wherein μ_{water} is the linear attenuation coefficient of water and μ_{tissue} is the actual measured attenuation coefficient. Considering this equation, two fix points can be identified. If we use $\mu_{\text{tissue}} = 0\,\text{mm}^{-1}$, approximately corresponding to the attenuation of air, we find a fix point at $-1000\,\text{HU}$. Similarly, if we use $\mu_{\text{tissue}} = \mu_{\text{water}}$, we find the second fix point as $0\,\text{HU}$.

I.e., the CT–values of water and air are fixed in every well–calibrated CT scanner [70], [74]. Soft tissues, such as the liver, are very similar to water but are slightly denser and therefore have a CT–value between $40\,\text{HU}$ and $70\,\text{HU}$. Bones highly absorb radiation and therefore have high CT–values of up to $2000\,\text{HU}$. The lungs consist of a large

Table 2.1: CT–values for different tissues.

Tissue	CT–value
Air	−1000 HU
Lungs	−900 HU to −500 HU
Fat	−100 HU to −70 HU
Water	0 HU
Kidneys	20 HU to 40 HU
Pancreas	20 HU to 50 HU
Blood	30 HU to 60 HU
Liver	40 HU to 70 HU
Bones (spongious)	70 HU to 350 HU
bones (cortical)	350 HU to 2000 HU

amount of air and only small fractions of soft tissue and therefore have CT–values around −500 HU and −900 HU. Table 2.1 shows more CT–values for different tissues. The range of possible CT–values is vast, however, the human eye cannot distinguish more than about 100 different shades of gray at the same time. This drawback is overcome by windowing which is an important diagnostic tool. In particular, two parameters can be adjusted in almost every clinical image viewer, the center (C) and the width (W) of the displayed gray values. For example, a center of $C = 0$ HU and $W = 1000$ HU would display all gray values from −500 HU to 500 HU with different shades of gray. Every value below −500 HU would be displayed as black and every value above 500 HU would be white.

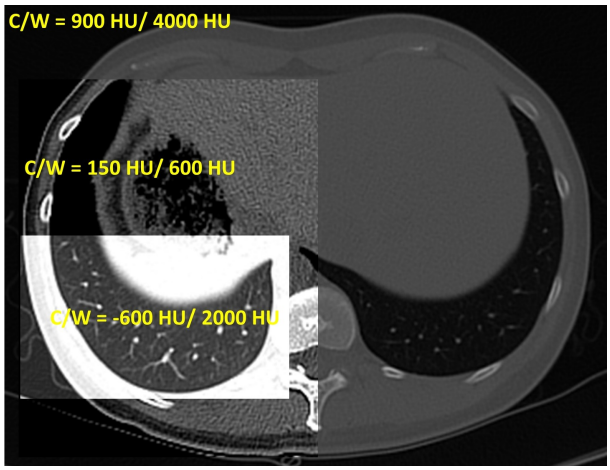

Figure 2.6: Different examples for window/level settings in CT. A typical lung window ($C = -600$ HU, $W = 1200$ HU), a window for soft tissue ($C = 150$ HU, $W = 600$ HU) and bones ($C = 900$ HU, $W = 4000$ HU) are shown.

Since soft tissue CT–values are all quite similar, a narrow window is best suited for diagnostics of such structures. For example, a setting to show a possible liver pathology might be $C = 40\,\mathrm{HU}, W = 200\,\mathrm{HU}$. For a bone or lung window on the other hand, the width should be wide. For bones, a setting of $C = 450\,\mathrm{HU}, W = 1500\,\mathrm{HU}$, and for the lungs, a setting of $C = -600\,\mathrm{HU}, W = 1200\,\mathrm{HU}$ could be chosen. An example of different window settings is shown in figure 2.6.

2.2 Dose Metrics in CT

2.2.1 Biological Interactions of Radiation

Ionisation in water or tissue is possible at photon energies of 30 eV and above [75]. This means that x–ray radiation in computed tomography is potentially ionising and can therefore have harmful effects on human tissue. The number of radiation–induced ionisation processes in the human body is rather high. For example, the annual dose to an individual in developed countries is about 2.4 mSv. The total number of ion pairs induced in a standard human body per year by this natural radiation exposure is about 3.6×10^{16}. This is particularly serious when ion pairs are formed in the cellular nucleus since this might damage the deoxyribonucleic acid (DNA) and might lead to gene mutation, and in some cases, the development of cancer. However, this is a statistical process and can only be assessed for larger cohorts of patients. Damage to the cell's organelles, on the other hand, is only serious when very high dose levels of radiation damage all organelles at the same time, shutting down the cell's metabolism. Irreversible damage to cell membranes leads to the breakdown of the cell nucleus or cell, followed by rapid cell death.

For low levels of radiation below 0.25 Gy, no immediate effects can be observed. However, long–term effects are possible. The stochastic radiation risk is highly age–dependant with children having a life–time risk to develop cancer that is about 3 times higher compared to middle–aged patients that undergo the same examinations. Similarly, the radiation–induced cancer mortality is lower for older patients due to their shorter life expectancy.

The cascade of interactions of radiation with tissue starts with the physical interactions. This happens in a time frame of about 10^{-16} s to 10^{-13} s. These interactions result in the ionisation or excitation of atoms and molecules such as nucleic acids or proteins. The next stage is the physical–chemical stage which lasts from 10^{-13} s to 10^{-2} s. Therein, the absorbed energy of the radiation is distributed. The thermodynamic energy balance dominates. Secondary reactions processes also play a role here. Bio–molecules can be altered or even destroyed by breaking or splitting off parts of molecules. The final biological phase lasts from 10^{-2} s to several years or decades. Initially, repair mechanisms for DNA damage take place. Changes that cannot be repaired, or are not repaired correctly, can affect cell metabolism or the genetic coding resulting to, for example, in mutation of genes, cell death after cell division(s) or cancer.

2.2.2 Physical Dose Quantities

The fundamental physical dose measure is the absorbed dose

$$D_{\text{abs}} = \frac{dE}{dm} = \frac{dE}{\rho dV} \tag{2.18}$$

with the unit Gray given as $1\,\text{Gy} = 1\,\frac{\text{J}}{\text{kg}}$. Further, dE describes the average energy deposited by ionising radiation in matter of mass dm [70]. Another important measure is the kinetic energy released per unit mass (KERMA). It is defined as being the sum of the kinetic energy E_{tr} of each charged secondary particle resulting from indirect ionising particles such as photons divided per mass. I.e.,

$$K = \frac{dE_{\text{tr}}}{dm}. \tag{2.19}$$

The unit is also Gray. In case of lower energies, KERMA is similar to absorbed dose. However in case of higher energies, KERMA is higher compared to the absorbed dose since high energetic secondary particles might escape the ROI before depositing their energy.

2.2.3 CT Dose Index and Dose Length Product

The CT dose index (CTDI) was introduced to allow for a comparison of the radiation output across different CT scanners using a reference phantom [76]–[78]. The reference phantom is a cylinder made of polymethyl methacrylate (PMMA). It is available in two sizes depending on the body region to be scanned. For head and paediatric examinations, the reference phantom has a diameter of 16 cm, otherwise the diameter is 32 cm. Figure 2.7 shows such a phantom. The phantom contains several drillings that can be used to place pencil ionisation chambers for radiation measurements. In particular, one chamber is placed in the center of the patient while four chambers are placed in the periphery. Since a chamber has a length of 100 mm the CTDI–value measured for such a chamber is called CTDI_{100}. It is defined as

$$\text{CTDI}_{100} = \frac{1}{C}\int_{-50\,\text{mm}}^{+50\,\text{mm}} dz\, D(z) \tag{2.20}$$

with C being the collimation. The CTDI–values are typically given in mGy. CTDI_{100}–values can be used to calculate the weighted CTDI (CTDI_{w}) which describes the average radiation dose across an axial section of the CTDI phantom. In particular, it is given by

$$\text{CTDI}_{\text{w}} = \frac{1}{3}\text{CTDI}_{100,\text{center}} + \frac{2}{3}\text{CTDI}_{100,\text{periphery}} \tag{2.21}$$

where $\text{CTDI}_{100,\text{center}}$ refers to the measurement at the center of the phantom and $\text{CTDI}_{100,\text{periphery}}$ refers to the measurement at the periphery of the CTDI phantom. This equation can be derived under two assumptions [79]. First, that the absorbed dose

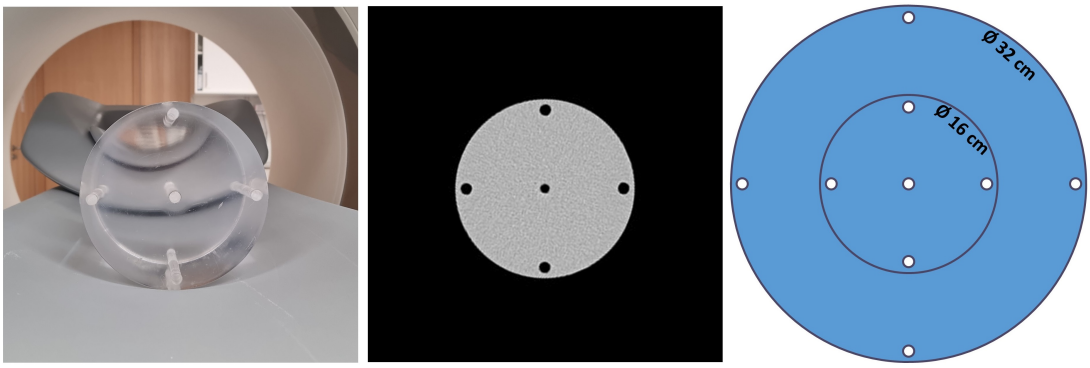

Figure 2.7: Left: Picture of a $CTDI_{16\,cm}$ phantom. Middle: CT image of the $CTDI_{16\,cm}$ phantom ($C = 0\,HU, W = 500\,HU$) Right: Scheme of a CTDI phantom. For the pencil chambers, one drill hole is placed in the middle of the phantom and four bores are on the periphery of the 32 cm diameter or 16 cm diameter phantom.

is linearly dependent on the radial position and, second, that it is independent of the angular position. The total energy deposited in a homogeneous disk segment of the phantom would be

$$E = \int_m \frac{dE}{dm}. \tag{2.22}$$

The energy absorbed in an object is given by

$$D = \frac{E}{m} \tag{2.23}$$

where E describes the deposited energy from ionizing radiation and m the mass of the object. It therefore follows that

$$E = \int_m D(\boldsymbol{x})dm = \int_V D(\boldsymbol{x})\rho dV \tag{2.24}$$

since for a disk the mass m is proportional to the volume V times the density ρ. Under the assumption that $D(\boldsymbol{x})$ is rotationally invariant, it further follows that

$$E = \int_0^R \int_0^{2\pi} D(r)\rho\Delta z r dr d\Theta = 2\pi\Delta z \int_0^R D(r) r dr \tag{2.25}$$

Because of the assumption that the absorbed dose is linearly dependent on the radial location r, D can be described as a linear function of r, i.e.,

$$D(r) = ar + b. \tag{2.26}$$

By knowing that the volume V of the disk equals the squared–radius R times the length Δz, it follows for the deposited energy that

$$E = \pi\rho R^2\Delta z(\frac{2}{3}aR + b). \tag{2.27}$$

For the average dose D_{avg} this yields

$$D_{\text{avg}} = \frac{2}{3}aR + b. \tag{2.28}$$

The two parameters a and b can be calculated by investigating the two measurement positions at the center $r = 0$ and the periphery $r = R$. It follows

$$D(0) = b \tag{2.29}$$

and

$$D(R) = aR + b. \tag{2.30}$$

I.e., a can be described by

$$a = \frac{D(R) - D(0)}{R}. \tag{2.31}$$

Then the result for D_{avg} can be described as

$$D_{\text{avg}} = \frac{2}{3}\frac{D(R) - D(0)}{R}R + D(0) = \frac{1}{3}D(0) + \frac{2}{3}D(R) \tag{2.32}$$

which corresponds to the initial equation (2.21). To account for possible influences in the angular direction such as the patient table, recent reports from the American Association of Physicists in Medicine (AAPM) suggest measuring the $\text{CTDI}_{100,\text{periphery}}$–value at four peripheral positions.

The CTDI_{w}–value is also used to calculate other dose measures such as the dose length product (DLP), the effective dose and the size–specific dose estimate (SSDE). Since CTDI_{w} gives a dose estimate for only one slice, in clinical practice, a CTDI–value for volumetric acquisitions is given by

$$\text{CTDI}_{\text{vol}} = \frac{\text{CTDI}_{\text{w}}}{p} \tag{2.33}$$

where p is the pitch factor introduced in section 2.1. The CTDI–values so far estimate the dose in a central slice but do not take into account the scan length. Therefore, the so–called DLP is defined. It is given as

$$\text{DLP} = \text{CTDI}_{\text{vol}} \cdot \text{Scan length}. \tag{2.34}$$

Both, CTDI and DLP, are quantities that are displayed on every CT scanner for every given scan protocol. However, since CTDI and the derived quantity DLP are measured using a cylindrical PMMA phantom, they are not measures of patient dose but rather measures of tube output. Furthermore, CTDI and DLP tend to under– or overestimate the dose to the actual patient as function of patient constitution.

2.2.4 Effective Dose

The effective dose D_{eff} describes a stochastic health risk following an exposure to ionizing radiation to the body measured with the unit Sievert (Sv). It was introduced in ICRP 60 [80] and is defined as

$$D_{\text{eff}} = w_{\text{T}} \cdot H_{\text{T}} \tag{2.35}$$

wherein w_{T} represents a tissue weighting factor and H_{T} the organ dose. The organ dose or the equivalent dose for a specified tissue is defined as

$$H_{\text{T}} = \sum_{\text{R}} w_{\text{R}} \cdot D_{\text{T,R}} \tag{2.36}$$

wherein T represents the tissue of interest, $D_{\text{T,R}}$ is the absorbed dose in the tissue and w_{R} is a radiation weighting factor. This factor depends on the type of radiation and in some cases on its energy. It is based on the relative biological effectiveness (RBE) which compares different types of radiation in terms of their biological effect at the same absorbed energy. In the case of computed tomography, photons are the only type of radiation administered to the patient, hence, w_{R} is equal to 1. The tissue weighting factors w_{T} refer to the risk of each organ to develop cancer due to an exposure of radiation. The ICRP publishes updates every 10 to 20 years. There have been many

Table 2.2: Tissue weighting factors recommended by the ICRP published in 1977, 1991, and 2007 [80]–[82]. Entries without values indicate that no weighting factor is provided in the respective edition of the report.

Tissue / Organ	ICRP (1977)	ICRP (1991)	ICRP (2007)
Bladder		0.05	0.04
Bone surface	0.03	0.01	0.01
Brain			0.01
Breast	0.15	0.05	0.12
Colon		0.12	0.12
Esophagus		0.05	0.04
Gonads	0.25	0.20	0.08
Liver		0.05	0.04
Lung	0.12	0.12	0.12
Red bone marrow	0.12	0.12	0.12
Remainder	0.30	0.05	0.12
Salivary glands			0.01
Skin		0.01	0.01
Stomach		0.12	0.12
Thyroid	0.03	0.05	0.04
Total	1.00	1.00	1.00

changes to the factors over time, and new organs have been added. Updated values for the tissue weighting factors were published in 1977, in 1990, and in 2007, respectively [80]–[82]. Table 2.2 summarizes these values.

There are also conversion factors k which convert from DLP to an estimate of the effective dose given the examined body region and the patient age, according to

$$D_{\text{eff}} = k \cdot \text{DLP}. \tag{2.37}$$

These factors are intended to allow for a rapid estimation of the effective dose delivered to the patient since the calculation of the actual effective dose would require an organ segmentation and computation of the dose distribution using Monte Carlo (MC) or deep learning methods. This, however, is time–consuming and usually not feasible in clinical practice. A list of k–factors is provided in table 2.3 [83]–[85].

Table 2.3: Conversion factors k given in mSv/(mGy · cm) as function of patient age. Except for the values for the adult chest, abdomen and pelvis which are related to 32 cm CTDI phantoms, all values are related to 16 cm CTDI phantoms [83]–[85].

Body region	0–year	1–year	5–year	10–year	Adult
Head	0.011	0.0067	0.0040	0.0032	0.0021
Head–Neck	0.013	0.0085	0.0057	0.0042	0.0031
Neck	0.017	0.0120	0.0110	0.0079	0.0059
Chest	0.039	0.0260	0.0180	0.0130	0.0140
Abdomen–Pelvis	0.049	0.0300	0.0200	0.0150	0.0150
Chest–Abdomen–Pelvis	0.044	0.0280	0.0140	0.0140	0.0150

2.2.5 Size–Specific Dose Estimate

A modern approach to obtain a patient–specific dose estimate is the SSDE which takes into account the diameter of the patient in addition to the radiation output of the x–ray tube [86]. The patient is assumed to have an elliptical shape and can therefore be described by two different radii $r_{\text{LAT}} = \frac{\text{LAT}}{2}$ and $r_{\text{AP}} = \frac{\text{AP}}{2}$ in lateral (LAT) and in a.p. direction, respectively. The area of the ellipse is given by $\text{Area} = \pi r_{\text{LAT}} r_{\text{AP}}$. At a given z–position, the effective diameter is thus defined as

$$\text{effective diameter} = 2\sqrt{\frac{\text{Area}}{\pi}} = \sqrt{\text{AP} \times \text{LAT}}. \tag{2.38}$$

However, considering only geometrical lengths is not entirely accurate since radiation dose absorption depends on tissue composition. For example, an abdomen and a thorax could have very similar diameters and areas, but because the lungs are not very dense, they would significantly differ in terms of absorption and therefore result in a different

absorbed dose. To overcome this drawback, AAPM report No. 220 [87] introduced another measure — the water–equivalent diameter. First, the water–equivalent area can be calculated. This is the diameter that a water phantom with the same attenuation properties as the patient would have. The corresponding formula is

$$A_{\mathrm{w}} = \sum \left(\frac{\mu(x,y)}{\mu_{\mathrm{water}}} \right)^{\alpha} \cdot A_{\mathrm{pixel}}. \tag{2.39}$$

Here, A_{pixel} is the area of a single pixel in the CT image. The parameter α defines the weighting of $\mu(x,y)$ relative to water. Studies have shown that a weighting of $\alpha = 1$ is valid for CT scans. Considering eq. (2.17), this equation can be reformulated as

$$A_w = \sum \left(\frac{\mathrm{CT}(x,y)}{1000\,\mathrm{HU}} + 1 \right) \cdot A_{\mathrm{pixel}} \tag{2.40}$$

where $\mathrm{CT}(x,y)$ is the CT–value of the voxel. The water–equivalent diameter D_w can then be calculated by

$$D_w = 2\sqrt{\frac{A_w}{\pi}} = 2\sqrt{\left(\frac{1}{1000\,\mathrm{HU}} \overline{\mathrm{CT}(x,y)_{\mathrm{ROI}}} + 1 \right) \frac{A_{\mathrm{ROI}}}{\pi}}. \tag{2.41}$$

Therein, $\overline{\mathrm{CT}(x,y)_{\mathrm{ROI}}}$ is the average CT–value in the ROI. This ROI is the whole patient in the displayed CT–slice and A_{ROI} is the number of pixels in this ROI. This means, calculation of the water–equivalent diameter only requires the number of pixels and the mean CT–value from a ROI, i.e., the patient. This can be done manually at the scanner or theoretically by using automatic segmentation algorithms. To calculate D_w for axial slices using this approach, the CT scan is required. To finally obtain a SSDE–value for a patient given an effective diameter or a water–equivalent diameter, the AAPM reports provide look–up tables for conversion factors to convert from CTDI–values to absorbed dose values. In particular, these conversion factors were obtained by MC simulations of different semi–anthropomorphic phantoms with well–defined effective or water–equivalent diameters. Hence, as soon as such a quantity is known, either by manual or automatic means, the clinical practitioner can calculate an estimate to the absorbed dose by multiplying the CTDI–value displayed at the scanner with a corresponding conversion factor. However, these conversion factors are only able to provide estimates for the absorbed dose, since they do not account for the organs that are present in the FOM. Anyways, the SSDE–values provide a much better estimate to the absorbed dose compared to CTDI–values and might at least improve the perception of administered radiation dose in clinical practice.

2.3 Tube Current Modulation Techniques

2.3.1 Standard Tube Current Modulation

In a case with constant tube current, the same number of photons are emitted from each viewing angle. However, the patient's anatomy can vary significantly between lateral

and anterior–posterior projections. Figure 2.8 shows an example of a slice through the shoulders. Since many photons are absorbed in the shoulders in case of lateral views, only a few photons reach the detector. In case of the a.p. direction, the intersection lengths through the patient are much shorter and many photons will reach the detector, i.e., there is a large variation in the number of photons reaching the detector depending on the angular position of the x–ray source. The statistics of a.p. projections will be very good whereas lateral directions will show rather poor statistics. However, image noise in reconstructed images is dominated by projections with poor statistics. In the case of the shoulders, this typically results in the introduction of horizontal streak artifacts and in a very inhomogeneous noise distribution in general.

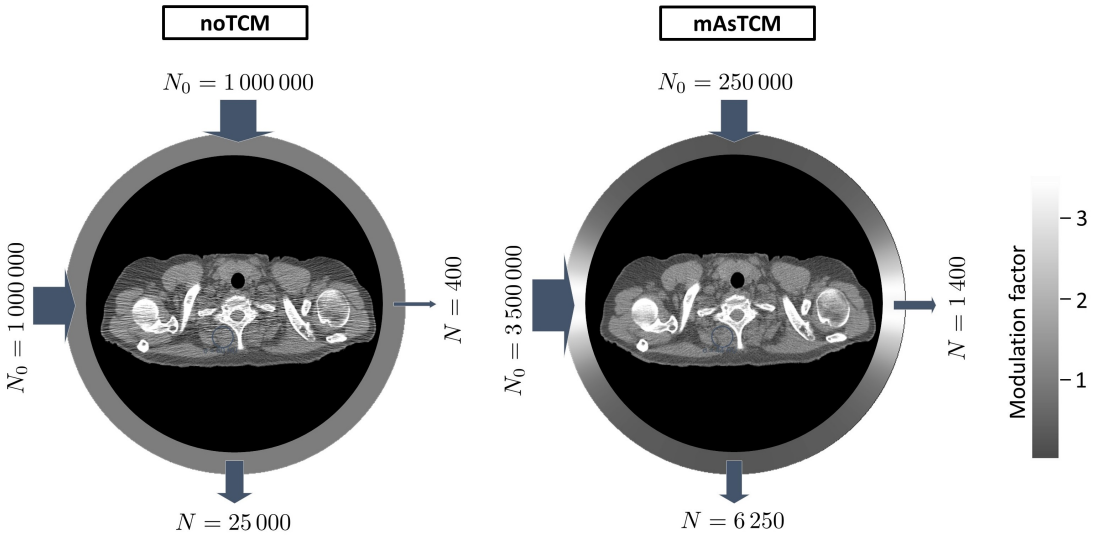

Figure 2.8: Principle of tube current modulation. On the left, a case of constant tube current is shown. Here, the same number of photons are emitted from every source position. But, due to the patient's anatomy, the number of photons reaching the detector varies strongly as function of the tube angle. This results in a high noise with severe streak artifacts. On the right, a case with TCM is shown. Projections with high attenuation receive higher tube current. Therefore, the number of photons reaching the detector is more balanced, resulting in a lower and more homogeneous noise.

By using a conventional tube current modulation technique, the current is chosen according to the statistics of the projection images. This means that views with high attenuation will be acquired using a higher tube current and views with lower attenuation will be acquired with a lower tube current. Thus, even as the total number of photons emitted, i.e., the total mAs–product, remains constant, a lower and more homogeneous noise is achieved as well as a reduction of the noise–induced streak artifacts. As a rule of thumb, the tube current should be modulated such that the same number of photons approximately pass through the center of the patient independent of the angular tube position. Such TCM techniques have been shown to reduce the total mAs–output up to

60%. Its introduction into clinical practice has therefore been of high impact and TCM methods are nowadays used in almost every clinical CT system [4].

2.3.2 Clinical Implementation of TCM Techniques

To achieve a desired image noise, the tube current $I(\alpha)$ is modulated as a function of the view angle α. In clinical practice, however, this is often combined with a modulation as function of longitudinal position z which is sometimes referred to as AEC and the tube current rather becomes $I(\alpha, z)$. The attenuation required to guide said methods can be estimated either based on a topogram or by using an online feedback loop that makes use of the previously measured 180° of data to predict the attenuation of the subsequent projections [49], [88], [89]. In particular, Toshiba uses the a.p. topogram and the lateral topogram and performs a sinusoidal modulation. The GE system also uses a single topogram and performs a sinusoidal modulation in order to perform the tube current modulation. Older systems by Philips and Siemens, on the other hand, use the information gained from the topogram as well as using the previously acquired data from 180°. A summary of available AEC and tube current modulation methods can be found in table 2.4.

Table 2.4: Automatic exposure control techniques provided by different manufacturers in clinical use.

	Toshiba	GE	Philips	Siemens
AEC+TCM Method	SUREExposure 3D standard deviation	AutomA 3D noise index	DoseRight ACS reference image	CARE Dose 4D reference mAs
Organ–specific AEC	OEM	ODM	Liver DRI	XCare
Tube voltage selection	Sure kV	kV Assistant	-	CARE kV
Cardiac CT	ECG Modulation	ECG Modulated mA	Dose Right	Adaptive ECG–Pulsing

Manufacturers offer different approaches to adjust the acquisition parameters. For example, Toshiba allows to select a preferred standard deviation in soft tissue. The tube current modulation is then chosen such that the image noise will match this predefined setting. In case of GE systems, a noise–index and a minimum and maximum mA–value are selected. Reconstruction using a standard kernel will then result in the desired image. Philips systems allow to select a baseline mAs–value and calculate the TCM curve such that the images will match a pre–defined reference image. In case of older

Siemens systems, a reference mAs–value is chosen which corresponds to a standard patient. The modulation strength can be set in five different stages from very weak to very strong.

Toshiba, GE and Siemens scanners also offer an automatic tube voltage selection which chooses the tube voltage based on the patient's size. Larger patients require higher tube voltages and hence higher photon energies to ensure that enough photons penetrate the patient and arrive at the detector to provide a sufficient image quality. Besides that, all manufacturers offer dedicated solutions for cardiac CT acquisitions [90]. However, this thesis is only concerned with the modulation of the tube current.

2.3.3 Organ–specific Tube Current Modulation

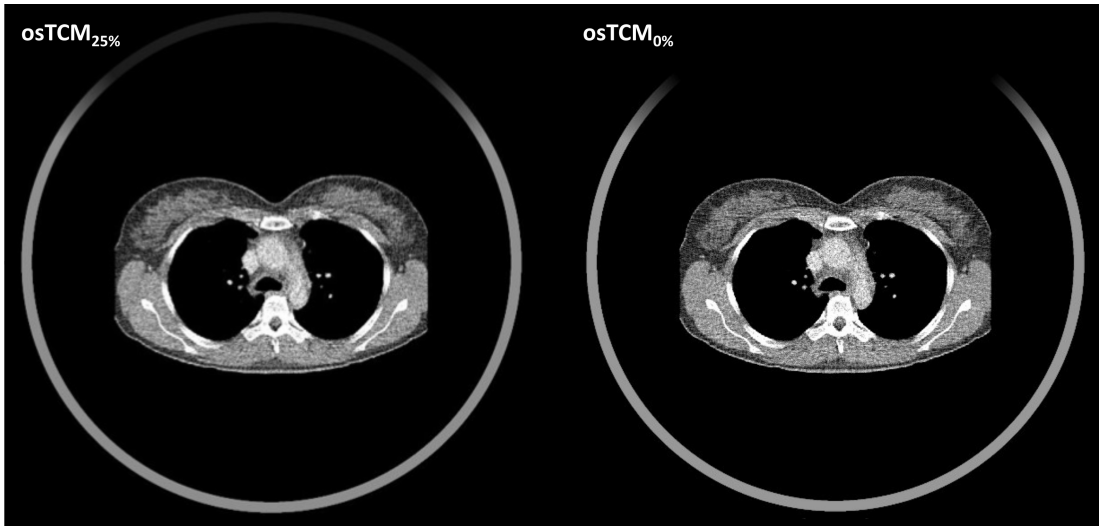

Figure 2.9: Principle of an organ–specific TCM. The tube current is decreased for pre–defined angles anterior of the patient to reduce dose to organs such as the breasts or eye lenses. The tube current is often set to a very low value, e.g., 25 % of a reference mAs–value (left), but it would be also possible to decrease it almost to zero (right). The circle enclosing the reconstructions indicates the tube current wherein white represents a high tube current and black represents no tube current at all.

Besides general tube current modulation techniques, osTCM techniques are widely used in clinical practice. Each major CT vendor offers such organ–specific TCM (osTCM) protocols [91]–[94]. The names of the osTCMs for the four major manufactures of clinical CT systems are listed in table 2.4. In general, all of these osTCM methods work similar. In particular, they reduce the tube current for pre–defined angular positions in front of the patient and increase the tube current for posterior views, i.e., the overall mAs–product is kept constant. However, these osTCMs are not patient–specific but follow a pre–defined modulation curve. The aim is to limit the radiation exposure to

sensitive or vulnerable organs such as the female breast or the eye lenses. An example for such a modulation curve is shown in Figure 2.9.

3 | Material and Methods

In the following, the material and methods for the riskTCM study are described. Parts of this chapter have been published in [95] and [96].

3.1 Conventional Tube Current Modulation

As mentioned in section 2.3.1, tube current modulation techniques are used in clinical routine to reduce noise–induced image artifacts and in general noise or, equivalently, the total mAs–product. In principle, tube current modulation is possible in angular (α)– and longitudinal (z)–direction. However, for this study, the focus is on the modulation in α–direction.

As a first step, it is required to estimate the expected image variance as a function of tube current I for every view angle α according to the expected attenuation. To achieve this, first the noise in the projections must be estimated. It should be noted that the projection values in CT are typically water–precorrected, i.e., the measured polychromatic attenuation is corrected to correspond to a monochromatic measurement. The water–precorrection assumes that the object is made of a single material of varying density. In patients, this material is water. This is a simplified assumption and, therefore, the presence of structures such as bones in the FOM would result in high order beam hardening artifacts since these are not corrected for in the rawdata using conventional water–precorrections. The single material assumption also means that the energy–dependent attenuation coefficient can be decomposed into a product of a spatially dependent object function $f(\boldsymbol{r})$, e.g., object density, or object attenuation value at a given energy, and into a function of energy $\psi(E)$, e.g., the energy dependence of water. That is $\mu(\boldsymbol{r}, E) = f(\boldsymbol{r})\psi(E)$. The projection value is given as line integral through the object function f along a line L by

$$p(L) = \int dL\, f(\boldsymbol{r}) \tag{3.1}$$

for the monochromatic case. The polychromatic projection value for a detected x–ray spectrum $w(E)$ normalized to unit area, is

$$q(L) = -\ln \int dE\, w(E) e^{-\int dL\, \mu(\boldsymbol{r}, E)} = -\ln \int dE\, w(E) e^{-p(L)\psi(E)}. \tag{3.2}$$

Since this is a one–to–one mapping from p to q, it will be denoted as $q = Q(p)$. It holds that

$$f(\boldsymbol{r}) \geq 0,\ w(E) \geq 0,\ \psi(E) \geq 0. \tag{3.3}$$

The inversion of the function $Q(p)$ is denoted as $p = P(q)$. The function P is the afore–mentioned water–precorrection function and is implemented in all diagnostic CT systems. It can be calculated numerically by inverting the relationship $q = Q(p)$. However, this usually requires either $w(E)$ to be known or requires special calibration techniques [97]. It is of importance to know that the measured signal before application of the water–precorrection is Poisson–distributed. This means that the variance of the signal is proportional to

$$Ie^{-q} \tag{3.4}$$

with I describing the tube current used to acquire the corresponding projection. By error propagation it is found that

$$\operatorname{Var} q \propto \frac{e^q}{I}. \tag{3.5}$$

Propagating this through the water–precorrection function results in

$$\operatorname{Var} p \propto \left(P'(q)\right)^2 \frac{e^q}{I} = \left(P'(Q(p))\right)^2 \frac{e^{Q(p)}}{I} = \frac{e(p)}{I}. \tag{3.6}$$

To simplify the following formulae, a polychromatic exponential function can be defined as

$$e(p) = \left(P'(Q(p))\right)^2 e^{Q(p)}. \tag{3.7}$$

For monochromatic radiation, the function $e(p)$ becomes an exponential function of p. Thus, $e(p)$ describes the differences in noise of a polychromatic scan compared to a monochromatic scan. In case of clinical CT, the projection data can be denoted with $p(\alpha, \beta, b)$. Herein, α is the projection angle and β is the fan angle that parameterizes the detector columns while b is the longitudinal position on the detector parameterizing the detector rows. The tube current of the x–ray tube for a given projection α will be denoted as $I(\alpha)$. Depending on the TCM algorithm, two surrogates for $p(\alpha, \beta, b)$ are required in the following:

$$p(\alpha, \beta) = \frac{1}{B} \int_{-B/2}^{+B/2} db\, p(\alpha, \beta, b), \tag{3.8}$$

is the average over all detector rows with B being the width of the detector array in the isocenter. For this study, $B = 64 \times 0.6$ mm which represents a collimation of about 40 mm. The second surrogate is the 90th percentile of $p(\alpha, \beta)$, i.e.,

$$p(\alpha) = p_{90\%}(\alpha, \beta). \tag{3.9}$$

That means that 90% of all values in $p(\alpha, \beta)$ are smaller than $p(\alpha)$ and 10% are larger.

The classical mAsTCM approaches use a single surrogate projection value, e.g., $p(\alpha)$ or similar, to apply the central ray approximation [43], [98]. I.e., the surrogate value $p(\alpha)$ is assumed to be the projection value of the central ray $\beta = 0$ and is then backprojected into the voxel at the isocenter of the scanner. For this central voxel, the variance propagation to image domain f yields

$$\operatorname{Var} f = \int d\alpha \operatorname{Var} p(\alpha) \propto \int d\alpha \, \frac{e(p(\alpha))}{I(\alpha)}. \tag{3.10}$$

Consequently, the image noise can be minimized by minimizing the cost function C according to

$$C = \int d\alpha \Big(\frac{e(p(\alpha))}{I(\alpha)} + \lambda \big(I(\alpha) - const. \big) \Big), \tag{3.11}$$

where λ is a Lagrange multiplier to constrain the tube current–time product. Alternatively, the Lagrange multiplier could be multiplied to the noise term to keep the noise constant while minimizing the tube current–time product. Both approaches would be mathematically equivalent. Minimization of the cost function yields the optimal modulation curve minimizing the image noise, i.e.,

$$I^2_{\mathrm{mAsTCM}}(\alpha) \propto e(p(\alpha)). \tag{3.12}$$

This is the basic principle of mAsTCM as described in references [43], [98] and that is used in today's CT systems in a similar way. Hence, mAsTCM only minimizes physical quantities but does not account for radiation–sensitive organs or the overall radiation–induced patient risk.

3.2 Risk–minimizing Tube Current Modulation

3.2.1 Basic Principle

The basic idea of the risk–minimizing tube current modulation (riskTCM) is to account for the radiation risk of individual organs and to adjust the tube current modulation accordingly. The riskTCM workflow is shown in figure 3.1. First, one or more topograms are acquired prior to the CT scan. This is always the case with CT systems, as it is required to derive and adapt scan parameters such as the scan range, but is also necessary for standard TCM algorithms. Based on these topograms, a CT volume has to be estimated. This study is retrospective, therefore, actual CT scans have been used. However, there are studies using deep learning approaches that show that this is possible from only a very limited number of views. Based on this approximate CT volume, with usually a very low spatial resolution, an organ segmentation of all relevant organs listed in table 2.2 is obtained. For this study, most of the organs have been manually segmented. However, there are also several deep learning approaches available in the literature to automate this task. A dose distribution given per view is also required

and would also be based on the estimated CT volume. For a possible implementation in clinical practice, a deep learning approach such as the deep dose estimation (DDE) is required for this step since the gold–standard MC methods would otherwise be too time consuming. Using the information from the organ segmentation and the dose distribution, the effective dose $D_{\text{eff}}(\alpha)$ can be calculated for each view angle. This information is then used to further calculate the riskTCM curves. All these steps will be discussed in more detail in the following sections.

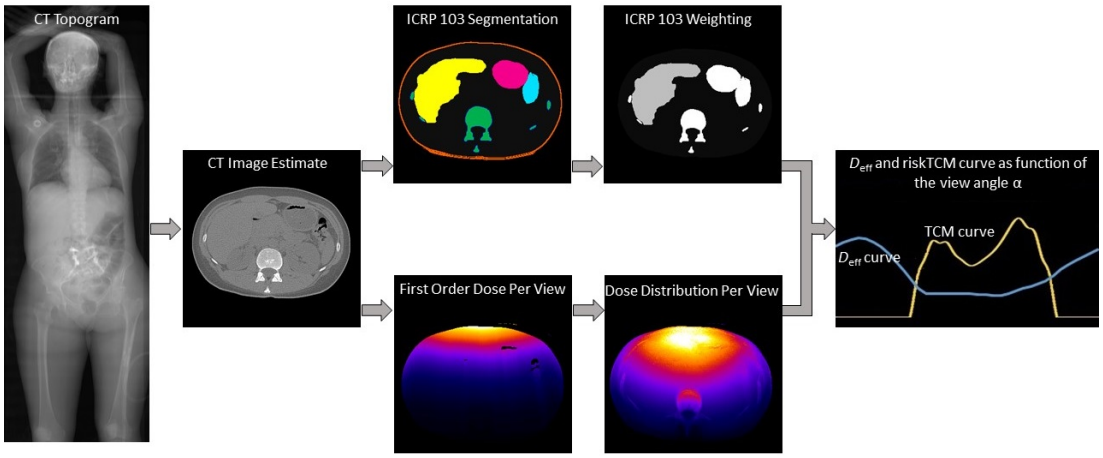

Figure 3.1: Workflow of riskTCM. The topogram(s) and other prior information are used to reconstruct a coarse CT volume approximating the patient. This coarse CT volume is used to perform a) an automatic organ segmentation and b) a view–by–view deep dose estimation. These are combined to yield the per–view effective dose $D_{\text{eff}}(\alpha)$. The per–view effective dose is then used as the risk measure for riskTCM.

3.2.2 Reconstruction from Topograms

The effective dose needs to be estimated for every view angle in order to obtain the desired riskTCM curve. Therefore, it is necessary to have some kind of CT reconstruction before the actual scan. On the basis of this, an organ segmentation and dose estimation can be performed. To be applicable in clinical practice, i.e., in a time frame of only a few minutes or even seconds, this reconstruction would have to be performed using deep learning–based methods that utilize the information from the available topogram(s) and a potential 3D camera image of the patient surface [99]. There are several studies available in the literature that illustrate that such an approach is feasible [100]–[104]. Since the focus of this study is to investigate the potential dose reduction of a risk–minimizing tube current modulation, CT reconstructions from a full CT scan are used in a retrospective manner. However, other approaches besides deep learning might be feasible, e.g., by performing an ultra–low dose CT scan and using appropriate prefilters.

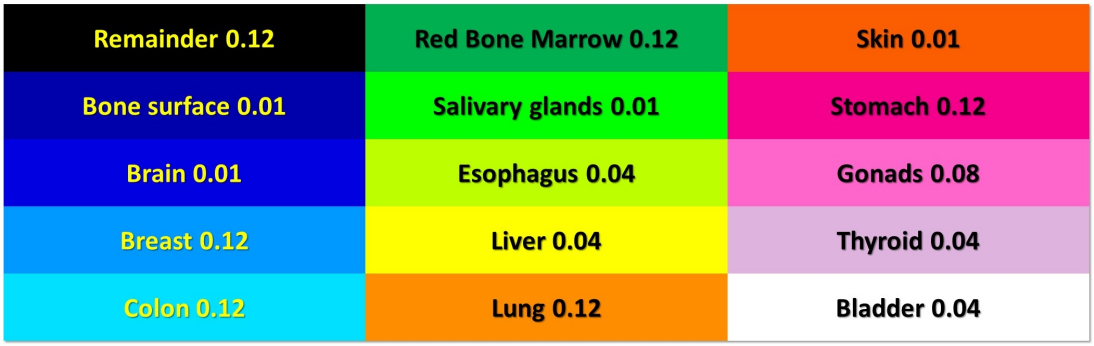

Figure 3.2: Color coding for the organ segmentations. The corresponding tissue weighting factors are also given for each organ.

3.2.3 Organ Segmentation

The estimated coarse CT volume is used to perform a segmentation of the ICRP 103 organs. As part of the overall project, segmentations have been provided by collaborators based on a previously published deep neural network [105]. Since this network cannot segment all organs required by ICRP 103 automatically, the remaining organs are segmented manually for each of the patients. These are esophagus, brain, salivary glands, gonads, colon, stomach, breast, red bone marrow, skin, and bone surface. The segmentations then allow to assign one of the ICRP 103 tissue weighting factors w_T, that are defined in reference [82] and listed in table 2.2, to each voxel followed by normalization with the total volume of the organ, resulting in a tissue weight volume $w_T(\boldsymbol{r})$ for each organ or tissue T. The color code for the organ segmentations that is used for the images shown in the results sections is displayed in figure 3.2.

3.2.4 Dose–Per–View Estimation

Once the CT volume is available, the DDE algorithm [106], [107] is used on a per–view basis to estimate the 3D dose distribution $D(\alpha, \boldsymbol{r})$ within the patient. DDE is a deep convolutional neural network that reproduces MC dose simulations based on a CT image and an analytic first–order dose estimate which are used as two–channel input to the network. In contrast to MC simulations, DDE enables a quasi–real–time dose prediction once the network is trained. The per–view effective dose is then given as

$$D_{\text{eff}}(\alpha) = \sum_T \int d^3r \, w_T(\boldsymbol{r}) D(\alpha, \boldsymbol{r}). \tag{3.13}$$

The normalization of the tissue weight volume is such that $w_T = \int d^3r \, w_T(\boldsymbol{r})$. It should be noted that all dose values used here are normalized to a unit tube current value. The final effective dose, given a tube current curve $I(\alpha)$, is then given as

$$D_{\text{eff}} = \int d\alpha \, I(\alpha) D_{\text{eff}}(\alpha). \tag{3.14}$$

3.2.5 riskTCM in Classical Reconstruction Algorithms

The riskTCM algorithm modifies the cost function (3.11) to also consider the per–view effective dose $D_{\text{eff}}(\alpha)$ that was introduced in section 2.2. Therefore, the cost function is now given by

$$C = \int d\alpha \Big(\operatorname{Var} p(\alpha) + \lambda \big(I(\alpha) D_{\text{eff}}(\alpha) \big) \Big). \tag{3.15}$$

Minimization of this cost function yields

$$I^2_{\text{riskTCM}_{\text{avg}}}(\alpha) \propto \frac{e(p(\alpha))}{D_{\text{eff}}(\alpha)}. \tag{3.16}$$

In the following, this approach will be referred to as riskTCM average ($\text{riskTCM}_{\text{avg}}$) tube current modulation in this study. The constant of proportionality in equation (3.16) is set to obtain the same image noise as a scan with mAsTCM or it is set to obtain the same effective dose as the scan with mAsTCM. This approach is referred to as $\text{riskTCM}_{\text{avg}}$ since it is possible to reconstruct data obtained with this method using classical reconstruction algorithms. In particular, these classical reconstruction algorithms such as the classical fan–beam filtered backprojection, for example, are not able to account for different noise values in projections and, thus, perform an averaging of the convolved projection values into a voxel during backprojection. The variance in such a voxel is then given as

$$V_{\text{avg}}(\boldsymbol{r}) \propto \frac{1}{4} \left(\frac{1}{I_{\text{D}}} + \frac{1}{I_{\text{C}}} \right), \tag{3.17}$$

with $\boldsymbol{r} = (x, y, z)$ being the spatial position. I_{D} describes the tube current from the direct ray while I_{C} describes the tube current from its complementary ray.

3.2.6 riskTCM in Modern Reconstruction Algorithms

The effective dose is a function of ray direction and hence is not the same for two complementary rays. I.e., the contribution of a ray to the effective dose passing from anterior to posterior is different from the complimentary ray passing from posterior to anterior. This is also a fundamental difference compared to conventional tube current modulation techniques. In the following, the cost function shall be optimized with regard to this speciality of redundant rays for patient risk–minimizing approaches. The angular tube position for a given ray can be described by either α_{D} and α_{C}, which only differ by 180°, i.e., they are complementary rays. As mentioned before, $D_{\text{eff}}(\alpha_{\text{D}}) \neq D_{\text{eff}}(\alpha_{\text{C}})$ even though $p(\alpha_{\text{D}}, +\beta) \approx p(\alpha_{\text{C}}, -\beta)$. This approximation reflects the fact that complementary rays in cone–beam CT systems are not necessarily exact but only an approximation regarding the longitudinal ray coordinates, which is also reflected during image reconstruction.

The resulting projection variances for the rays from α_{D} and α_{C} are

$$V_{\text{D}} = e\big(p(\alpha_{\text{D}}, +\beta)\big) \frac{1}{I_{\text{D}}} \qquad \text{and} \qquad V_{\text{C}} = e\big(p(\alpha_{\text{C}}, -\beta)\big) \frac{1}{I_{\text{C}}}. \tag{3.18}$$

In contrast to the classical reconstruction algorithms, where the variance is described as in equation (3.17), other, potentially more modern reconstruction algorithms, such as weighted filtered backprojection approaches [108], [109] or statistical iterative reconstruction algorithms, may implicitly or explicitly perform a voxel–specific weighting of each projection contribution to this voxel. The two contributions of the complementary rays can be statistically optimally weighted, i.e., inversely to their variance. The resulting variance becomes

$$V_{\mathrm{opt}}(\boldsymbol{r}) \propto \frac{1}{I_{\mathrm{D}} + I_{\mathrm{C}}} \quad \text{and one finds} \quad V_{\mathrm{opt}}(\boldsymbol{r}) \leq V_{\mathrm{avg}}(\boldsymbol{r}). \tag{3.19}$$

That means, for cases where $I(\alpha_{\mathrm{D}}) \neq I(\alpha_{\mathrm{C}})$, the resulting image noise is lower for reconstruction algorithms with optimal weighting.

Equation (3.11) holds true for averaging reconstruction methods in the central ray approximation. The central ray approximation, however, is no longer valid for modern reconstruction approaches since an optimal balance of direct and complementary rays needs to be determined. However, in case of the central ray, this implies to set 180° of the tube current to zero while having the other 180° non–zero. This, however, would no longer allow for image reconstruction since for fan–beam scanners, at least 180° plus fan angle of data are required. Therefore, the overall noise needs not only to be considered in the isocenter but throughout the entire FOM. For convenience, a mid–plane approximation is used and the cone–beam nature of the beam is neglected. This is a valid approximation since the cone angle in diagnostic CT is much smaller than the fan angle. The overall noise is the weighted sum over the square–root of all variances that are backprojected into the voxels:

$$N_{\mathrm{riskTCM}}(I) = \int dx\, dy\, w(\boldsymbol{r}) \sqrt{\int d\vartheta \, \frac{e\big(p(\alpha(\vartheta,\boldsymbol{r}),\beta(\vartheta,\boldsymbol{r}))\big)}{I(\alpha_{\mathrm{D}}(\vartheta,\boldsymbol{r})) + I(\alpha_{\mathrm{C}}(\vartheta,\boldsymbol{r}))}}, \tag{3.20}$$

where $w(\boldsymbol{r})$ is a weight function normalized to unit area that emphasizes voxels in the patient and dismisses those outside the patient. For this study, it is set to zero outside and to one inside the patient. However, it would also be possible to set $w(\boldsymbol{r})$ as a function of the imaging task, e.g., such that a focus is put on particular organs such as the breast. This would also include region of interest imaging tasks. Another option could be to set $w(\boldsymbol{r})$ inversely proportional to the contrast in a particular region, aiming at achieving a more balanced contrast–to–noise ratio within the patient. This would, for example, imply that more noise is accepted in regions of high contrast, e.g., close to bone or in the lungs.

Let ϑ be the angle of a ray through a voxel such that $\xi = x\cos\vartheta + y\sin\vartheta$ is the distance of the ray to the isocenter. The angle β is the angle within the fan. The angles α and β are related to ϑ and ξ via the rebinning equations $\vartheta = \alpha + \beta$ and $\xi = -R_{\mathrm{F}}\sin\beta$, with $R_{\mathrm{F}} = 595$ mm being a typical distance of the focal spot to the isocenter in clinical CT systems. The function $\alpha(\vartheta,\boldsymbol{r})$ is the angle or trajectory parameter of the source position such that a ray passing through a voxel at $\boldsymbol{r}$ under angle ϑ is being measured. It also holds that $\beta(\vartheta,\boldsymbol{r}) = \vartheta - \alpha(\vartheta,\boldsymbol{r})$. The riskTCM optimization problem can be

formulated as

$$I = \arg\min_{I} N_{\text{riskTCM}}(I) \qquad \text{with} \qquad \int d\alpha\, D_{\text{eff}}(\alpha) I(\alpha) = \text{const.} \tag{3.21}$$

The resulting tube current modulation will be called riskTCM. Equation (3.21) does not allow for an analytical minimization. Therefore, a numerical minimization using the simplex algorithm was performed [110]. To speed up the computations, a coarse voxel size of 1 cm in axial direction was used to estimate the riskTCM curve. The constant of proportionality in equation (3.21) was again set to obtain the same image noise as a scan with mAsTCM or to obtain the same effective dose as the mAsTCM scan.

Additionally, a combination of $\text{riskTCM}_{\text{avg}}$ and riskTCM shall be tested on their effective dose reduction potential. The mixed curve is determined as

$$I_{\text{riskTCM}_{\text{mix}}}(\alpha) = \frac{1}{2}\big(I_{\text{riskTCM}_{\text{avg}}}(\alpha) + I_{\text{riskTCM}}(\alpha)\big). \tag{3.22}$$

3.3 Simulation Study

3.3.1 Scanner Geometry

All simulations were based on the geometry of the SOMATOM Definition Flash CT scanner (Siemens Healthineers, Forchheim, Germany) whose collimation is 64×0.6 mm. To obtain rawdata, a 2D fan–beam forward projection for each slice of the available volumes has been performed [111]. The reason for doing a 2D fan–beam forward projection rather than a 3D cone–beam forward projection is to reduce noise contained in the original data by longitudinal averaging and will be explained in more detail below. The semi–empirical Tucker spectrum [58] with 6.0 mm Al prefiltration has been used to mimic a realistic CT x–ray spectrum. The detected spectrum was obtained by registering the emitted spectrum in an energy–integrating Gd_2O_2S (gadolinium oxysulfide, $\rho = 7.32$ g/cm^3) scintillator with a thickness of 1.4 mm. A soft thresholding of bone has been used to distinguish between water–equivalent and bone–equivalent voxels and to be able to correctly simulate the higher order beam hardening effects. The forward projected polychromatic rawdata $q(\alpha, \beta, z)$ then underwent a water–precorrection (first order beam hardening correction) to obtain the water–precorrected rawdata $p(\alpha, \beta, z)$ for further use. Note that the longitudinal detector coordinate b of the cone–beam rawdata $p(\alpha, \beta, b)$ is replaced by the slice position z in the performed simulations.

i.) Circular Scan Trajectory

To highly reduce the noise present in the forward–projected data, a running average of $p(\alpha, \beta, z)$ along the z–direction with a boxcar filter of 15 mm width has been computed. The thus obtained data $p_{15}(\alpha, \beta, z)$ are considered free of noise and were used to add noise according to the desired tube current curves $I(\alpha)$ and to reconstruct the noisy data at selected z–positions using filtered backprojection. To obtain the 90th percentile of each projection that is required for mAsTCM, for example, and to obtain the average

from equation (3.8) along the detector's longitudinal direction which is required for riskTCM, for example, $p(\alpha, \beta, z)$ has been averaged or evaluated within ±20 mm around the z–position of interest. This 40 mm range corresponds to the collimation of the simulated scanner at the isocenter.

ii.) Extension to Spiral Trajectory

CT acquisitions nowadays typically use spiral trajectories. Circular, or sequence scans, respectively, are only used in dedicated scenarios in clinical practice. Therefore, part of this study was also to obtain preliminary results with an extension of riskTCM to spiral trajectories. As a first step, the optimization is not yet performed in spiral geometry but rather the computation of the TCM curves is performed for many circular scans with a very narrow z–spacing of 2 mm. This allows for an interpolation between the circular scans according to the spiral trajectory and to obtain the resulting tube current values for specific angular and longitudinal positions $I(\alpha, z)$. The scanner parameters are again based on the SOMATOM Definition Flash CT scanner (Siemens Healthineers, Forchheim, Germany). The source to isocenter distance R_F is 595.0 mm while the source to detector distance R_{FD} is 1085.6 mm. The used collimation is 32×0.6 mm. A total of 1152 projections per revolution were considered as well as 736 detector elements in fan–direction with a fan angle of 49.6°. The pitch value has been chosen as p = 0.5 to allow for the occurrence of complementary rays. This is a rather small pitch value since the clinical range typically ranges between 0.5 to 1.4. For pitch values around 1.4, it is not guaranteed that each voxel is covered by at least 180° and image reconstruction is not possible. Since riskTCM exploits redundant rays, a pitch value of 0.6 or less has to be chosen to ensure that at least two redundant rays are always available. The rawdata are forward projected in spiral geometry. Similar to the simulations in only two dimensions, a running average in z–direction was used to obtain quasi–noise free projections. The drawback is that the longitudinal spatial resolution decreases and, in particular, structures like bones appear blurry. Again, noise is inserted according to the desired TCM curve by interpolating the tube current between the simulated circular scans for every position in the spiral trajectory. This is followed by a backprojection that accounts for complementary rays and also performs a weighting according to the noise found in the projections. Then, a back projection is performed. The weighting w of the rays is given by

$$w = I_n \cdot \exp(-p(n, m, l)) \tag{3.23}$$

Here, n describes a specific projection of the rawdata p, m a detector element in lateral direction, and l a detector element in longitudinal direction.

iii.) Organ–Specific Tube Current Modulation

As another step, riskTCM is also compared to a organ–specific TCM as illustrated in figure 3.3. For this study, a tube current modulation similar to XCare (Siemens Healthineers, Forchheim, Germany) has been implemented. This algorithm was designed

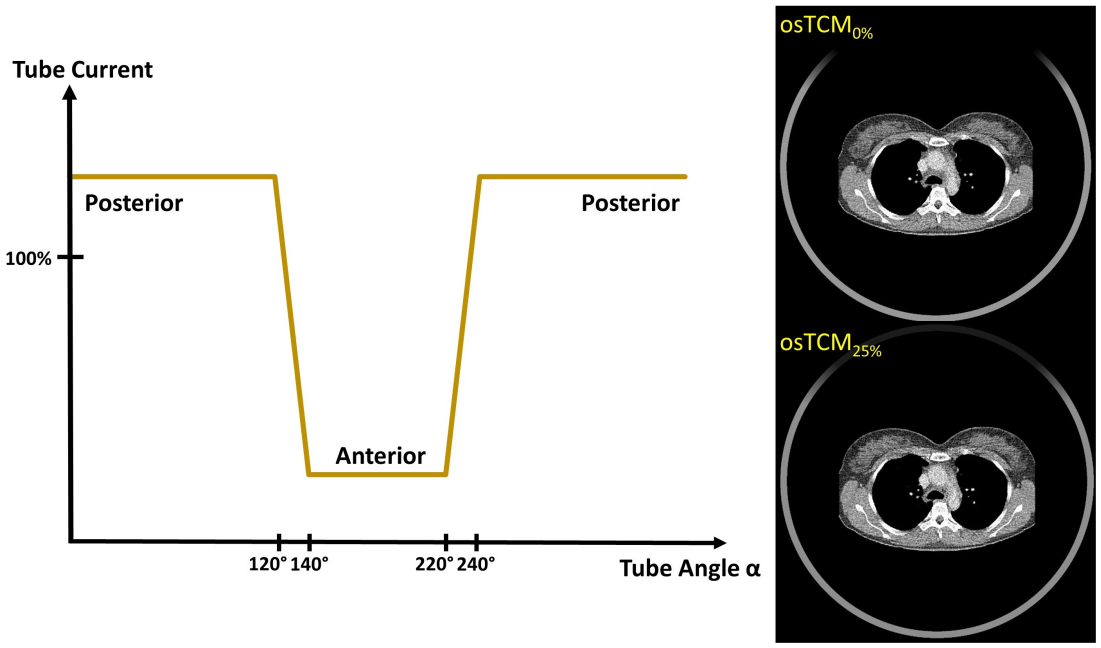

Figure 3.3: Schematic of the tube current modulation curve of the XCare algorithm (left) and examples for a tube current of 0 % of the reference current in front of the patient (right top) and of 25 % of the reference current (right bottom). The color gradient around the reconstructions indicates the tube current.

to reduce the radiation to the female breast. In particular, the tube current is decreased for an angular segment of 120° in front of the patient, e.g., to only 25 % of the overall desired current, and increased behind the patient. However, the overall tube current–time product is kept constant. For this study, two cases have been considered. First, the case that the tube current is lowered to 25 % of the reference value which will be referred to $\text{osTCM}_{25\%}$. Secondly, the tube current is turned off anterior to the patient, therefore, this case will be refereed to as $\text{osTCM}_{0\%}$. Figure 3.3 shows the working principle of the organ–specific tube current modulation.

3.3.2 Patient Population and Scan Protocols

To evaluate riskTCM and to benchmark it against mAsTCM and other TCM methods, 20 whole–body volumetric patient scans from the Visceral dataset [112] acquired and reconstructed with a clinical CT scanner were used. For the evaluation concerning osTCM, 7 data sets provided by the Klinikum Nürnberg have been used which contain only female patients. The study was approved by the Institutional Review Board. Written informed consent was waived due to the respective nature of the study. Investigation was conducted according to the principles of the Helsinki declaration and good clinical practice. The patients ages range from 32 to 66 years with an median of 42 years.

In total, seven different tube current curves have been evaluated. First, a study was

performed using a circular trajectory. Therefore, riskTCM, riskTCM$_{\text{avg}}$, riskTCM$_{\text{mix}}$ and the case of no tube current modulation, i.e., noTCM, have been evaluated and compared with mAsTCM since this is the clinical gold standard. Different slices have been selected, each corresponding to a different body region. In particular, the head, neck, thorax, abdomen and pelvis have all been investigated. For the head, two cases have been considered: the head with arms placed next to it, as it is in the original data set, and the case without arms next to the head, since both cases might be found in clinical practice. For the images without arms next to the head, the arms have been manually removed from the CT images and corresponding segmentations. Four different tube voltages have been investigated to evaluate a possible dependence of the effective dose reduction on the tube voltage. Namely, 70 kV, 100 kV, 120 kV, and 150 kV, respectively, have been used since they cover the relevant range of tube voltages used in clinical CT.

Furthermore, two different cases of organ–specific tube current modulations have been investigated. The case without tube current anterior to the patient, namely osTCM$_{0\,\%}$, and the case with low tube current in front of the patient, i.e., osTCM$_{25\,\%}$ are considered in the following. For this evaluation, the osTCM algorithms have been compared to noTCM, mAsTCM and riskTCM. Here, only the region of the chest is of interest since the reduction of the dose administered to the female breast is one of the main goals when using osTCM methods such as XCare. This study was only conducted for a tube voltage of 70 kV.

Further comparisons were performed for cases using a spiral trajectory. Here, the cases of riskTCM, noTCM, mAsTCM, riskTCM$_{\text{avg}}$ and riskTCM$_{\text{mix}}$ are investigated. In case of these methods, a pitch value of 0.5 was chosen to ensure the availability of complimentary rays. This study was also only conducted for a tube voltage of 70 kV.

For all cases, the tube current curves $I(\alpha)$ were scaled such that either the resulting image noise or the effective dose D_{eff} is the same for all cases.

The whole–body scans only cover the patient up from the knees. Therefore, the organ doses of organs such as the skin, bone surface, red bone marrow or the remainder may be overestimated. This results in an overestimation of the effective dose. Under the assumption that the difference between the evaluated TCM methods is rather small outside of the scan area, it would follow that the overestimation of the dose is like an offset to all effective dose values of all methods. Thus, the potential effective dose reduction of riskTCM compared to the other methods could be slightly underestimated. However, in the following evaluation, this will be neglected for.

3.4 Phantom Measurements

To perform real measurements with riskTCM is difficult since it would require to manually control the tube current curve in a clinical CT system. I.e., a system would be required that allows access to the tube current modulation functionality. However, changing these parameters in a system used for routine clinical examinations would mean to alter an approved medical device and actual patient scans would be challenging from a organizational and legal perspective. Therefore, another – simpler – approach

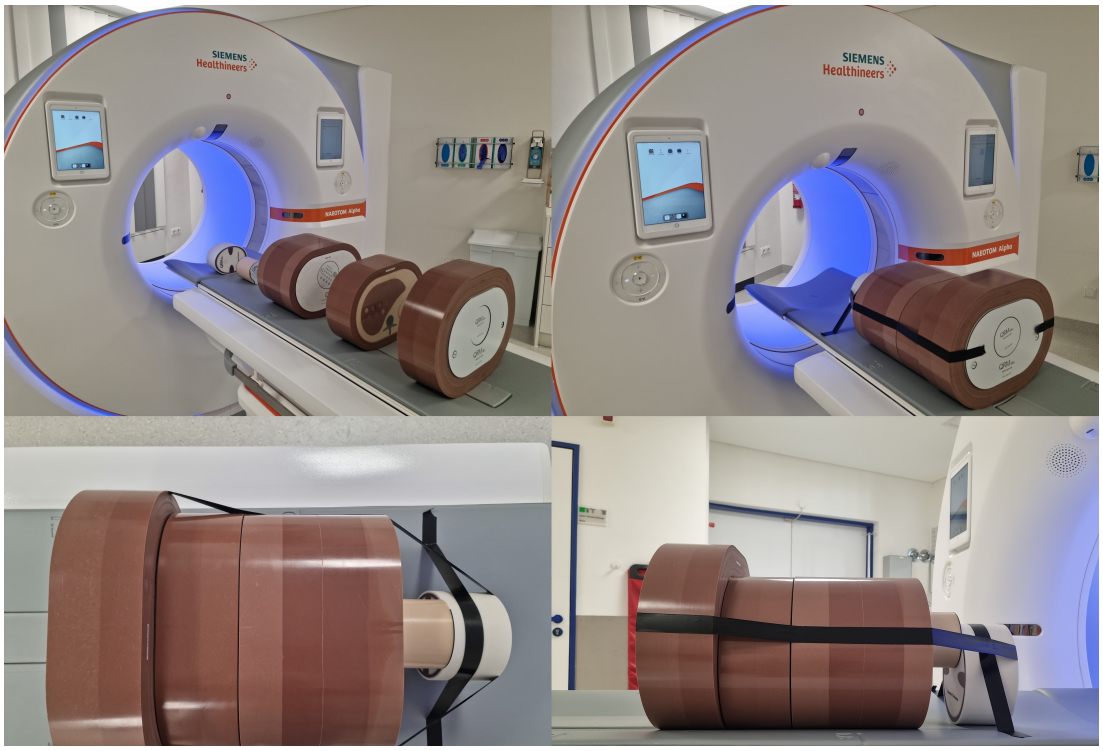

Figure 3.4: Assembling of the semi–anthropomorphic phantoms. The pelvis phantom with a large fat ring, the abdomen phantom with a medium fat ring, the thorax phantom with a medium fat ring, a low contrast phantom as neck replacement, and the head phantom have been put together to mimic a patient. The phantoms were scanned with the Naeotom Alpha scanner (Siemens Healthineers, Erlangen, Germany).

has been pursued herein. Measurements with different dose levels have been acquired of all available semi–anthropomorphic phantoms (QRM – A PTW Company, Möhrendorf, Germany) to generate data that can be combined to mimic different TCM scenarios. A total of six phantoms have been used to assemble a semi–anthropomorphic patient. A head phantom, a low contrast phantom that is supposed to mimic the neck, a thorax and an abdomen phantom with medium fat rings as well as a pelvis phantom with a large fat ring. The phantoms have been placed one after the other in a NAEOTOM Alpha scanner (Siemens Healthineers, Forchheim, Germany) located at the University Hospital of Mannheim. Pictures are shown in figure 3.4. Not all organs of interest are available using these semi–anthropomorphic phantoms. However, brain, bone surface, liver, lungs, red bone marrow, skin, the urinary bladder and the remainder can be segmented. A high dose measurement has been performed using an effective tube current–time product of 155 mAs and a tube voltage of 120 kV. The $\mathrm{CTDI}_{32\,\mathrm{cm}}$–value for this measurement was 12.2 mGy to establish a noise–free ground truth. Similar to previous sections, the dose distribution was calculated for circular scans at various z–positions and 36 angles per

circular scan. The available organs have been segmented manually. By combining both information, the organ doses as function of z– and α–position have been obtained. Based on this, the riskTCM curve as well as noTCM, mAsTCM, riskTCM$_{\text{avg}}$ and riskTCM$_{\text{mix}}$ have been computed. Additional measurements have been performed between 5 mAs (CTDI$_{32\,\text{cm}}$–value of 0.39 mGy) and 110 mAs (CTDI$_{32\,\text{cm}}$–value of 8.69 mGy) in steps of 15 mAs. The eight reconstructions obtained using these data have been forward projected. Unlike in simulations, noise is not added to quasi–noise free projections in this case but actual acquired projections are used for image reconstruction. In particular, a new set of rawdata is computed for each TCM approach as follows. For every given tube current value at every given tube position, two of the afore–mentioned datasets are found that closely match the desired tube current. A linear interpolation is used between projections obtained using these two different tube currents to obtain a projection with the tube current given by the TCM curve. This is done for all required projections and the resulting data are reconstructed to yield an image that was acquired with a desired TCM approach. Since the tube current has to be greater than zero, the minimum for the tube current values has been chosen to be the ultra–low dose measurement acquired with a CTDI$_{32\,\text{cm}}$–value of 0.39 mGy.

4 Results

Some parts of the results regarding the evaluation of riskTCM as a function of body region and tube voltage are published in [95]. Parts of the results concerning the evaluation of riskTCM versus osTCM are published in [96]. Exemplary patient images have a similar layout as in the mentioned publications. However, different example patients are shown in the following sections.

4.1 riskTCM as a Function of the Body Region

First, the potential dose reduction of riskTCM is evaluated as a function of body region. Therefore, the tube voltage is fixed at 70 kV for the results and images presented in this section. Table 4.1 illustrates the potential effective dose reduction for the six different body regions that were investigated for the five TCM algorithms, namely, noTCM, mAsTCM, $\text{riskTCM}_{\text{avg}}$, $\text{riskTCM}_{\text{mix}}$, and riskTCM. All values are given relative to mAsTCM since this is the clinical standard. Furthermore, all tube current modulation approaches were chosen to result in the same spatial resolution and image noise, i.e., the same image quality.

Table 4.1: Relative effective dose values for all TCM approaches. The values are normalized to mAsTCM. Image noise and spatial resolution and thus image quality is kept constant. The results are averaged over all patients and given for 70 kV. The error is given as the standard deviation over the patients.

Body region	noTCM	mAsTCM	$\text{riskTCM}_{\text{avg}}$	$\text{riskTCM}_{\text{mix}}$	riskTCM
Head+Arms	**170 %** ± 13 %	**100 %**	**95 %** ± 2 %	**90 %** ± 2 %	**88 %** ± 5 %
Head	**111 %** ± 10 %	**100 %**	**97 %** ± 2 %	**91 %** ± 4 %	**87 %** ± 6 %
Neck	**242 %** ± 40 %	**100 %**	**89 %** ± 6 %	**78 %** ± 8 %	**73 %** ± 9 %
Thorax	**118 %** ± 8 %	**100 %**	**94 %** ± 2 %	**84 %** ± 5 %	**77 %** ± 6 %
Abdomen	**115 %** ± 14 %	**100 %**	**92 %** ± 3 %	**77 %** ± 7 %	**68 %** ± 7 %
Pelvis	**155 %** ± 20 %	**100 %**	**93 %** ± 2 %	**80 %** ± 7 %	**73 %** ± 9 %

In case of head examinations with arms raised next to the head, noTCM requires a significantly higher radiation dose compared to mAsTCM to achieve the same spatial

resolution and image quality, i.e., image noise. That means that in this case even the standard mAsTCM guarantees a reduction of patient risk over noTCM. The riskTCM$_{\text{avg}}$ algorithm only results in a small reduction of D_{eff} of about 5 %. With riskTCM$_{\text{mix}}$, however, about 10 % of the effective dose can be saved. Using riskTCM, the effective dose can be reduced by about 12 % compared to mAsTCM. Figure 4.1 shows an exemplary patient. This figure shows a total of six images, five of which are reconstructions obtained using noTCM, mAsTCM, riskTCM$_{\text{avg}}$, riskTCM$_{\text{mix}}$ and riskTCM. The lower right image shows the organ segmentations according to ICRP 103. The corresponding color coding can be found in section 3.2.3. The circular curve around the organ segmentation shows the effective dose for a constant tube current and shall serve as a reference.

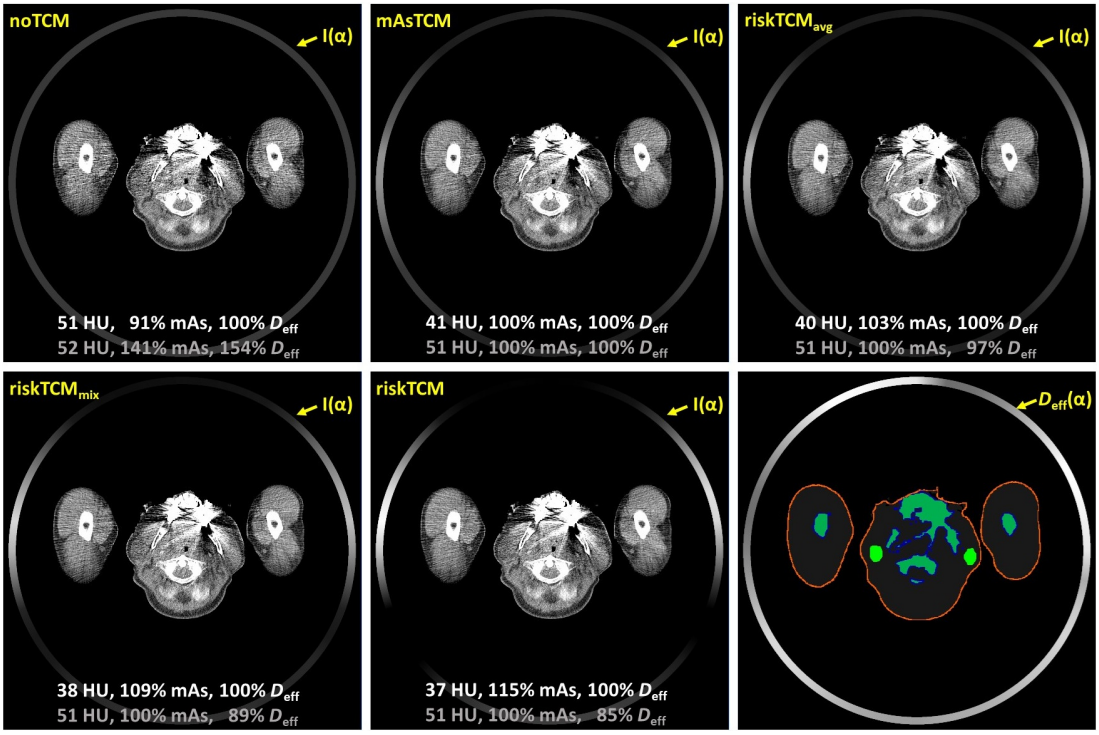

Figure 4.1: noTCM, mAsTCM, riskTCM$_{\text{avg}}$, riskTCM$_{\text{mix}}$ and riskTCM images (C = 25 HU, W = 400 HU) as well as the segmented organs for an exemplary head examination with arms placed next to the head. In section 3.2.3 it is explained which colors are assigned to which organs. The circular density plots circumscribing the 50 cm FOM indicate the tube current curves $I(\alpha)$ for the CT images and the effective dose curve at constant tube current $D_{\text{eff}}(\alpha)$ for the segmented organ image. The images are shown at constant effective dose (100 % D_{eff}). Image noise values as well as mAs integrals are given in the upper of the two rows in white. In addition, the numerical evaluation is given for the case of constant image noise in the lower rows in gray.

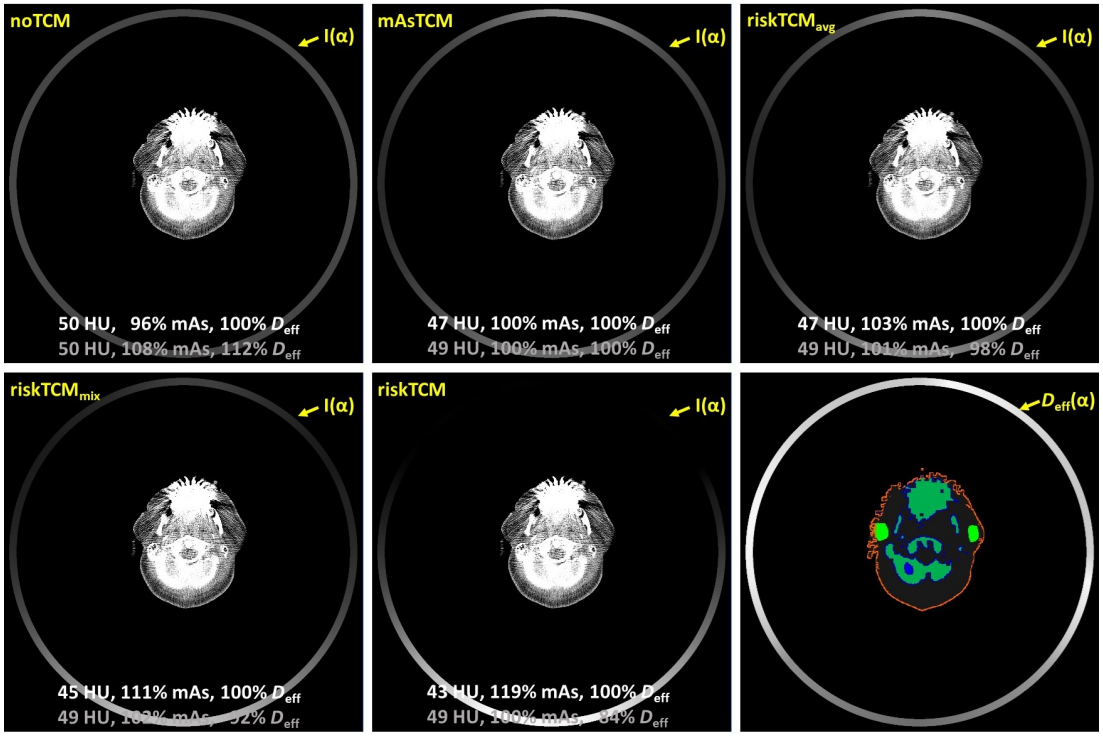

Figure 4.2: noTCM, mAsTCM, riskTCM$_{\text{avg}}$, riskTCM$_{\text{mix}}$ and riskTCM images (C = 25 HU, W = 400 HU) as well as the segmented organs for an exemplary head examination without arms placed next to it. The layout is the same as in figure 4.1.

I.e., a white color indicates projections that contribute much to effective dose and allows for an interpretation of dose contributions due to the location of radiation–sensitive organs. The images are all reconstructed at the same effective dose and hence show different noise levels. Image noise, mAs– and the effective dose values are provided below the respective reconstructions for the two following cases: values in white directly refer to the afore–mentioned reconstructions, i.e., the effective dose is the same in each case. The values in light gray show results for a case of constant noise, and thus, the effective dose values vary. The circular gray color gradients around the reconstructions indicate the tube current as a function of angular tube position. For this example of a head scan with arms next to it, the noise is the highest for the noTCM image with 51 HU. With mAsTCM, the noise can be reduced to 41 HU. With riskTCM$_{\text{avg}}$, the noise is slightly lower at about 40 HU. The mixed case riskTCM$_{\text{mix}}$ shows a further reduction of image noise to 38 HU, while the riskTCM reconstruction shows the lowest image noise of 37 HU. As stated before, values shown in gray illustrate cases with same noise levels and effective dose is given relative to mAsTCM. E.g., noTCM achieves the same noise as mAsTCM of 52 HU but requires 154 % of the effective dose to achieve this. riskTCM$_{\text{avg}}$ shows only a very low effective dose reduction of 3 % compared to

mAsTCM. riskTCM$_{\text{mix}}$ is able to reduce the effective dose by about 11 % compared to mAsTCM for this specific case. Similarly, riskTCM (bottom mid) requires only 85 % of the effective dose of the mAsTCM acquisition to achieve the same image quality, i.e., the effective dose can be reduced by about 15 % compared to mAsTCM in this case. In the following, riskTCM$_{\text{avg}}$ and riskTCM$_{\text{mix}}$ will not be addressed for in the text but can be found in the tables and figures. However, it shall be noted that the effective dose at same image quality is always the lowest for riskTCM, the second lowest for riskTCM$_{\text{mix}}$, followed by riskTCM$_{\text{avg}}$, mAsTCM and is the highest for noTCM.

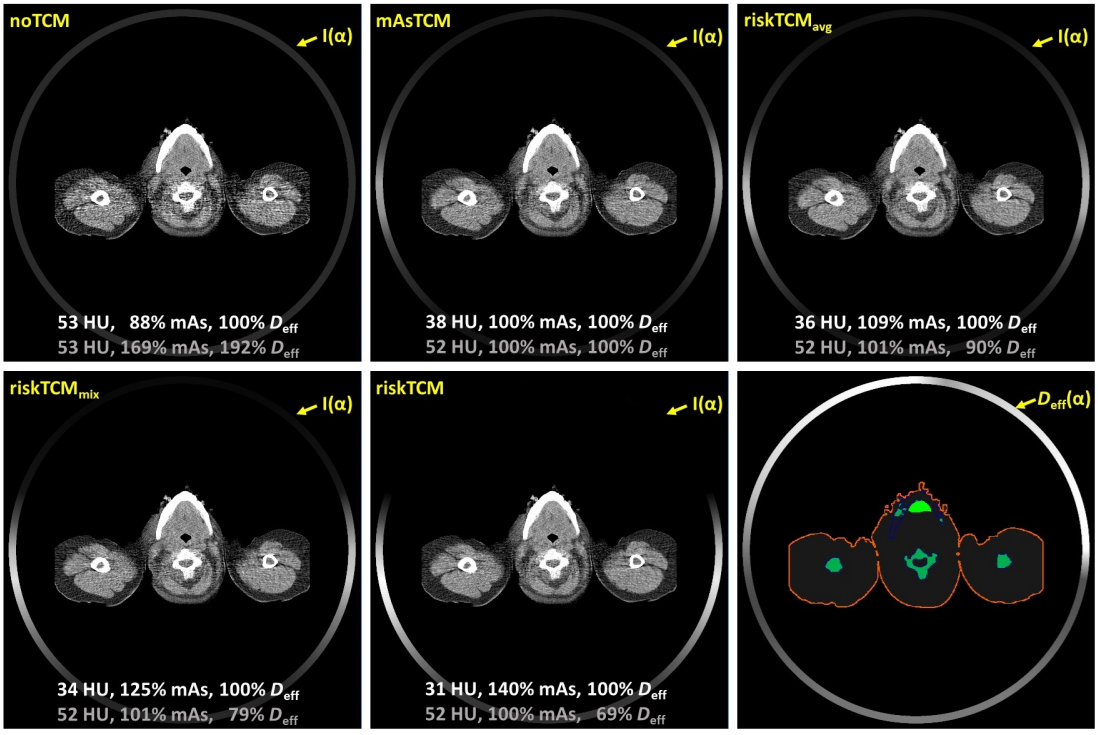

Figure 4.3: noTCM, mAsTCM, riskTCM$_{\text{avg}}$, riskTCM$_{\text{mix}}$ and riskTCM images (C = 25 HU, W = 400 HU) as well as the segmented organs for an exemplary neck examination. The layout is the same as in figure 4.1.

Considering examinations of the head without arms next to it, the difference between noTCM and mAsTCM is not as pronounced as before since now the patient shape is more circular. Using noTCM requires around 11 % more effective dose to obtain the same image noise compared to mAsTCM. These results are also summarized in table 4.1. With riskTCM, about 13 % of effective dose can be reduced compared to the clinical gold standard. This is very similar to the case of arms placed next to the head. Figure 4.2 shows exemplary images for the five different TCM methods for one patient. For the case of constant effective dose, i.e., the values given in white color, noTCM shows an image noise of 50 HU while mAsTCM can reduce it to about 47 HU. With riskTCM, the image noise is the lowest with 43 HU. Considering the case of constant

image noise, noTCM requires around 12 % more effective dose compared to mAsTCM in order to maintain the desired image quality. About 16 % of effective dose can be reduced by using riskTCM.

For the case of neck and shoulder examinations, the difference between noTCM and mAsTCM is even more pronounced because the shoulders are highly inhomogeneous in lateral direction compared to projections acquired in a.p. directions. Table 4.1 illustrates that in this case more than twice the effective dose is required for noTCM to achieve the same image quality as with mAsTCM. The highest dose reduction can be achieved with riskTCM with an average of 27 % over all patients. Figure 4.3 shows an exemplary slice for the neck region. Here, mAsTCM can significantly reduce image noise and noise–induced streak artifacts. The noise is reduced from 53 HU to 38 HU at the same effective dose. riskTCM can lower the noise even further to about 31 HU. For the case of constant noise, noTCM requires almost twice as much effective dose as mAsTCM to achieve the same noise value. With riskTCM the highest effective dose reduction can be achieved with 31 % compared to mAsTCM.

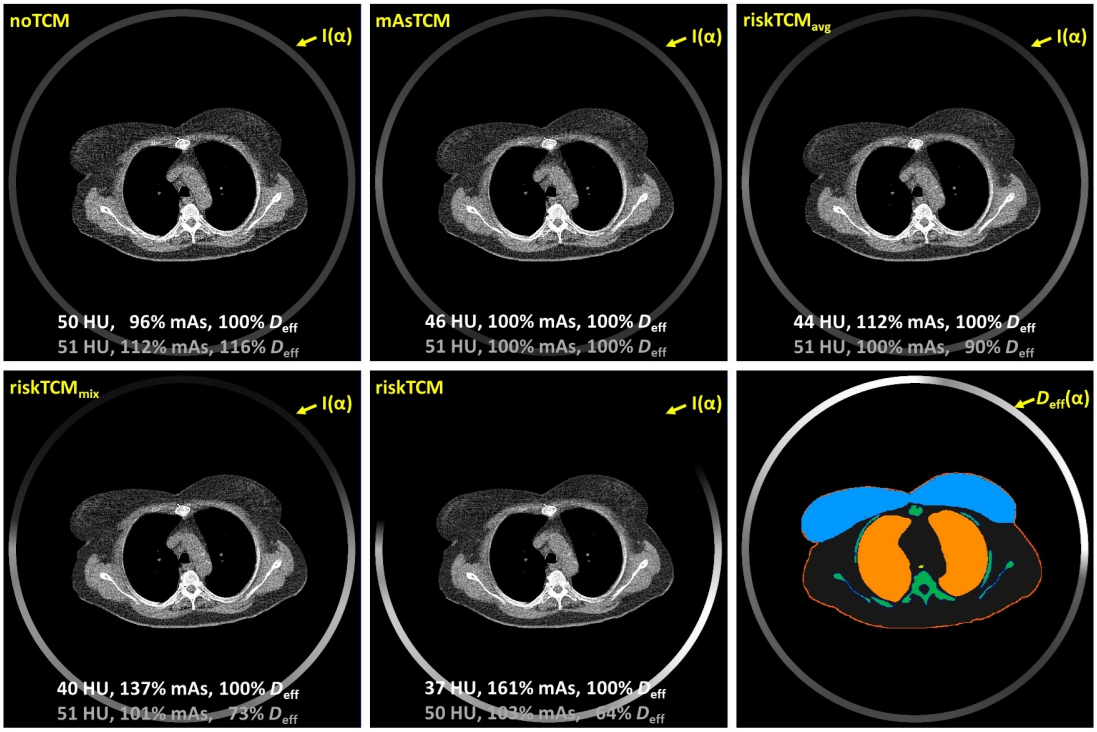

Figure 4.4: The reconstructions for noTCM, mAsTCM, riskTCM$_{avg}$, riskTCM$_{mix}$ and riskTCM (C = 25 HU, W = 400 HU) as well as the segmented organs for an exemplary thorax examination. The layout is the same as in figure 4.1.

For thorax acquisitions, table 4.1 shows that on average the difference between a constant tube current and mAsTCM is rather small. This is due to the fact that patients tend to be rather circular shaped and have a homogeneous tissue composition

across all projection angles in this region. Again, riskTCM has the highest potential effective dose reduction of about 23 % compared to mAsTCM. An example patient for the thorax patient is shown in figure 4.4. This figure shows a female patient and therefore the female breast, as a radiation sensitive organ, results in a high effective dose at constant tube current anterior of the patient and hence the potential effective dose reduction in this anatomical case is very high. About 36 % of effective dose can be reduced by riskTCM compared to mAsTCM at the same noise level. As can be seen from table 4.1, the difference between mAsTCM and noTCM is not as large for thorax scans. In particular, noTCM requires about 16 % more effective dose to achieve the same image noise. Considering the noise reduction potential at same effective dose, it can be seen that while noTCM provides an image noise about 50 HU, mAsTCM can reduce the image noise to 46 HU. The riskTCM acquisition has the lowest noise with 37 HU.

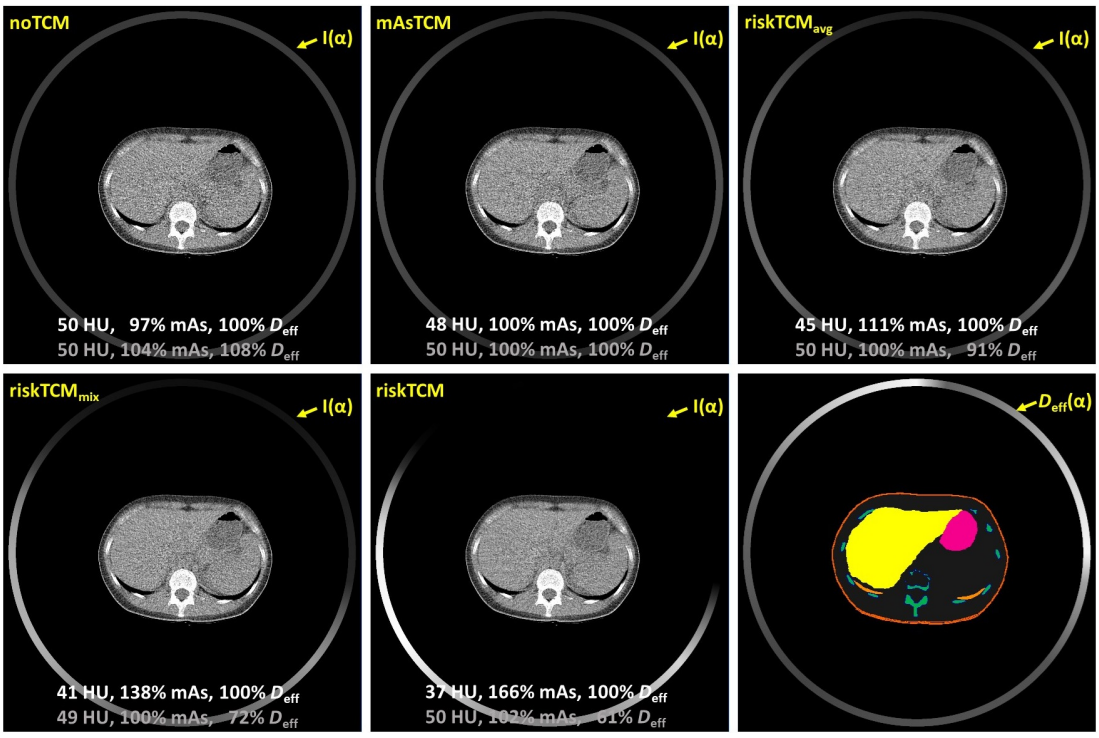

Figure 4.5: The reconstructions for noTCM, mAsTCM, riskTCM$_{avg}$, riskTCM$_{mix}$ and riskTCM (C = 25 HU, W = 400 HU) as well as the segmented organs for an exemplary abdomen examination. The layout is the same as in figure 4.1.

Another clinically relevant body region of interest is the abdomen. Table 4.1 shows that similar to the thorax, mAsTCM and noTCM are very similar. The case of constant tube current requires, on average, about 15 % more effective dose to achieve the same image quality as mAsTCM. On the other hand, riskTCM achieves a potential effective dose reduction of 32 % which is the highest across the body regions studied. Examples

for abdominal acquisitions are shown in figure 4.5. Compared to the noTCM acquisition which has a noise value of 50 HU, mAsTCM shows only a slight improvement of noise with a level of 48 HU. The highest noise reduction is seen for riskTCM with an image noise of only 37 HU. Considering the case of constant noise, the effective dose reductions reflect the noise values seen for the five different cases. noTCM requires a slightly higher effective dose of 8 % compared to mAsTCM in order to achieve the same image quality. riskTCM achieves the greatest effective dose reduction of 39 % compared to mAsTCM in this case.

The last body region of interest considered herein is the pelvis. Table 4.1 illustrates that, on average, the case of constant tube current requires an increase of 55 % compared to mAsTCM to achieve the same image noise. An effective dose reduction of about 27 % can be expected from riskTCM compared to the clinical standard mAsTCM. An example patient is shown in figure 4.6. Considering the images, it can be seen that the riskTCM reconstruction with an image noise of 42 HU provides a good noise reduction compared to noTCM with an image noise of 54 HU and mAsTCM with 50 HU. Considering the values in gray which provide the effective dose values relative to mAsTCM at constant noise in this example, it can be seen that noTCM requires about 15 % more effective dose than mAsTCM, in this case. Again, riskTCM shows the highest potential dose reduction, about 28 % compared to mAsTCM.

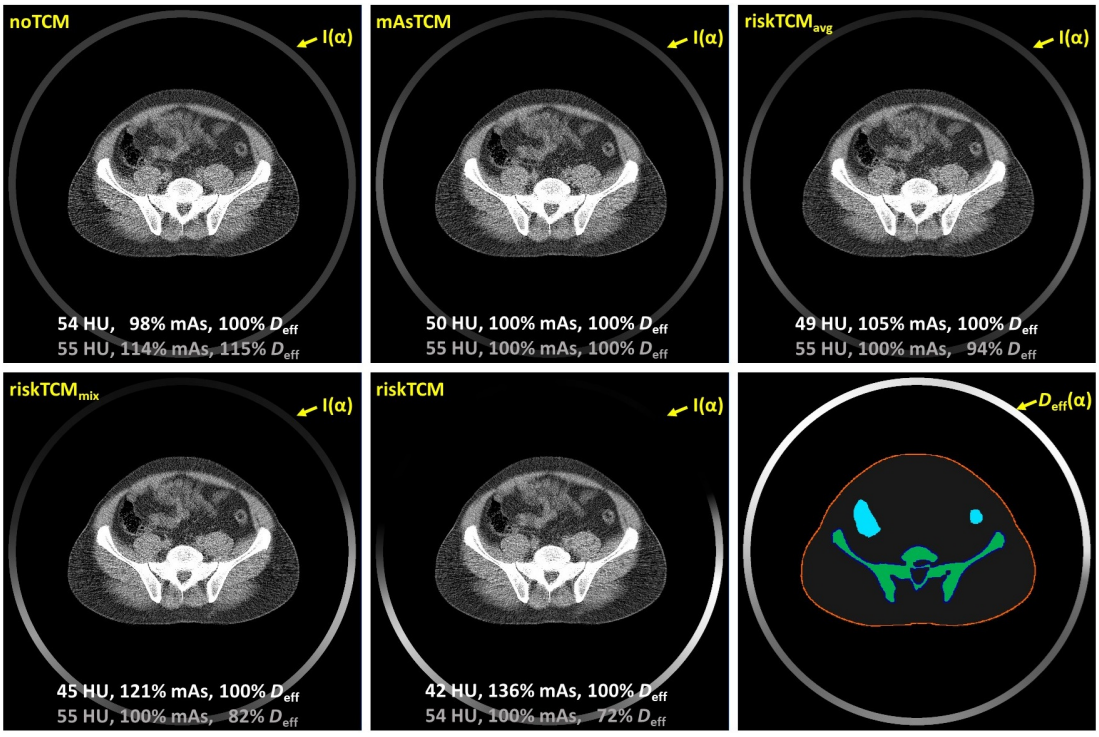

Figure 4.6: The reconstructions for noTCM, mAsTCM, riskTCM$_{avg}$, riskTCM$_{mix}$ and riskTCM (C = 25 HU, W = 400 HU) as well as the segmented organs for an exemplary pelvis examination. The layout is the same as in figure 4.1.

4.2 riskTCM as a Function of the Tube Voltage

Next, a possible influence of the tube voltage on the potential dose reduction shall be evaluated. To do so, for every body region, the effective dose at the same image noise for four different tube voltages, in particular, 70 kV, 100 kV, 120 kV, and 150 kV has been evaluated. This covers the tube voltage range of typical clinical CT systems. In particular, the body regions head with and without arms placed next to it, the neck, thorax, abdomen, and pelvis have been evaluated. The results for the different TCM methods for all body regions and tube voltages are shown in table 4.2.

First, the head with arms placed next to it has been investigated. It can be seen that for most TCM methods, only small differences are seen throughout the tube voltages. For noTCM, an increase in effective dose of about 65 % to 70 % compared to mAsTCM is required to maintain image quality across the tube voltages. For riskTCM$_{\text{avg}}$, the effective dose reduction compared to mAsTCM is about 4 % to 5 % for all tube voltages. For riskTCM$_{\text{mix}}$, the effective dose reduction is about 9 % to 11 % across the tube voltages. For riskTCM, the effective dose reduction potential compared to mAsTCM is about 12 % for 70 kV, 13 % for 100 kV, and 11 % for 120 kV and 150 kV. In the following, the description of the results is focused on the cases of noTCM, mAsTCM and the novel riskTCM. However, the results for riskTCM$_{\text{avg}}$ and riskTCM$_{\text{mix}}$ can still be found in table 4.2. Note that, generally, the results for riskTCM$_{\text{avg}}$ do not change much across all tube voltages, while the riskTCM$_{\text{mix}}$ results vary across the tube voltages since its tube current values are of equal parts of riskTCM$_{\text{avg}}$ and riskTCM. For the case of the head without arms placed next to it, the differences are small throughout the various tube voltages. With noTCM, around 10 % to 11 % more of effective dose are required compared to mAsTCM to obtain the same image noise. With riskTCM, about 13 % of effective dose can be spared compared to mAsTCM for 70 kV. For 120 kV, the dose saving is about 12 % while it is about 11 % for 120 kV and 150 kV.

Next, the results for the neck region are of interest. Using noTCM results in an high increase of effective dose compared to mAsTCM in the neck and shoulder region. An increase of about 122 % to 163 % is necessary to maintain image noise dependent on the tube voltage. The results indicate a small decrease of potential dose reduction with increasing tube voltage for riskTCM. While riskTCM potentially decreases the effective dose of 27 % compared to mAsTCM at 70 kV, it is 25 % for 100 kV, 24 % for 120 kV, and only about 23 % for 150 kV. In the thorax region, for noTCM, no significant difference across the tube voltages can be observed. Compared to mAsTCM, it is about 17 % to 19 % across all tube voltages. The results for riskTCM decrease with increasing tube voltages from a potential effective dose reduction of 23 % at 70 kV to a effective dose reduction of 18 % at 150 kV compared to mAsTCM. For the abdomen, noTCM shows no significant difference across all tube voltages. The effective dose increase compared to mAsTCM is about 15 % to 16 % across the four tube voltages. On the other hand, using the new riskTCM approach, results in an expected effective dose reduction about 32 % for 70 kV compared to mAsTCM. This values decreases with increasing tube voltage. For 100 kV, the potential effective dose reduction is about 29 %, while its is around 27 % for 120 kV and 26 % for 150 kV.

Table 4.2: Relative effective dose values for the different TCM approaches given for all investigated body regions. The values are normalized to the case of mAsTCM. Image noise and thus image quality is kept constant. The results are averaged over all patients and given for 70 kV, 100 kV, 120 kV, and 150 kV. The error is given as the standard deviation over the patients.

	Method	70 kV	100 kV	120 kV	150 kV
Head+Arms	noTCM	**170 %** ± 13 %	**171 %** ± 19 %	**165 %** ± 19 %	**165 %** ± 17 %
	mAsTCM	**100 %**	**100 %**	**100 %**	**100 %**
	riskTCM$_{avg}$	**95 %** ± 2 %	**95 %** ± 2 %	**96 %** ± 2 %	**95 %** ± 3 %
	riskTCM$_{mix}$	**90 %** ± 2 %	**89 %** ± 2 %	**91 %** ± 3 %	**91 %** ± 4 %
	riskTCM	**88 %** ± 5 %	**87 %** ± 5 %	**89 %** ± 5 %	**89 %** ± 5 %
Head	noTCM	**111 %** ± 10 %	**110 %** ± 11 %	**111 %** ± 10 %	**110 %** ± 10 %
	mAsTCM	**100 %**	**100 %**	**100 %**	**100 %**
	riskTCM$_{avg}$	**97 %** ± 2 %	**97 %** ± 2 %	**98 %** ± 2 %	**98 %** ± 2 %
	riskTCM$_{mix}$	**91 %** ± 4 %	**91 %** ± 3 %	**93 %** ± 3 %	**93 %** ± 3 %
	riskTCM	**87 %** ± 6 %	**88 %** ± 6 %	**89 %** ± 4 %	**89 %** ± 4 %
Neck	noTCM	**242 %** ± 40 %	**263 %** ± 45 %	**231 %** ± 39 %	**222 %** ± 33 %
	mAsTCM	**100 %**	**100 %**	**100 %**	**100 %**
	riskTCM$_{avg}$	**89 %** ± 6 %	**91 %** ± 4 %	**93 %** ± 2 %	**91 %** ± 3 %
	riskTCM$_{mix}$	**78 %** ± 8 %	**81 %** ± 7 %	**83 %** ± 5 %	**82 %** ± 6 %
	riskTCM	**73 %** ± 9 %	**75 %** ± 8 %	**76 %** ± 8 %	**77 %** ± 7 %
Thorax	noTCM	**118 %** ± 8 %	**119 %** ± 8 %	**118 %** ± 7 %	**117 %** ± 6 %
	mAsTCM	**100 %**	**100 %**	**100 %**	**100 %**
	riskTCM$_{avg}$	**94 %** ± 2 %	**96 %** ± 2 %	**96 %** ± 2 %	**95 %** ± 4 %
	riskTCM$_{mix}$	**84 %** ± 5 %	**86 %** ± 4 %	**87 %** ± 3 %	**87 %** ± 6 %
	riskTCM	**77 %** ± 6 %	**79 %** ± 5 %	**81 %** ± 5 %	**82 %** ± 5 %
Abdomen	noTCM	**115 %** ± 14 %	**115 %** ± 13 %	**116 %** ± 13 %	**116 %** ± 13 %
	mAsTCM	**100 %**	**100 %**	**100 %**	**100 %**
	riskTCM$_{avg}$	**92 %** ± 3 %	**94 %** ± 2 %	**93 %** ± 3 %	**94 %** ± 2 %
	riskTCM$_{mix}$	**77 %** ± 7 %	**80 %** ± 5 %	**81 %** ± 4 %	**82 %** ± 4 %
	riskTCM	**68 %** ± 7 %	**71 %** ± 6 %	**73 %** ± 6 %	**74 %** ± 5 %
Pelvis	noTCM	**155 %** ± 20 %	**155 %** ± 21 %	**153 %** ± 18 %	**154 %** ± 18 %
	mAsTCM	**100 %**	**100 %**	**100 %**	**100 %**
	riskTCM$_{avg}$	**93 %** ± 2 %	**94 %** ± 2 %	**95 %** ± 2 %	**95 %** ± 2 %
	riskTCM$_{mix}$	**80 %** ± 7 %	**82 %** ± 7 %	**85 %** ± 6 %	**85 %** ± 5 %
	riskTCM	**73 %** ± 9 %	**74 %** ± 8 %	**79 %** ± 7 %	**79 %** ± 7 %

For the last case of the pelvis region, a similar pattern can be seen. For noTCM, there seems to be no significant difference across the tube voltages, similar to riskTCM$_{\text{avg}}$. In particular, for noTCM, an increase of effective dose of about 53 % to 55 % is needed across the tube voltages. For riskTCM, the potential effective dose reduction compared to mAsTCM, is 27 % for 70 kV, 26 % for 100 kV and around 21 % for 120 kV and 150 kV.

4.3 riskTCM Compared to Organ–Specific TCM

In this section, results are shown for noTCM, mAsTCM, riskTCM, and the two organ–specific tube current modulation techniques osTCM$_{0\,\%}$ and osTCM$_{25\,\%}$. The resulting effective dose and dose to the breast values are given in table 4.3 over all patients. In this section, the results focus on the thorax since a special focus of osTCM methods is the reduction of dose to the breast. The results in the table are again all given relative to mAsTCM. Considering the effective dose values, it can be seen that noTCM increases the effective dose around 16 % to achieve the same image noise. With osTCM$_{25\,\%}$, the effective dose can be reduced about 5 % compared to mAsTCM. Using osTCM$_{0\,\%}$, the effective dose can be even further reduced by about 9 %. The highest potential effective dose reduction is seen for riskTCM. About 23 % of effective dose can be reduced over mAsTCM. The breast dose values are also listed relative to mAsTCM. With noTCM, about 8 % more dose is absorbed in the breast. osTCM$_{25\,\%}$ can decrease the breast dose by about 23 % compared to mAsTCM, while osTCM$_{0\,\%}$ decreases the breast dose even further by about 30 % compared to mAsTCM. Using riskTCM, the highest breast dose reduction can be observed. On average, about 51 % of breast dose can be spared compared to mAsTCM at the same image quality.

Table 4.3: Relative effective dose values as well as D_{Breast} values for noTCM, mAsTCM, osTCM$_{25\,\%}$, osTCM$_{0\,\%}$, and riskTCM curves for the chest region. The values are normalized to the case of mAsTCM. Image noise and thus image quality is kept constant. The results are averaged over all patients and given for 70 kV. The error is given as the standard deviation over the patients.

TCM method	Effective dose D_{eff}	Dose to the breast D_{Breast}
noTCM	**116 %** ± 7%	**108 %** ± 8%
mAsTCM	**100 %**	**100 %**
osTCM$_{25\,\%}$	**95 %** ± 4%	**77 %** ± 6%
osTCM$_{0\,\%}$	**91 %** ± 6%	**70 %** ± 8%
riskTCM	**77 %** ± 5%	**49 %** ± 9%

Two exemplary patient acquisitions are also presented in this section. The first example is shown in figure 4.7. The images show the same image noise of about 50 HU. In the upper row, the reconstructions for noTCM, mAsTCM, and osTCM$_{0\,\%}$ can be seen from left to right. The lower row shows the reconstructions for osTCM$_{25\,\%}$, riskTCM, as well as the organ segmentations for this slice. The mAs–, D_{eff}, and D_{Breast} values are

given relative to mAsTCM. There are again two rows with values per image. The first row in white represents the values for the case of a constant image noise as shown in the images. The second row in gray presents the values for the case of a constant effective dose. For the case of a constant image noise, noTCM requires about 8 % more D_{eff} and D_{Breast} to achieve the same image quality as mAsTCM. In the case of osTCM$_{0\,\%}$, the effective dose reduction is about 13 % while the reduction of the breast dose is about 31 %. For osTCM$_{25\,\%}$, the D_{eff} and D_{Breast} reduction is less than for osTCM$_{0\,\%}$. Compared to mAsTCM, D_{eff} can be reduced by about 9 % while D_{Breast} can be reduced about 24 %. For riskTCM, the highest reduction of D_{eff} and D_{Breast} can be seen relative to mAsTCM. The effective dose can be reduced by about 25 % and the dose to the breast about 58 % in this case. For the case of constant effective dose, the noTCM

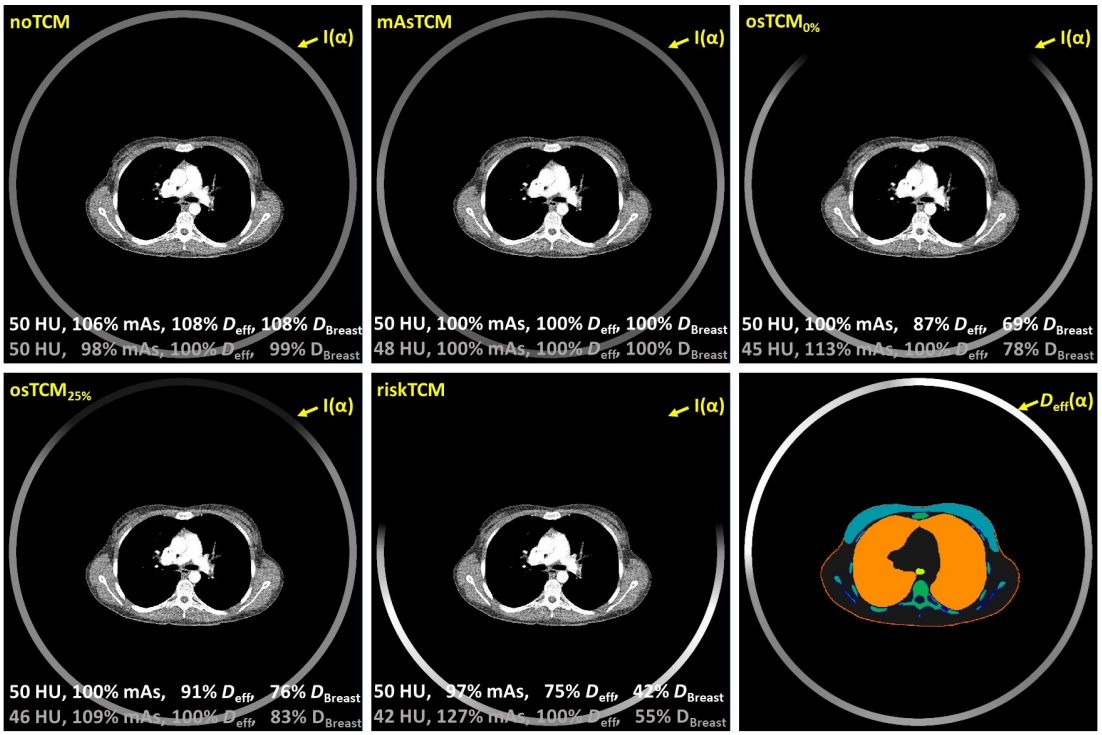

Figure 4.7: noTCM, mAsTCM, osTCM$_{0\%}$, osTCM$_{25\,\%}$ and riskTCM images (C = 25 HU, W = 400 HU) as well as the segmented organs for an exemplary thorax/breast examination. The layout is similar to figure 4.1.

acquisition shows about 50 HU of image noise while mAsTCM only shows about 48 HU. The image noise for osTCM$_{0\,\%}$ is reduced to 45 HU while the breast dose can still be reduced by about 22 % compared to mAsTCM. For osTCM$_{25\,\%}$, image noise is about 46 HU while D_{Breast} is about 17 % reduced compared to mAsTCM. For riskTCM, the lowest image noise can be observed. At a noise level of about 42 HU, the breast dose still is reduced by about 45 % compared to mAsTCM.

The second patient is shown in figure 4.8. The images are again all shown at the

same image noise of about 50 HU. For noTCM, about 4 % more D_{eff} and D_{Breast} are required to achieve the same image noise. For osTCM$_{0\,\%}$, the effective dose and the breast dose can be reduced by about 11 % and 37 %, respectively. With osTCM$_{25\,\%}$, the effective dose can be reduced by about 9 % compared to mAsTCM while the breast dose can be reduced by about 28 %. Using riskTCM results in an effective dose reduction of about 20 % and an D_{Breast} reduction of about 62 % in this particular case. For the case of constant effective dose, the noTCM acquisition shows an image noise of 50 HU while the mAsTCM image has an image noise of 49 HU. With osTCM$_{0\,\%}$, the image noise can be reduced to 46 HU while still reducing the dose to the breast by about 30 % compared to mAsTCM. Using osTCM$_{25\,\%}$ results in an image noise of 47 HU while reducing D_{Breast} by about 21 % for this case. With riskTCM, the lowest image noise of 44 HU is seen. Here, also the reduction of the breast dose is still about 53 % compared to mAsTCM.

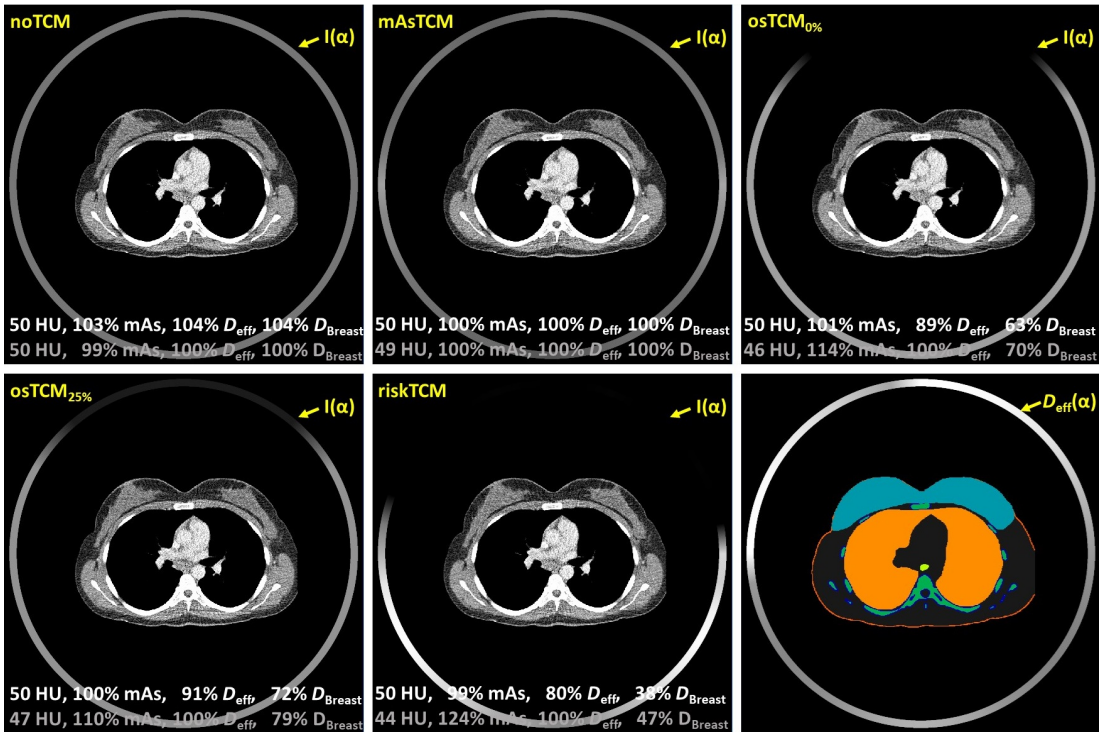

Figure 4.8: noTCM, mAsTCM, osTCM$_{0\%}$, osTCM$_{25\,\%}$ and riskTCM images (C = 25 HU, W = 400 HU) as well as the segmented organs for a second example patient. The layout is the same as in figure 4.7.

4.4 Extension to Spiral Trajectory

In the following, reconstructions for an extension of riskTCM to a spiral trajectory according to section 3.3 are shown. Figure 4.9 shows coronal images for one patient

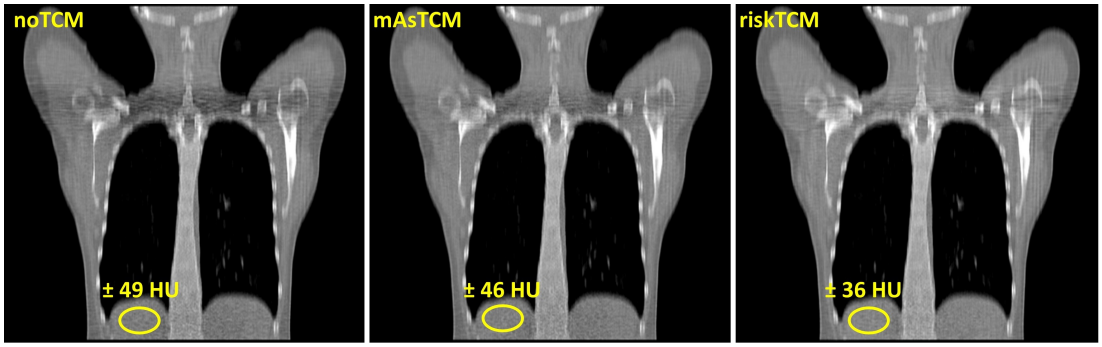

Figure 4.9: Coronal reconstructions for noTCM, mAsTCM, and riskTCM (C = 0 HU, W = 1500 HU) at the same effective dose for a spiral scan with a pitch of 0.5 and a tube voltage of 70 kV. For the yellow ROI, the noise is given for the three reconstructions.

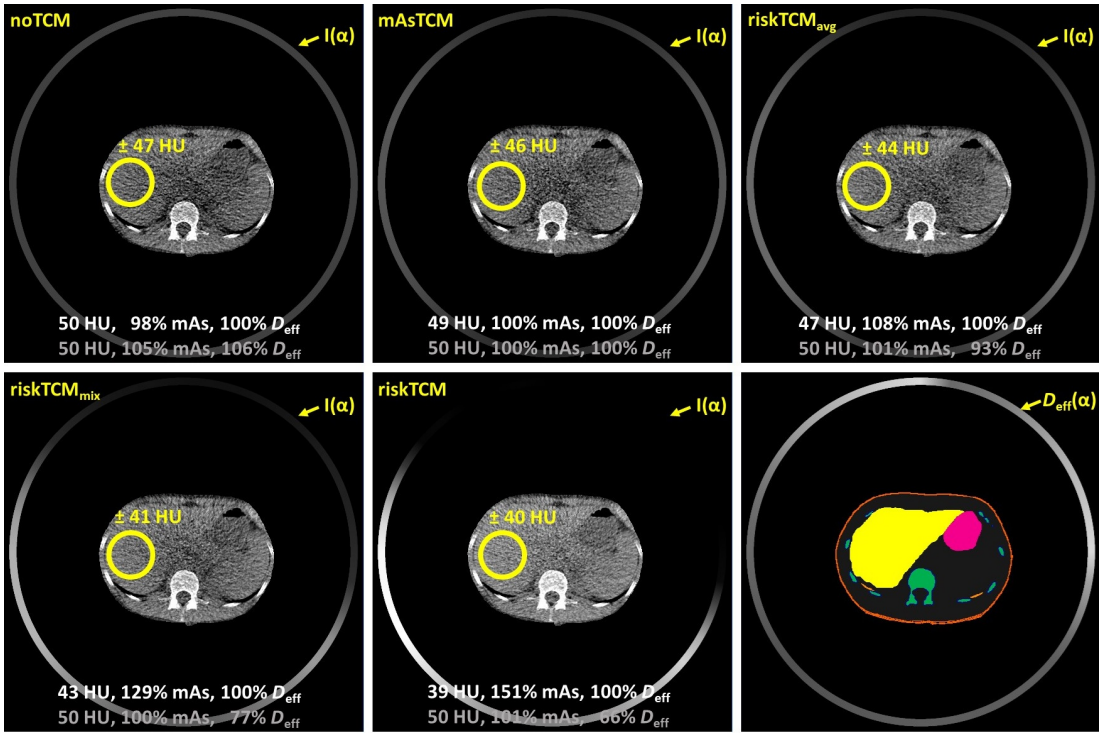

Figure 4.10: Reconstructions for noTCM, mAsTCM, riskTCM$_{avg}$, riskTCM$_{mix}$, and riskTCM (C = 25 HU, W = 400 HU) at the same effective dose for a spiral scan for one exemplary axial slice in the abdomen. Also, the organ segmentation is given for this particular slice. The layout is similar to figure 4.1. The tube voltage has been chosen to be 70 kV, the pitch value is 0.5. The values given in the white and gray row represent the values from the corresponding circular scan. The images and the noise given in the ROI correspond to the spiral reconstructions.

using three different tube current modulation methods. From left to right, noTCM, mAsTCM, and riskTCM are shown. These reconstructions are shown at the same effective dose. The noise in one example ROI is about 49 HU for noTCM, 46 HU for mAsTCM and 36 HU for riskTCM. Of particular interest in these images are the streak artifacts in the region of the shoulders. While they are very prominent in the noTCM image, they are significantly reduced in the mAsTCM and riskTCM reconstructions. Note that the images show a rather low spatial resolution in longitudinal direction since several slices are averaged in a running manner to obtain a noise free ground truth, as discussed in section 3.3.

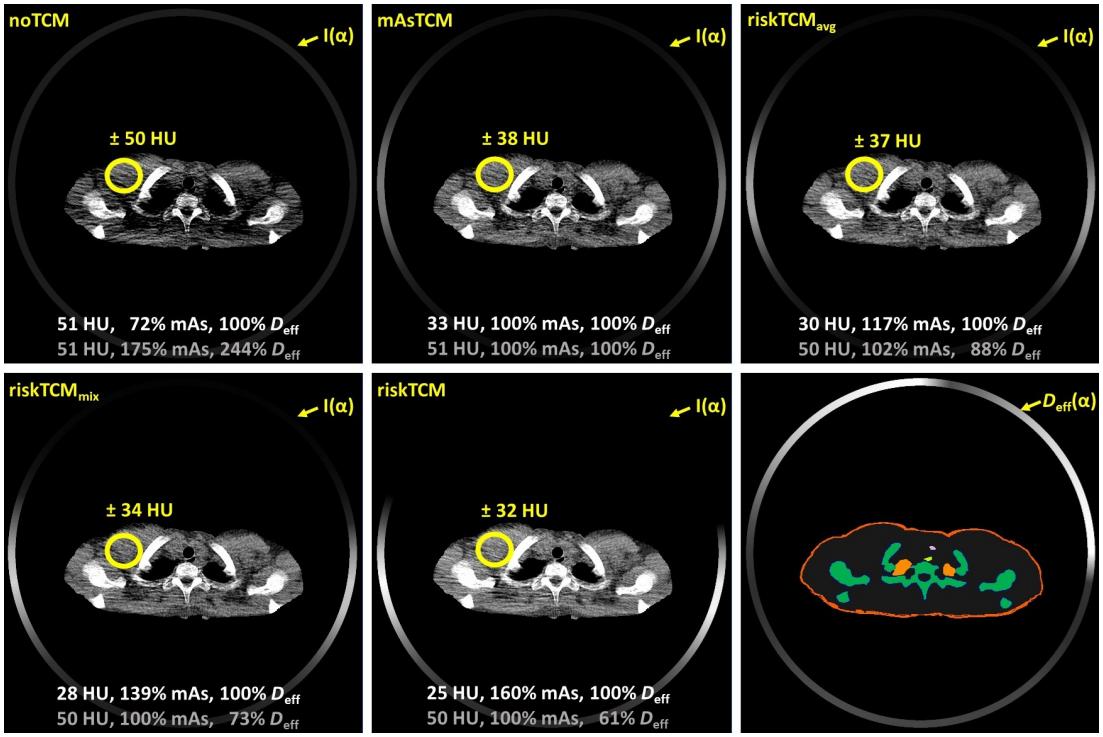

Figure 4.11: Reconstructions for noTCM, mAsTCM, riskTCM$_{avg}$, riskTCM$_{mix}$, and riskTCM (C = 25 HU, W = 400 HU) at same effective dose for a spiral scan with a pitch value of 0.5 for one exemplary axial slice through the shoulders. Also, the organ segmentation is given for this particular slice. The layout is similar to figure 4.1. The tube voltage is 70 kV.

In Figure 4.10, an example axial slice from the abdomen is shown. For an example ROI, the noise is provided. For noTCM, the noise in this ROI is about 47 HU, while it is 46 HU in the mAsTCM acquisition, 44 HU in the riskTCM$_{avg}$ reconstruction, and 41 HU in the riskTCM$_{mix}$ image. The lowest noise of 40 HU can be seen for riskTCM. Noise has also been evaluated in the difference image between the quasi–noise free image and the particular TCM reconstruction. Therefore, the noise in the patient has been evaluated for 20 slices in the abdomen and averaged. The resulting noise is 35 HU using

noTCM, 34 HU for mAsTCM, 33 HU with riskTCM$_{avg}$, and 32 HU with riskTCM$_{mix}$. With riskTCM, the noise is about 31 HU, on average.

A similar approach has been taken for the shoulders. An example image can be seen in figure 4.11. All images are shown at the same effective dose. The noise in a specific ROI is again shown for all five TCM methods evaluated herein. In this case, the noise using the noTCM method is the highest with 50 HU. With mAsTCM, about 38 HU can be achieved. Using riskTCM$_{avg}$, the noise reduces to 37 HU while it is about 34 HU for riskTCM$_{mix}$. Using riskTCM results in the lowest noise of 32 HU. Additionally, noise has been evaluated in the difference image for 10 slices in this region of the shoulders. The noise has been evaluated in a ROI covering the whole patient. This approach results in a noise of 41 HU in the difference image by using noTCM. With mAsTCM, the noise is about 32 HU. Using riskTCM$_{avg}$, and riskTCM$_{mix}$ results in an image noise of 31 HU and 28 HU, respectively. With riskTCM, the average noise is reduced to 27 HU.

4.5 Phantom Measurements

Figure 4.12 shows an example slice of the abdomen phantom for noTCM, mAsTCM, riskTCM$_{avg}$, riskTCM$_{mix}$ and riskTCM.

Effective dose and mAs–values are given for the case of constant noise as well as constant effective dose. As mentioned in section 3.4, the images shown in figure 4.12 are generated by combining the different projections of several measurements acquired with different dose levels according to the TCM curves. The values in the white and gray rows in the images give the predicted values for the simulated circular scans. The noise given in the yellow ROIs has been solely measured in the images. Therefore, these values differ from each other. Interpolation between the eight measurements has been used to compute images according to the different TCM methods. Furthermore, the lowest tube current used was 5 mAs. For the case of constant effective dose, the noTCM ROI has an image noise of 25 HU while mAsTCM and riskTCM$_{avg}$ have 24 HU, and 23 HU, respectively. In the riskTCM$_{mix}$ ROI, the noise is 22 HU and riskTCM has the lowest noise of 21 HU. For the case of constant noise, noTCM requires about 12 % more effective dose compared to mAsTCM. With riskTCM$_{avg}$ and riskTCM$_{mix}$, about 1 % of effective dose can be spared, respectively 4 %. With riskTCM, the effective dose reduction is about 9 %. Since the semi–anthropomorphic phantoms are missing several organs and the available organs such as the bones are not very realistic, the effective dose values can hardly be compared to the patient simulations shown before. Nevertheless, this example can be used to illustrate the difference between mAsTCM and riskTCM once more. In case of mAsTCM, it is obvious that the tube current is increased for lateral views while it is decreased for a.p. views. In this particular example, however, the liver as a major organ at risk is placed asymmetrically in the abdomen. Hence, using the same increased tube current for left– and right–lateral views is obviously not optimal in terms of effective dose. This drawback is overcome by using riskTCM. It is evident from the figure that in this example the liver is spared and tube current is primarily increased on the patient left side, i.e., in views not directly exposing the liver.

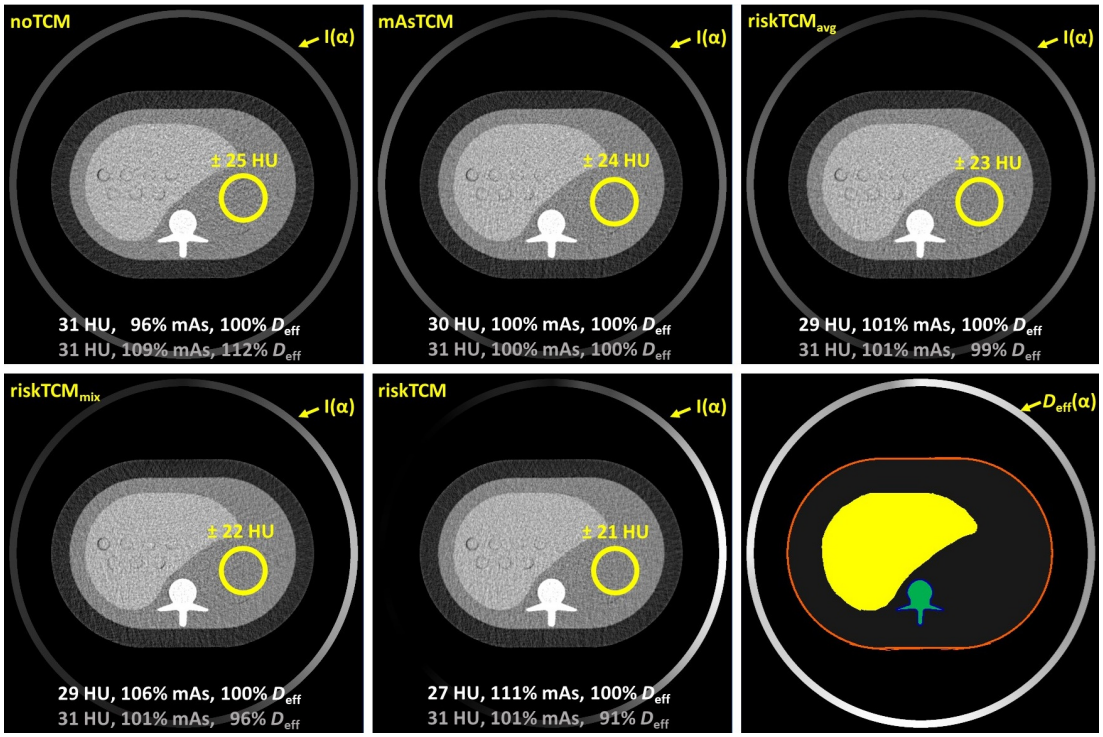

Figure 4.12: Reconstructions for noTCM, mAsTCM, riskTCM$_{\text{avg}}$, riskTCM$_{\text{mix}}$, and riskTCM (C = 25 HU, W = 400 HU) at same effective dose for an example slice of the abdomen phantom. The layout is similar to figure 4.1. Also, the organ segmentation is given for this particular slice. The values in the white and gray rows in the images show the predicted values for the simulated circular scans. The noise values given for the yellow ROIs have been measured in the images.

5 Discussion

In the following, several aspects regarding riskTCM are discussed more throughout. For a better overview, the following discussion is divided into four sections. First, the potential effective dose reduction of riskTCM with regard to different body regions and tube voltages is summarized and analyzed. Afterwards, the limitations of these studies are discussed. The next section is dedicated to the optimization of riskTCM, especially to the optimization of minimizing the riskTCM cost function. In the last section, the dose problematics coming with riskTCM are discussed.

5.1 Potential Effective Dose Reduction with riskTCM

The results for the novel patient–specific tube current modulation algorithm presented herein indicate that patients can greatly benefit from riskTCM. However, the amount of effective dose reduction depends on the anatomical region. The head, with or without arms, shows a smaller effective dose reduction than other regions compared to the current clinical gold standard of mAsTCM. This may be due to the composition of human tissue in this region. The head is rather circular in shape and the organs at risk, such as the brain, are more or less uniformly distributed. In both cases, head with or without arms, the effective dose reduction potential of riskTCM is around 12 % to 13 % over mAsTCM, for 70 kV.

A higher effective dose reduction can be achieved in the neck region. A prominent organ of risk in this region is the thyroid gland which is very sensitive to radiation and is located at the anterior side of the patient. The conventional mAsTCM method is already able to reduce the effective dose in this scenario significantly, because the human anatomy is highly inhomogeneous in this region. This results in the lateral views receiving much higher tube current values than anterior and posterior views. However, riskTCM, is able to increase the dose reduction potential even further by reducing the tube current anterior to the patient. For the case of 70 kV, approximately 27 % can be saved compared to mAsTCM while maintaining image quality.

For the thorax and abdomen, mAsTCM is not able to reduce the effective dose as much as for the neck region compared to noTCM. This is because the patient is relatively circular shaped in these regions. Therefore, the modulation is not as pronounced. However, since many organs at risk are located at the anterior side of the patient, such as the the breast, stomach or liver, riskTCM can greatly benefit the patient with effective dose reductions of up to 23% for the thorax and 32 % for the

abdomen compared to mAsTCM for a tube voltages of 70 kV. Abdominal scans are typically performed at rather high dose levels to reduce noise and increase soft tissue contrast. Furthermore, several consecutive abdominal scans are performed to visualize contrast agent kinetics, e.g., to image the liver in both the arterial as well as the venous phase. This makes the potential dose reduction of riskTCM even more important since it could either be used to actually reduce effective dose or to reduce image noise at the same effective dose and thus to increase diagnostic confidence. The use of riskTCM can also be beneficial in examinations of the pelvis. The effective dose reduction in these cases is about 27% on average compared to mAsTCM.

In addition, two other approaches of patient risk–minimizing TCMs were evaluated, namely riskTCM$_{\text{avg}}$ and riskTCM$_{\text{mix}}$. The riskTCM$_{\text{avg}}$ method does not include the optimal weighting of redundant rays in the used cost function. Therefore, its dose reduction potential is lower compared to riskTCM. Using riskTCM$_{\text{avg}}$ reduces the effective dose by about 6 % to 11 % from the neck to the pelvis and by about 3 % to 5 % for the head compared to mAsTCM. The riskTCM$_{\text{mix}}$ algorithm calculated the tube current curves from the tube current curves of riskTCM and riskTCM$_{\text{avg}}$ in equal parts. The effective dose reduction for riskTCM$_{\text{mix}}$ is about 9 % to 23 %, for 70 kV.

Furthermore, the choice of tube voltage and its effect on the potential effective dose reduction was evaluated. A slight decrease in effective dose reduction can be observed with increasing tube voltage. However, even for the highest tube voltage investigated, 150 kV, the effective dose reduction potential of riskTCM compared to mAsTCM is still high. For the head with and without arms, it is about 11 % compared to 12 % to 13 % at 70 kV. The neck region shows a decrease from 27 % to 23 % when switching from lowest to highest tube voltage. For the pelvis, the values are similar. Compared to an effective dose reduction of 27 % at 70 kV, the effective dose reduction compared to mAsTCM is only about 21 % at 150 kV. For the thorax, the effective dose reduction is about 23 % at 70 kV and 18 % at 150 kV. In the abdomen, the effective dose reduction is about 32 % at 70 kV and decreases to 26 % at 150 kV. This overall reduction of effective dose reduction in riskTCM can be explained by the weighting of redundant rays. The higher the tube voltage, the higher the effective energy of the emitted spectra. This also means that the contribution of effective dose by each complementary ray is increasingly similar with increasing tube voltage, since the penetration depth of the used radiation increases as well. Hence, at higher tube voltages, complementary rays are weighted more equally whereas at lower tube voltages, one of the rays might receive a significantly higher weight than the other. The high potential effective dose reduction also makes it of interest for programs such as lung cancer screening since the dose of such examinations has to be particular low in order to justify the diagnostic value.

Since some organ–specific TCM methods are already clinically available, it was also of interest to compare riskTCM to these methods. Therefore, the XCare algorithm (Siemens Healthineers, Forchheim, Germany) was chosen as a reference method since its design is disclosed in the literature. This algorithm reduces the tube current for predefined angles anterior to the patient and increases it for the posterior angles while the overall mAs–product is constant. It is therefore not patient–specific. The main goal of this approach is to spare sensitive organs such as the female breast. For this

reason, only female chest scans were evaluated in this particular part of the study. The organ–specific methods do not seem to reduce the overall effective dose to the patient as much as riskTCM compared to conventional TCM methods. Up to 9 % of effective dose could be saved, on average, compared to a dose reduction of 23 % with riskTCM. However, the specific dose to the breast can be reduced by 23 % to 30 % compared to mAsTCM using these organ–specific methods. When riskTCM is used, the dose to the breast is reduced even further. About 51 % of the breast dose can be saved with the algorithm, highlighting the potential clinical benefit of the proposed method.

5.2 Limitations

The first parts of the evaluation of riskTCM are limited to circular scans. However, in clinical practice, spiral scans are more common. Therefore, as a proof of principle, a first translation of riskTCM to spiral trajectories was implemented. To estimate the tube current values, many circular scans with a very narrow z–spacing were computed. The tube current values could then be obtained by interpolating between the tube current values for the circular scans according to the spiral trajectory. This was done for two exemplary patients. The results indicate that the translation of riskTCM to spiral scans is possible. However, since a major advantage of riskTCM is the use of redundant rays, the best results for dose reduction can only be expected at low pitch values, since otherwise the existence of at least two complementary rays cannot be guaranteed. Further studies might investigate the influence from parameters such as the start angle of the spiral acquisition on the possible dose reduction potential. Another point that could be of interest is to include the tube current inertia and evaluate if it might influence the overall potential dose reduction.

Another limitation is that no real measurements can be performed yet, as this would require the modification of a medical product which cannot be done without the help of manufacturers. At present, a collaboration with Siemens Healthineers has been initiated to provide the necessary access to the system and updated reconstruction software, but this will need to be evaluated in future research and is outside the scope of this thesis. However, first phantom measurements have been performed herein, which used real measurements of different dose levels and combined the projections such that one CT volume is calculated which represents a volume that would have been acquired with a certain TCM curve. Besides the fact that the resulting dose reduction values are hardly comparable to the patient study since many radiation sensitive organs are missing and the phantoms are just rudimentary representations of human anatomy, this approach shows that translation to clinical practice generally seems to be possible.

A very important advantage of riskTCM is the fact that it can be implemented on any CT scanner that is capable of tube current modulation, which is almost every system in clinical use today. Therefore, no major hardware updates to the CT systems are required to implement riskTCM. However, some software updates will be required, since a rough organ segmentation and dose distribution will be needed before the actual CT scan to calculate the ideal riskTCM curve for a specific patient.

5.3 Optimizing riskTCM

Also, the method for optimization of the riskTCM curves could be a topic of future research. Since the new riskTCM cost function needs to be solved numerically, the Nelder Mead method [110] has been used in this study. Its advantage is its simplicity since it does not require an explicit computation of the derivatives of the objective function. However, since calculating the derivatives of the riskTCM cost function is possible, other optimization approaches might show a better performance or improved stability. The former is particularly relevant in clinical practice. In such a case, the riskTCM curve must be obtained as fast as possible and suitable methods to achieve this goal need to be found. These optimizations might be manifold. For once, an optimization of the cost function might be possible, for example by performing all computations on a downsampled version of the used volume or by implementing all relevant computations on a graphics processing unit (GPU). Another potential way of improving riskTCM is by using more advanced optimization algorithms. Recently, several algorithms have shown remarkable performance in terms of improved convergence and stability as well as reduced computational demands over classic methods in disciplines such as engineering and machine learning. Examples include but are not limited to the Stochastic Gradient Descent method [113] or the limited–memory Broyden–Fletcher–Goldfarb–Shanno (BFGS) algorithm [114]. Alternatively, one might consider improved versions of classical algorithms, such as a preconditioned conjugated gradient method [115] or Nesterov's algorithm [116]. All of these methods might be suitable to provide the convergence speed required in clinical practice and a particular candidate should be chosen after careful consideration. A drawback of all afore–mentioned optimization methods is the fact that they rather seek to find local optima rather than global ones. However, this issue can be mitigated by using appropriate starting points for optimization. E.g., in case of riskTCM, the mAsTCM curve is used as an initial guess. Another approach might be to only use a very limited, random number of projections to estimate a good initial guess to the riskTCM curve using a performance–efficient Bayesian optimization approach [117].

Another point that requires further attention and evaluation is the prior knowledge required to calculate the optimal riskTCM curve. Herein, instead of using only the topograms, CT images and a mostly manual segmentation of the organs were used. The novel riskTCM algorithm requires an estimation of the organ doses as a function of the source position. One possible idea for a potential clinical workflow with riskTCM would be to estimate a dose distribution and segmentation based on an estimated CT volume from the topogram(s) using neural networks. However, the required accuracy of these intermediate steps would need to be thoroughly investigated. This applies in particular to the quality of segmentations obtained from the coarse estimate of the patient volume. However, the convex hull of objects such as the body outline or of bones can be extracted well from projections at a low computational cost. Such information could be used as initial guess for further organ segmentations or as a means of regularisation. However, it is much more difficult to segment organs such as the colon or the salivary glands and potential segmentation methods have to be studied thoroughly. In addition, alternatives

should be investigated. For example, it might be advantageous to train a neural network to estimate organ doses per projection directly from the topogram(s). Another idea could be to replace conventional topograms with ultra–low–dose CT scans which could facilitate the estimation of dose distribution and organ segmentation.

5.4 Dose Considerations

A barrier for the implementation of riskTCM in clinical CT systems may be that legal regulations require the CTDI– and DLP–values to be reported for each CT scan. As seen in the results, minimizing patient–specific risk measures such as the effective dose may result in an increase of the total mAs–product. However, an increase of the total mAs–product also results in an increase of CTDI and DLP. It is therefore important to consider how to actually implement riskTCM in clinical practice and how to communicate the resulting patient dose. The current approach of reporting CTDI– and DLP–values has the advantage that since these measures are based on standardized phantoms, the values are comparable between different CT protocols and CT scanners. These values can be reported easily, e.g., in publications and can be used to at least compare tube outputs among different scanners. However, since measures such as organ doses or the effective dose are patient–specific, and also the potential effective dose reduction will vary between different patient anatomies, reporting these values on a per–scanner basis would not be meaningful. Quantities such as organ and patient dose should always be related to a specific patient or at least a particular patient population and require the tracking of additional information, such as patient habitus and size. While these information are often available in clinical practice, their collection in larger dedicated databases and a consequent reporting might raise data protection concerns that would need to be addressed. The afore–mentioned potential increase of CTDI and DLP due to riskTCM would also require a modification of software interfaces. It is imaginable that the estimation of effective doses used to compute the riskTCM curve are presented to the technician or physician along with CTDI and DLP after the acquisition of the topogram and prior to the actual scan. This would provide clinical experts not only with information of the tube output, e.g., CTDI, but also with an estimate for actual patient dose and would potentially reduce the restrain to apply a scan protocol that increases CTDI.

Finally, it should be emphasized that the effective dose used as surrogate for patient risk in this thesis, is just one exemplary measure for patient risk. The riskTCM algorithm can easily be adapted to other risk measures. For example, it is conceivable to include additional organs, or to optimize only for certain organs of interest selected by the physician prior to the CT scan. As the concept of effective dose is widely used [118], it has been chosen as a risk measure to demonstrate the potential benefits of riskTCM. However, even the effective dose is not a constant concept, as new re–estimates of tissue weighting factors and the addition of new organs are published from time to time.

Furthermore, the effective dose and its tissue weighting factors are only meant to control occupational exposure, therefore there is no distinguishing between different ages, sexes or other factors. However, looking at an individual patient, these differences

should not be ignored. For example, studies indicate that the risk for the female breast to develop cancer is significantly higher than for the male breast [82], [119], [120]. Also for other organs such as the thyroid gland or lung cancer, the radiation induced risk seems to vary between male and female patients.

However, in scope of this measure, riskTCM outperforms all other considered tube current modulation methods, including the current clinical gold standard of mAsTCM.

6 | Summary and Outlook

The introduction of tube current modulation techniques into clinical practice more than 20 years ago has greatly benefited clinical CT. However, the approaches of these techniques are not driven by the actual minimization of patient risk. Rather, classical tube current modulations minimize the tube current–time product based on the observed intersection lengths through the patient. In general, the tube current is increased for projections with high attenuation, for example in the case of lateral projections through the shoulders, and decreased in areas of low absorption. This allows the total tube current to be reduced and the noise texture to be more homogeneous, particularly in regions of asymmetric patient cross–sections. However, other regions of the body such as the abdomen or thorax, benefit much less from this approach. In addition, there are also organ–specific TCM approaches that are clinically available. These approaches are rather simple and not patient–specific. For example, they reduce the tube current anterior to the patient for predefined angles and increase it for the other angles to maintain image quality. The aim is to save dose to specific organs such as the breast or eye lenses.

The patient risk–minimizing tube current modulation approach presented in this work uses an initial estimate of the patient's anatomy which can be obtained, for example, by neural networks from the acquired topograms, to identify all relevant anatomical structures and organs in the field of measurement. Based on this, the optimal tube current curve for the patient is calculated, minimizing both the resulting image noise and the radiation exposure to the patient in terms of the effective dose. Using a simulation study, this work provides evidence that riskTCM could greatly benefit patients in clinical practice. For the case of 70 kV, on average, about 12 % of effective dose can be reduced compared to the current gold standard of mAsTCM for the head with arms while the dose reduction potential for the head without arms is about 13 %. For the neck, about 27 % of D_{eff} reduction can be expected. For the thorax and the pelvis, the D_{eff} reduction is about 23 % and 27 %, respectively. The highest effective dose reduction potential compared to mAsTCM was found for the abdomen with 32 %.

The influence of the choice of tube voltage on the dose reduction potential of riskTCM is not very dominant. However, there seems to be a small decrease in dose reduction with increasing tube voltage, with the highest effective dose reduction values for 70 kV. For example, the effective dose reduction in the thorax region is about 23 % for riskTCM compared to mAsTCM for 70 kV, while it is about 18 % at 150 kV.

In a next step, riskTCM was compared with a conventional clinically available organ–

specific TCM in terms of effective dose reduction potential as well as breast dose reduction. It was found that while $\text{osTCM}_{0\%}$ and $\text{osTCM}_{25\,\%}$ reduce the effective dose by about 5 % to 9 % and the dose to the breast by about 23 % to 30 % compared to mAsTCM, riskTCM can further reduce these values. Compared to mAsTCM, about 23 % of effective dose can be saved while the breast dose can be reduced by about 51 %. This, for example, might allow for the design of novel applications in CT such as dedicated imaging of the female breast.

The dose reduction values were estimated using circular full scans. Here, riskTCM benefits from the presence of redundant rays. However, a first proof–of–principle study in this work also showed that riskTCM can also benefit patients when a spiral trajectory is used, at least for scans with low pitch values. Dose reduction for scans with higher pitch values would need to be the subject of further research. In addition to optimizing scans with spiral trajectory and higher pitch values the effect of the chosen start angle of the spiral on dose reduction should be investigated.

Potential future research topics based on the riskTCM framework are manifold. One example might be the extension of the algorithm to the simultaneous optimization of tube current, tube voltage and prefilter, on a per–view basis. Such an approach might allow for an even higher reduction of effective dose, in particular when contrast media are present in the field of measurement. However, the clinical implementation of this simultaneous modulation of tube current, voltage and prefilter would most likely require hardware modifications since neither tube voltage nor prefilter thickness can be continuously modulated in today's systems. Another topic of future research might be the adaption of riskTCM to dedicated protocols and acquisition schemes, e.g., to cardiac imaging. Prospectively gated cardiac CT or ECG–based tube current modulation for retrospectively gated cardiac CT aims at acquiring 180° plus fan angle segments of data. The absence of complementary rays, i.e., the absence of redundant data, implies that dose reduction with risk–based TCM would be significantly lower. A potential optimization for such cardiac exams would be to select the time point (number of heart beats) for the scan start such that the x–ray tube start angle is such that the gated scan minimizes the effective dose to the patient. It should also be noted that the concept of adjusting the exposure parameters in a way that minimizes the patient risk while maintaining image quality can be generalized to hardware that allows to modulate not only a single exposure parameter per projection but rather to modulate the exposure per ray, such as the methods proposed in references [121]–[123]. However, minimizing the effective dose in such a way has not been researched in these studies yet. Such methods are often termed as fluence field modulation but have not made their way into a clinical system, yet. Initial measurements with phantoms indicated that the translation of riskTCM into clinical practice seems to be possible. Nevertheless, for research in the nearer future, it would be of importance to evaluate riskTCM for real measurements. For this, it would be necessary to be able to set a pre–calculated riskTCM curve for a CT system which requires cooperations with system manufacturers.

Finally, it should be mentioned that the developed algorithm is by no means limited to the consideration of the effective dose, but also allows for the use of other specific risk measures. In fact, the effective dose is not an ideal measure as it is not age–, size–

or gender–specific. Hence, future iterations of the riskTCM might exploit more accurate estimates of patient dose and reduce the risk associated with CT examinations even further.

Bibliography

[1] W. C. Röntgen, "Über eine neue Art von Strahlen," *Annalen der Physik*, volume 300, number 1, pages 12–17, 1898.

[2] F. Nüsslin, "Wilhelm Conrad Röntgen: The scientist and his discovery," *Physica Medica*, volume 79, pages 65–68, 2020.

[3] G. N. Hounsfield, "Computerized transverse axial scanning (tomography): Part 1. Description of system," *The British Journal of Radiology*, volume 46, number 552, pages 1016–1022, 1973.

[4] M. M. Lell, J. E. Wildberger, H. Alkadhi, J. Damilakis, and M. Kachelrieß, "Evolution in computed tomography," *Investigative Radiology*, volume 50, number 9, pages 629–644, 2015.

[5] M. Lell and M. Kachelrieß, "Computed tomography 2.0," *Investigative Radiology*, volume 58, number 8, pages 587–601, 2023.

[6] B. Newman and M. J. Callahan, "ALARA (as low as reasonably achievable) CT 2011 – Executive summary," *Pediatric Radiology*, volume 41, number S2, pages 453–455, 2011.

[7] W. Chang, J. M. Lee, K. Lee, J. H. Yoon, M. H. Yu, J. K. Han, and B. I. Choi, "Assessment of a model-based, iterative reconstruction algorithm (MBIR) regarding image quality and dose reduction in liver computed tomography," *Investigative Radiology*, volume 48, number 8, pages 598–606, 2013.

[8] M. Park, Y. E. Chung, H. S. Lee, J.-Y. Choi, M.-S. Park, M.-J. Kim, and K. W. Kim, "Intraindividual comparison of diagnostic performance in patients with hepatic metastasis of full-dose standard and half-dose iterative reconstructions with dual-source abdominal computed tomography," *Investigative Radiology*, volume 49, number 4, pages 195–200, 2014.

[9] H.-C. Becker, D. Augart, M. Karpitschka, S. Ulzheimer, F. Bamberg, D. Morhard, K. Neumaier, A. Graser, T. Johnson, and M. Reiser, "Radiation exposure and image quality of normal computed tomography brain images acquired with automated and organ-based tube current modulation multiband filtering and iterative reconstruction," *Investigative Radiology*, volume 47, number 3, pages 202–207, 2012.

[10] M. Beister, D. Kolditz, and W. A. Kalender, "Iterative reconstruction methods in x-ray CT," *Physica Medica*, volume 28, number 2, pages 94–108, 2012.

[11] P. Prakash, M. K. Kalra, A. K. Kambadakone, H. Pien, J. Hsieh, M. A. Blake, and D. V. Sahani, "Reducing abdominal CT radiation dose with adaptive statistical iterative reconstruction technique," *Investigative Radiology*, volume 45, number 4, pages 202–210, 2010.

[12] D. Marin, K. R. Choudhury, R. T. Gupta, L. M. Ho, B. C. Allen, S. T. Schindera, J. G. Colsher, E. Samei, and R. C. Nelson, "Clinical impact of an adaptive statistical iterative reconstruction algorithm for detection of hypervascular liver tumours using a low tube voltage, high tube current MDCT technique," *European Radiology*, volume 23, number 12, pages 3325–3335, 2013.

[13] W. P. Shuman, K. T. Chan, J. M. Busey, L. M. Mitsumori, E. Choi, K. M. Koprowicz, and K. M. Kanal, "Standard and reduced radiation dose liver CT images: Adaptive statistical iterative reconstruction versus model-based iterative reconstruction – Comparison of findings and image quality," *Radiology*, volume 273, number 3, pages 793–800, 2014.

[14] Y. Hou, X. Liu, S. Xv, W. Guo, and Q. Guo, "Comparisons of image quality and radiation dose between iterative reconstruction and filtered back projection reconstruction algorithms in 256-MDCT coronary angiography," *American Journal of Roentgenology*, volume 199, number 3, pages 588–594, 2012.

[15] R. D. A. Khawaja, S. Singh, M. Gilman, A. Sharma, S. Do, S. Pourjabbar, A. Padole, D. Lira, K. Brown, J.-A. O. Shepard, and M. K. Kalra, "Computed tomography (CT) of the chest at less than 1 mSv," *Journal of Computer Assisted Tomography*, volume 38, number 4, pages 613–619, 2014.

[16] E. J. Halpern, E. L. Gingold, H. White, and K. Read, "Evaluation of coronary artery image quality with knowledge-based iterative model reconstruction," *Academic Radiology*, volume 21, number 6, pages 805–811, 2014.

[17] M. S. May, W. Wüst, M. Brand, C. Stahl, T. Allmendinger, B. Schmidt, M. Uder, and M. M. Lell, "Dose reduction in abdominal computed tomography," *Investigative Radiology*, volume 46, number 7, pages 465–470, 2011.

[18] P. Barca, S. Domenichelli, R. Golfieri, L. Pierotti, L. Spagnoli, S. Tomasi, and L. Strigari, "Image quality evaluation of the precise image CT deep learning reconstruction algorithm compared to filtered back-projection and iDose^4: A phantom study at different dose levels," *Physica Medica*, volume 106, page 102 517, 2023.

[19] M. Lenfant, P.-O. Comby, K. Guillen, F. Galissot, K. Haioun, A. Thay, O. Chevallier, F. Ricolfi, and R. Loffroy, "Deep learning-based reconstruction vs. iterative reconstruction for quality of low-dose head-and-neck CT angiography with different tube-voltage protocols in emergency-department patients," *Diagnostics*, volume 12, number 5, page 1287, 2022.

[20] H. Yoon, J. Kim, H. J. Lim, and M.-J. Lee, "Image quality assessment of pediatric chest and abdomen CT by deep learning reconstruction," *BMC Medical Imaging*, volume 21, number 1, 2021.

[21] Y. Yao, B. Guo, J. Li, Q. Yang, X. Li, and L. Deng, "The influence of a deep learning image reconstruction algorithm on the image quality and auto-analysis of pulmonary nodules at ultra-low dose chest CT: A phantom study," *Quantitative Imaging in Medicine and Surgery*, volume 12, number 5, pages 2777–2791, 2022.

[22] J. Greffier, Q. Durand, J. Frandon, S. Si-Mohamed, M. Loisy, F. de Oliveira, J.-P. Beregi, and D. Dabli, "Improved image quality and dose reduction in abdominal CT with deep-learning reconstruction algorithm: A phantom study," *European Radiology*, volume 33, number 1, pages 699–710, 2022.

[23] J. Greffier, J. Frandon, S. Si-Mohamed, D. Dabli, A. Hamard, A. Belaouni, P. Akessoul, F. Besse, B. Guiu, and J.-P. Beregi, "Comparison of two deep learning image reconstruction algorithms in chest CT images: A task-based image quality assessment on phantom data," *Diagnostic and Interventional Imaging*, volume 103, number 1, pages 21–30, 2022.

[24] J. A. van Stiphout, J. Driessen, L. R. Koetzier, L. B. Ruules, M. J. Willemink, J. W. T. Heemskerk, and A. J. van der Molen, "The effect of deep learning reconstruction on abdominal CT densitometry and image quality: A systematic review and meta-analysis," *European Radiology*, volume 32, number 5, pages 2921–2929, 2021.

[25] Y. Nagayama, M. Goto, D. Sakabe, T. Emoto, S. Shigematsu, S. Oda, S. Tanoue, M. Kidoh, T. Nakaura, Y. Funama, R. Uchimura, S. Takada, H. Hayashi, M. Hatemura, and T. Hirai, "Radiation dose reduction for 80-kVp pediatric CT using deep learning–based reconstruction: A clinical and phantom study," *American Journal of Roentgenology*, volume 219, number 2, pages 315–324, 2022.

[26] L. R. Koetzier, D. Mastrodicasa, T. P. Szczykutowicz, N. R. van der Werf, A. S. Wang, V. Sandfort, A. J. van der Molen, D. Fleischmann, and M. J. Willemink, "Deep learning image reconstruction for CT: Technical principles and clinical prospects," *Radiology*, volume 306, number 3, 2023.

[27] J. Hsieh, "Adaptive streak artifact reduction in computed tomography resulting from excessive x-ray photon noise," *Medical Physics*, volume 25, number 11, pages 2139–2147, 1998.

[28] M. Kachelrieß, O. Watzke, and W. A. Kalender, "Generalized multi-dimensional adaptive filtering for conventional and spiral single-slice, multi-slice, and cone-beam CT," *Medical Physics*, volume 28, number 4, pages 475–490, 2001.

[29] S. Gordic, F. Morsbach, B. Schmidt, T. Allmendinger, T. Flohr, D. Husarik, S. Baumueller, R. Raupach, P. Stolzmann, S. Leschka, T. Frauenfelder, and H. Alkadhi, "Ultralow-dose chest computed tomography for pulmonary nodule detection," *Investigative Radiology*, volume 49, number 7, pages 465–473, 2014.

[30] A. Hasegawa, K. Ichikawa, Y. Morioka, and H. Kawashima, "A tin filter's dose reduction effect revisited: Using the detectability index in low-dose computed tomography for the chest," *Physica Medica*, volume 99, pages 61–67, 2022.

[31] S. Schüle, K. Gärtner, D. Halt, M. Beer, and C. Hackenbroch, "Low-dose CT imaging of the pelvis in follow-up examinations – Significant dose reduction and impact of tin filtration," *Investigative Radiology*, volume 57, number 12, pages 789–801, 2022.

[32] K. Rajendran, B. A. Voss, W. Zhou, S. Tao, D. R. DeLone, J. I. Lane, J. M. Weaver, M. L. Carlson, J. G. Fletcher, C. H. McCollough, and S. Leng, "Dose reduction for sinus and temporal bone imaging using photon-counting detector CT with an additional tin filter," *Investigative Radiology*, volume 55, number 2, pages 91–100, 2020.

[33] P. Leyendecker, V. Faucher, A. Labani, V. Noblet, F. Lefebvre, P. Magotteaux, M. Ohana, and C. Roy, "Prospective evaluation of ultra-low-dose contrast-enhanced 100-kV abdominal computed tomography with tin filter: Effect on radiation dose reduction and image quality with a third-generation dual-source CT system," *European Radiology*, volume 29, number 4, pages 2107–2116, 2018.

[34] J. Y. Jeon, S.-W. Lee, Y. M. Jeong, and H. J. Baek, "The effect of tube voltage combination on image artefact and radiation dose in dual-source dual-energy CT: Comparison between conventional 80/140 kV and 80/150 kV plus tin filter for gout protocol," *European Radiology*, volume 29, number 3, pages 1248–1257, 2018.

[35] M. J. Willemink, M. Persson, A. Pourmorteza, N. J. Pelc, and D. Fleischmann, "Photon-counting CT: Technical principles and clinical prospects," *Radiology*, volume 289, number 2, pages 293–312, 2018.

[36] K. Taguchi and J. S. Iwanczyk, "Vision 20/20: Single photon counting x-ray detectors in medical imaging," *Medical Physics*, volume 40, number 10, page 100 901, 2013.

[37] P. M. Shikhaliev, T. Xu, and S. Molloi, "Photon counting computed tomography: Concept and initial results," *Medical Physics*, volume 32, number 2, pages 427–436, 2005.

[38] S. Kappler, F. Glasser, S. Janssen, E. Kraft, and M. Reinwand, "A research prototype system for quantum-counting clinical CT," in *SPIE Proceedings*, SPIE, 2010.

[39] A. Pourmorteza, R. Symons, A. Henning, S. Ulzheimer, and D. A. Bluemke, "Dose efficiency of quarter-millimeter photon-counting computed tomography," *Investigative Radiology*, volume 53, number 6, pages 365–372, 2018.

[40] J. von Spiczak, M. Mannil, B. Peters, T. Hickethier, M. Baer, A. Henning, B. Schmidt, T. Flohr, R. Manka, D. Maintz, and H. Alkadhi, "Photon counting computed tomography with dedicated sharp convolution kernels," *Investigative Radiology*, volume 53, number 8, pages 486–494, 2018.

[41] R. Gutjahr, A. F. Halaweish, Z. Yu, S. Leng, L. Yu, Z. Li, S. M. Jorgensen, E. L. Ritman, S. Kappler, and C. H. McCollough, "Human imaging with photon counting–based computed tomography at clinical dose levels," *Investigative Radiology*, volume 51, number 7, pages 421–429, 2016.

[42] L. Klein, S. Dorn, C. Amato, S. Heinze, M. Uhrig, H.-P. Schlemmer, M. Kachelrieß, and S. Sawall, "Effects of detector sampling on noise reduction in clinical photon-counting whole-body computed tomography," *Investigative Radiology*, volume 55, number 2, pages 111–119, 2020.

[43] M. Gies, W. A. Kalender, H. Wolf, C. Suess, and M. T. Madsen, "Dose reduction in CT by anatomically adapted tube current modulation. I. simulation studies," *Medical Physics*, volume 26, number 11, pages 2235–2247, 1999.

[44] W. A. Kalender, H. Wolf, and C. Suess, "Dose reduction in CT by anatomically adapted tube current modulation. II. phantom measurements," *Medical Physics*, volume 26, number 11, pages 2248–2253, 1999.

[45] H. Greess, H. Wolf, W. A. Kalender, and W. A. Bautz, "Dose reduction in CT by anatomically adapted tube current modulation: First patient studies," in *Advances in CT IV*, Springer Berlin Heidelberg, 1998, pages 35–40.

[46] H. Greess, H. Wolf, U. Baum, M. Lell, M. Pirkl, W. Kalender, and W. A. Bautz, "Dose reduction in computed tomography by attenuation-based on-line modulation of tube current: Evaluation of six anatomical regions," *European Radiology*, volume 10, number 2, pages 391–394, 2000.

[47] C. H. McCollough, M. R. Bruesewitz, and J. M. Kofler, "CT dose reduction and dose management tools: Overview of available options," *RadioGraphics*, volume 26, number 2, pages 503–512, 2006.

[48] P. Stenner and M. Kachelrieß, "Dual energy exposure control (DEEC) for computed tomography: Algorithm and simulation study," *Medical Physics*, volume 35, number 11, pages 5054–5060, 2008.

[49] M. Söderberg and M. Gunnarsson, "Automatic exposure control in computed tomography – an evaluation of systems from different manufacturers," *Acta Radiologica*, volume 51, number 6, pages 625–634, 2010.

[50] M. Doss, M. P. Little, and C. G. Orton, "Point/counterpoint: Low-dose radiation is beneficial, not harmful," *Medical Physics*, volume 41, number 7, page 070 601, 2014.

[51] D. R. Martin and R. C. Semelka, "Health effects of ionising radiation from diagnostic CT," *The Lancet*, volume 367, number 9524, pages 1712–1714, 2006.

[52] J. G. Fletcher, J. M. Kofler, J. A. Coburn, D. H. Bruining, and C. H. McCollough, "Perspective on radiation risk in CT imaging," *Abdominal Imaging*, volume 38, number 1, pages 22–31, 2012.

[53] C. W. Schmidt, "CT scans: Balancing health risks and medical benefits," *Environmental Health Perspectives*, volume 120, number 3, 2012.

[54] A. Ferrero, N. Takahashi, T. J. Vrtiska, A. E. Krambeck, J. C. Lieske, and C. H. McCollough, "Understanding, justifying, and optimizing radiation exposure for CT imaging in nephrourology," *Nature Reviews Urology*, volume 16, number 4, pages 231–244, 2019.

[55] M. P. Little, R. Wakeford, D. Borrego, B. French, L. B. Zablotska, M. J. Adams, R. Allodji, F. de Vathaire, C. Lee, A. V. Brenner, J. S. Miller, D. Campbell, M. S. Pearce, M. M. Doody, E. Holmberg, M. Lundell, S. Sadetzki, M. S. Linet, and A. B. de González, "Leukaemia and myeloid malignancy among people exposed to low doses (100 mSv) of ionising radiation during childhood: A pooled analysis of nine historical cohort studies," *The Lancet Haematology*, volume 5, number 8, pages 346–358, 2018.

[56] "Umweltradioaktivität und Strahlenbelastung Jahresbericht 2019," *Bundesministerium für Umwelt, Naturschutz und nukleare Sicherheit (BMU)*, 2019.

[57] F. Sauter, "Über die Bremsstrahlung schneller Elektronen," *Annalen der Physik*, volume 412, number 4, pages 404–412, 1934.

[58] D. M. Tucker, G. T. Barnes, and D. P. Chakraborty, "Semiempirical model for generating tungsten target x–ray spectra," *Medical Physics*, volume 18, number 3, pages 211–218, 1991.

[59] P. Schardt, J. Deuringer, J. Freudenberger, E. Hell, W. Knüpfer, D. Mattern, and M. Schild, "New x-ray tube performance in computed tomography by introducing the rotating envelope tube technology," *Medical Physics*, volume 31, number 9, pages 2699–2706, 2004.

[60] H. Bethe and W. Heitler, "On the stopping of fast particles and on the creation of positive electrons," *Proceedings of the Royal Society of London. Series A, Containing Papers of a Mathematical and Physical Character*, volume 146, number 856, pages 83–112, 1934.

[61] J. Strutt, "XV. On the light from the sky, its polarization and colour," *The London, Edinburgh, and Dublin Philosophical Magazine and Journal of Science*, volume 41, number 271, pages 107–120, 1871.

[62] J. Strutt, "LVIII. On the scattering of light by small particles," *The London, Edinburgh, and Dublin Philosophical Magazine and Journal of Science*, volume 41, number 275, pages 447–454, 1871.

[63] L. Rayleigh, "X. On the electromagnetic theory of light," *The London, Edinburgh, and Dublin Philosophical Magazine and Journal of Science*, volume 12, number 73, pages 81–101, 1881.

[64] L. Rayleigh, "XXXIV. On the transmission of light through an atmosphere containing small particles in suspension, and on the origin of the blue of the sky," *The London, Edinburgh, and Dublin Philosophical Magazine and Journal of Science*, volume 47, number 287, pages 375–384, 1899.

[65] F. H. Attix, *Introduction to Radiological Physics and Radiation Dosimetry*. Wiley, 1986.

[66] A. Einstein, "Über einen die Erzeugung und Verwandlung des Lichtes betreffenden heuristischen Gesichtspunkt," *Annalen der Physik*, volume 322, number 6, pages 132–148, 1905.

[67] A. H. Compton, "A quantum theory of the scattering of x-rays by light elements," *Physical Review*, volume 21, number 5, pages 483–502, 1923.

[68] A. Beer, "Bestimmung der Absorption des rothen Lichts in farbigen Flüssigkeiten," *Annalen der Physik und Chemie*, volume 162, number 5, pages 78–88, 1852.

[69] J. H. Lambert, *Photometria, sive de mensura et gradibus luminis, colorum et umbrae*. Eberhard Klett, 1760.

[70] W. Schlegel, C. P. Karger, and O. Jakel, Eds., *Medizinische Physik*, 1st edition. Springer Berlin Heidelberg, 2018.

[71] W. A. Kalender, W. Seissler, E. Klotz, and P. Vock, "Spiral volumetric CT with single-breath-hold technique, continuous transport, and continuous scanner rotation.," *Radiology*, volume 176, number 1, pages 181–183, 1990.

[72] T. Buzug, *Computed Tomography*. Springer Berlin Heidelberg, 2008.

[73] R. A. Brooks, "A quantitative theory of the Hounsfield unit and its application to dual energy scanning," *Journal of Computer Assisted Tomography*, volume 1, number 4, pages 487–493, 1977.

[74] W. A. Kalender, *Computed tomography*, 3rd edition. Publicis MCD Verlag, 2011.

[75] H. Krieger, *Grundlagen der Strahlungsphysik und des Strahlenschutzes*. Springer Berlin Heidelberg, 2019.

[76] "DIN 6809-7: Klinische Dosimetrie – Teil 7: Verfahren zur Ermittlung der Patientendosis in der Röntgendiagnostik," *Deutsches Institut für Normung*, 2003.

[77] "IEC 61223-3-5: Evaluation and routine testing in medical imaging departments – Part 3–5: Acceptance tests – Imaging performance of computed tomography x-ray equipment," *International Electrotechnical Commission (IEC)*, 2004.

[78] "IEC 60601-2-44: Medical electrical equipment – Part 2–44: Particular requirements for the basic safety and essential performance of x-ray equipment for computed tomography," *International Electrotechnical Commission (IEC)*, 2004.

[79] K. Treb and K. Li, "Accuracy of weighted CTDI in estimating average dose delivered to CTDI phantoms: An experimental study," *Medical Physics*, volume 47, number 12, pages 6484–6499, 2020.

[80] "Recommendations of the International Commission on Radiological Protection. ICRP Publication 60," *Annals of the ICRP*, volume 21, number 1-3, 1991.

[81] "Recommendations of the International Commission on Radiological Protection. ICRP Publication 27," *Annals of the ICRP*, volume 1, number 3, 1977.

[82] "Recommendations of the International Commission on Radiological Protection. ICRP Publication 103," *Annals of the ICRP*, volume 37, number 2-4, 2007.

[83] G. B. G, S. Golding, A. Jurik, M. Leonardi, E. Meerten, J. Geleijns, K. Jessen, W. Panzer, P. Shrimpton, and G. Tosi, "European guidelines on quality criteria for computed tomography: Eur 16262," *European Commission, Luxembourg*, 2000.

[84] P. C. Shrimpton, M. C. Hillier, M. A. Lewis, and M. Dunn, "National survey of doses from CT in the UK: 2003," *The British Journal of Radiology*, volume 79, number 948, pages 968–980, 2006.

[85] P. Shrimpton, "Assessment of patient dose in CT: European guidelines for multislice computed tomography," *International Electrotechnical Commission (IEC)*, 2004.

[86] J. Boone, K. Strauss, D. Cody, C. McCoullough, M. McNitt-Gray, and T. Toth, *TG 204 – Size specific dose estimates (SSDE) in pediatric and adult body CT examinations*. American Association of Physicists in Medicine, 2011.

[87] C. McCoullough, D. Bakalyar, M. Bostani, S. Brady, K. Boedecker, J. Boone, H. Chen-Mayer, O. Christianson, S. Leng, B. Li, M. McNitt-Gray, R. Nilsen, M. Supanich, and J. Wang, *TG 220 - Use of Water Equivalent Diameter for Calculating Patient Size and Size–Dependent Dose Estimates (SSDE) in CT*. American Association of Physicists in Medicine, 2014.

[88] C. J. Martin and S. Sookpeng, "Setting up computed tomography automatic tube current modulation systems," *Journal of Radiological Protection*, volume 36, number 3, R74–R95, 2016.

[89] J. N. Althén, "Automatic tube–current modulation in CT – A comparison between different solutions," *Radiation Protection Dosimetry*, volume 114, number 1-3, pages 308–312, 2005.

[90] L. Husmann, I. Valenta, O. Gaemperli, O. Adda, V. Treyer, C. A. Wyss, P. Veit-Haibach, F. Tatsugami, G. K. von Schulthess, and P. A. Kaufmann, "Feasibility of low-dose coronary CT angiography: First experience with prospective ECG-gating," *European Heart Journal*, volume 29, number 2, pages 191–197, 2007.

[91] X. Duan, J. Wang, J. A. Christner, S. Leng, K. L. Grant, and C. H. McCollough, "Dose reduction to anterior surfaces with organ-based tube-current modulation: Evaluation of performance in a phantom study," *American Journal of Roentgenology*, volume 197, number 3, pages 689–695, 2011.

[92] J. Wang, X. Duan, J. A. Christner, S. Leng, K. L. Grant, and C. H. McCollough, "Bismuth shielding, organ-based tube current modulation, and global reduction of tube current for dose reduction to the eye at head CT," *Radiology*, volume 262, number 1, pages 191–198, 2012.

[93] S. Taylor, D. E. Litmanovich, M. Shahrzad, A. A. Bankier, P. A. Gevenois, and D. Tack, "Organ-based tube current modulation: Are women's breasts positioned in the reduced-dose zone?" *Radiology*, volume 274, number 1, pages 260–266, 2015.

[94] A. Seidenfuss, A. Mayr, M. Schmid, M. Uder, and M. M. Lell, "Dose reduction of the female breast in chest CT," *American Journal of Roentgenology*, volume 202, number 5, W447–W452, 2014.

[95] L. Klein, C. Liu, J. Steidel, L. Enzmann, M. Knaup, S. Sawall, A. Maier, M. Lell, J. Maier, and M. Kachelrieß, "Patient-specific radiation risk-based tube current modulation for diagnostic CT," *Medical Physics*, volume 49, number 7, pages 4391–4403, 2022.

[96] L. Klein, L. Enzmann, A. Byl, C. Liu, S. Sawall, A. Maier, J. Maier, M. Lell, and M. Kachelrieß, "Organ-specific vs. patient risk-specific tube current modulation in thorax CT scans covering the female breast," in *7th International Conference on Image Formation in X-Ray Computed Tomography*, J. W. Stayman, Ed., SPIE, 2022.

[97] M. Kachelrieß, K. Sourbelle, and W. Kalender, "Empirical cupping correction: A first order rawdata precorrection for cone–beam computed tomography," *Medical Physics*, volume 33, number 5, pages 1269–1274, 2006.

[98] W. A. Kalender, H. Wolf, C. Suess, M. Gies, H. Greess, and W. A. Bautz, "Dose reduction in CT by on-line tube current control: Principles and validation on phantoms and cadavers," *European Radiology*, volume 9, number 2, pages 323–328, 1999.

[99] F. Geissler, R. Heiß, M. Kopp, M. Wiesmüller, M. Saake, W. Wuest, A. Wimmer, V. Prell, M. Uder, and M. S. May, "Personalized computed tomography – automated estimation of height and weight of a simulated digital twin using a 3d camera and artificial intelligence," *RöFo - Fortschritte auf dem Gebiet der Röntgenstrahlen und der bildgebenden Verfahren*, volume 193, number 04, pages 437–445, 2020.

[100] Y. Xu, H. Yan, L. Ouyang, J. Wang, L. Zhou, L. Cervino, S. B. Jiang, and X. Jia, "A method for volumetric imaging in radiotherapy using single x–ray projection," *Medical Physics*, volume 42, number 5, pages 2498–2509, 2015.

[101] P. Henzler, V. Rasche, T. Ropinski, and T. Ritschel, "Single–image tomography: 3D volumes from 2D x–rays," *arXiv*, number 1710.04867v2, 2017.

[102] X. Ying, H. Guo, K. Ma, J. Wu, Z. Weng, and Y. Zheng, "X2ct-GAN: Reconstructing CT from biplanar x-rays with generative adversarial networks," in *2019 IEEE/CVF Conference on Computer Vision and Pattern Recognition (CVPR)*, IEEE, 2019.

[103] L. Shen, W. Zhao, and L. Xing, "Patient-specific reconstruction of volumetric computed tomography images from a single projection view via deep learning," *Nature Biomedical Engineering*, volume 3, number 11, pages 880–888, 2019.

[104] D. F. Almeida, P. Astudillo, and D. Vandermeulen, "Three-dimensional image volumes from two-dimensional digitally reconstructed radiographs: A deep learning approach in lower limb CT scans," *Medical Physics*, volume 48, number 5, pages 2448–2457, 2021.

[105] S. Chen, X. Zhong, S. Hu, S. Dorn, M. Kachelrieß, M. Lell, and A. Maier, "Automatic multi-organ segmentation in dual-energy CT (DECT) with dedicated 3d fully convolutional DECT networks," *Medical Physics*, volume 47, number 2, pages 552–562, 2020.

[106] J. Maier, E. Eulig, S. Dorn, S. Sawall, and M. Kachelrieß, "Real–time patient–specific CT dose estimation using a deep convolutional neural network," in *IEEE Medical Imaging Conference Record*, 2018, pages M–03–178.

[107] J. Maier, L. Klein, E. Eulig, S. Sawall, and M. Kachelrieß, "Real-time estimation of patient-specific dose distributions for medical CT using the deep dose estimation," *Medical Physics*, volume 49, number 4, pages 2259–2269, 2022.

[108] K. Stierstorfer, A. Rauscher, J. Boese, H. Bruder, S. Schaller, and T. Flohr, "Weighted FBP – A simple approximate 3D FBP algorithm for multislice spiral CT with good dose usage for arbitrary pitch," *Physics in Medicine and Biology*, volume 49, pages 2209–2218, 2004.

[109] M. Kachelrieß, M. Knaup, and W. A. Kalender, "Extended parallel backprojection for standard 3D and phase–correlated 4D axial and spiral cone–beam CT with arbitrary pitch and 100% dose usage," *Medical Physics*, volume 31, number 6, pages 1623–1641, 2004.

[110] J. A. Nelder and R. Mead, "A simplex method for function minimization," *The Computer Journal*, volume 7, number 4, pages 308–313, 1965.

[111] P. M. Joseph, "An improved algorithm for reprojecting rays through pixel images," *IEEE Transactions on Medical Imaging*, volume 1, number 3, pages 192–196, 1982.

[112] O. Jimenez-del-Toro, H. Muller, M. Krenn, K. Gruenberg, A. A. Taha, M. Winterstein, I. Eggel, A. Foncubierta-Rodriguez, O. Goksel, A. Jakab, G. Kontokotsios, G. Langs, B. H. Menze, T. S. Fernandez, R. Schaer, A. Walleyo, M.-A. Weber, Y. D. Cid, T. Gass, M. Heinrich, F. Jia, F. Kahl, R. Kechichian, D. Mai, A. B. Spanier, G. Vincent, C. Wang, D. Wyeth, and A. Hanbury, "Cloud-based evaluation of anatomical structure segmentation and landmark detection algorithms: VISCERAL anatomy benchmarks," *IEEE Transactions on Medical Imaging*, volume 35, number 11, pages 2459–2475, 2016.

[113] Y. Tian, Y. Zhang, and H. Zhang, "Recent advances in stochastic gradient descent in deep learning," *Mathematics*, volume 11, number 3, 2023.

[114] D. C. Liu and J. Nocedal, "On the limited memory BFGS method for large scale optimization," *Mathematical Programming*, volume 45, number 1-3, pages 503–528, 1989.

[115] J. Yuan and A. Iusem, "Preconditioned conjugate gradient method for generalized least squares problems," *Journal of Computational and Applied Mathematics*, volume 71, number 2, pages 287–297, 1996.

[116] N. J. Walkington, "Nesterov's method for convex optimization," *SIAM Review*, volume 65, number 2, pages 539–562, 2023.

[117] B. Shahriari, K. Swersky, Z. Wang, R. P. Adams, and N. de Freitas, "Taking the human out of the loop: A review of bayesian optimization," *Proceedings of the IEEE*, volume 104, number 1, pages 148–175, 2016.

[118] W. Huda, K. M. Ogden, and M. R. Khorasani, "Effect of dose metrics and radiation risk models when optimizing CT x-ray tube voltage," *Physics in Medicine and Biology*, volume 53, number 17, pages 4719–4732, 2008.

[119] "Geschlechtsspezifische Unterschiede der Strahlenempfindlichkeit – epidemiologische, klinische und biologische Studien," *Stellungnahme der Strahlenschutzkommission*, 2009.

[120] N. Narendran, L. Luzhna, and O. Kovalchuk, "Sex difference of radiation response in occupational and accidental exposure," *Frontiers in Genetics*, volume 10, 2019.

[121] G. J. Gang, A. Mao, W. Wang, J. H. Siewerdsen, A. Mathews, S. Kwamoto, R. Levinson, and J. W. Stayman, "Dynamic fluence field modulation in computed tomography using multiple aperture devices," *Physics in Medicine and Biology*, volume 64, 105024 (13pp), 2019.

[122] S. M. Huck, G. S. K. Fung, K. Parodi, and K. Stierstorfer, "The z-sbDBA, a new concept for a dynamic sheet–based fluence field modulator in x–ray CT," *Medical Physics*, volume 47, number 10, pages 4827–4837, 2020.

[123] S. M. Huck, G. S. K. Fung, K. Parodi, and K. Stierstorfer, "Sheet–based dynamic beam attenuator — a novel concept for dynamic fluence field modulation in x–ray CT," *Medical Physics*, volume 46, number 12, pages 5528–5537, 2019.

List of publications

Journal articles with direct reference to the dissertation

[1] **L. Klein**, C. Liu, J. Steidel, L. Enzmann, M. Knaup, S. Sawall, A. Maier, M. Lell, J. Maier, and M. Kachelrieß, "Patient–specific radiation risk–based tube current modulation for diagnostic CT," *Medical Physics*, volume 49, number 7, pages 4391–4403, 2022.
This article received the **"Moses & Sylvia Greenfield Award"** for the best scientific paper on imaging in Medical Physics in 2022.

[2] J. Maier, **L. Klein**, E. Eulig, S. Sawall, and M. Kachelrieß, "Real–time estimation of patient–specific dose distributions for medical CT using the deep dose estimation," *Medical Physics*, volume 49, number 4, pages 2259–2269, 2022.

Conference contributions with direct reference to the dissertation

[1] **L. Klein**, C. Liu, J. Steidel, L. Enzmann, S. Sawall, J. Maier, A. Maier, M. Lell, and M. Kachelrieß, "Risk–minimizing tube current modulation (riskTCM) for CT – potential dose reduction across different tube voltages," *Proceedings of the European Congress of Radiology (ECR)*, 2022.
This contribution was awarded the "**Best Research Presentation Abstract Award** within the topic Physics in Medical Imaging" at the ECR 2022.

[2] **L. Klein**, L. Enzmann, A. Byl, C. Liu, S. Sawall, A. Maier, J. Maier, M. Lell, and M. Kachelrieß, "Organ–specific vs. patient risk–specific tube current modulation in thorax CT scans covering the female breast," in *7th International Conference on Image Formation in X–Ray Computed Tomography*, J. W. Stayman, Ed., SPIE, 2022.

[3] **L. Klein**, E. Baader, A. Byl, C. Liu, S. Sawall, A. Maier, M. Lell, J. Maier, and M. Kachelrieß, "Potential CT radiation dose reduction to the female breast by a novel risk–minimizing tube current modulation," *Proceedings of the 108th Scientific Assembly and Annual Meeting of the Radiological Society of North America (RSNA)*, 2022.

[4] **L. Klein**, C. Liu, J. Steidel, S. Sawall, A. Maier, M. Lell, J. Maier, and M. Kachelrieß, "A novel CT tube current modulation technique that minimizes patient risk," *Proceedings of the 107th Scientific Assembly and Annual Meeting of the Radiological Society of North America (RSNA)*, 2021.

[5] E. Baader, **L. Klein**, S. Sawall, J. Maier, and M. Kachelrieß, "CT tube current and tube voltage modulation to minimize the patient's radiation risk," *Proceedings of the European Congress of Radiology (ECR)*, 2023.

[6] C. Liu, F. Denzinger, L. Folle, J. Qiu, **L. Klein**, J. Maier, M. Kachelrieß, M. Lell, and A. Maier, "Whole–body multi–organ segmentation using anatomical attention," *Proceedings of the 20th International Symposium on Biomedical Imaging*, 2023.

[7] J. Maier, **L. Klein**, S. Sawall, C. Liu, A. Maier, and M. Kachelrieß, "Radiation risk minimizing tube current modulation (rmTCM) for x–ray computed tomography," *Proceedings of the European Congress of Radiology (ECR)*, 2021.

[8] C. Liu, Y. Huang, J. Maier, **L. Klein**, M. Kachelrieß, and A. Maier, "Robustness investigation on deep learning CT reconstruction for real–time dose optimization," *Proceedings of the 2020 Virtual IEEE Nuclear Science Symposium and Medical Imaging Conference*, 2020.

[9] J. Maier, **L. Klein**, and M. Kachelrieß, "How low can CT dose go? Options for automatic exposure control (AEC)," *Proceedings of the 62nd Annual Meeting of the AAPM*, 2020.

Journal articles without direct reference to the dissertation

[1] J. A. Peña, **L. Klein**, J. Maier, T. Damm, H.-P. Schlemmer, K. Engelke, C.-C. Glüer, M. Kachelrieß, and S. Sawall, "Dose–efficient assessment of trabecular microstructure using ultra–high–resolution photon–counting CT," *Zeitschrift für Medizinische Physik*, volume 32, number 4, pages 403–416, 2022.

[2] E. Wehrse, **L. Klein**, L. Rotkopf, W. Stiller, M. Finke, G. Echner, C. Glowa, S. Heinze, C. Ziener, H.-P. Schlemmer, M. Kachelrieß, and S. Sawall, "Ultrahigh resolution whole body photon counting computed tomography as a novel versatile tool for translational research from mouse to man," *Zeitschrift für Medizinische Physik*, 2022.

[3] S. Sawall, C. Amato, **L. Klein**, E. Wehrse, J. Maier, and M. Kachelrieß, "Toward molecular imaging using spectral photon–counting computed tomography?" *Current Opinion in Chemical Biology*, volume 63, pages 163–170, 2021.

[4] A. Byl, **L. Klein**, S. Sawall, S. Heinze, H.-P. Schlemmer, and M. Kachelrieß, "Photon–counting normalized metal artifact reduction (NMAR) in diagnostic CT," *Medical Physics*, volume 48, number 7, pages 3572–3582, 2021.

[5] S. Sawall, **L. Klein**, E. Wehrse, L. T. Rotkopf, C. Amato, J. Maier, H.-P. Schlemmer, C. H. Ziener, S. Heinze, and M. Kachelrieß, "Threshold–dependent iodine imaging and spectral separation in a whole–body photon–counting CT system," *European Radiology*, volume 31, number 9, pages 6631–6639, 2021.

[6] E. Wehrse, S. Sawall, **L. Klein**, P. Glemser, S. Delorme, H.-P. Schlemmer, M. Kachelrieß, M. Uhrig, C. H. Ziener, and L. T. Rotkopf, "Potential of ultra–high–resolution photon-counting CT of bone metastases: Initial experiences in breast cancer patients," *Nature Partner Journals (npj) Breast Cancer*, volume 7, number 1, 2021.

[7] E. Wehrse, **L. Klein**, L. T. Rotkopf, W. L. Wagner, M. Uhrig, C. P. Heußel, C. H. Ziener, S. Delorme, S. Heinze, M. Kachelrieß, H.-P. Schlemmer, and S. Sawall, "Photon–counting detectors in computed tomography: From quantum physics to clinical practice," *Der Radiologe*, volume 61, number S1, pages 1–10, 2021.

[8] C. Amato, **L. Klein**, E. Wehrse, L. T. Rotkopf, S. Sawall, J. Maier, C. H. Ziener, H.-P. Schlemmer, and M. Kachelrieß, "Potential of contrast agents based on high–Z elements for contrast–enhanced photon–counting computed tomography," *Medical Physics*, volume 47, number 12, pages 6179–6190, 2020.

Conference contributions without direct reference to the dissertation

[1] **L. Klein**, E. Wehrse, C. Amato, C. Ziener, M. Uhrig, S. Heinze, H.-P. Schlemmer, M. Kachelrieß, and S. Sawall, "Context–sensitive ultra high resolution bone imaging in whole body photon–counting CT," *Proceedings of the European Congress of Radiology (ECR)*, 2020.

[2] **L. Klein**, J. Hardt, A. Byl, E. Wehrse, S. Heinze, M. Uhrig, H.-P. Schlemmer, M. Kachelrieß, and S. Sawall, "Kernel considerations for high resolution photon–counting CT: Dose reduction versus spatial resolution," *Proceedings of the European Congress of Radiology (ECR)*, 2020.

[3] **L. Klein**, E. Wehrse, L. Rotkopf, C. Amato, J. Maier, H.-P. Schlemmer, C. H. Ziener, S. Heinze, M. Kachelrieß, and S. Sawall, "Strategien zur Dosisoptimierung in der photonenzählenden Ganzkörper–Computertomographie," *Abstractband der 51. Jahrestagung der Deutschen Gesellschaft für Medizinische Physik*, 2020.

[4] M. Fix, Y. Kayser, **L. Klein**, J. Maier, L. T. Rotkopf, H.-P. Schlemmer, S. O. Schönberg, M. Kachelrieß, and S. Sawall, "Clinical photon–counting CT: The small pixel effect and its implications for dose reduction," *Proceedings of the European Congress of Radiology (ECR)*, 2023.

[5] S. Sawall, **L. Klein**, C. Amato, L. Rotkopf, C. H. Ziener, H.-P. Schlemmer, and M. Kachelrieß, "Iron quantification in a dual–source photon-counting CT system with up to four energy bins," *Proceedings of the European Congress of Radiology (ECR)*, 2022.

[6] J. Pena, **L. Klein**, T. Damm, H.-P. Schlemmer, K. Engelke, C. C. Glueer, M. Kachelrieß, and S. Sawall, "Dose–efficient assessment of trabecular microstructure using whole–body photon–counting CT," *Proceedings of the 107th Scientific Assembly and Annual Meeting of the Radiological Society of North America (RSNA)*, 2021.

[7] J. Steidel, **L. Klein**, J. Maier, S. Sawall, and M. Kachelrieß, "Beyond iodine: Dose reduction potential with patient–specific prefiltration in hafnium–enhanced CT scans with energy integrating and photon counting detectors," *Proceedings of the 107th Scientific Assembly and Annual Meeting of the Radiological Society of North America (RSNA)*, 2021.

[8] S. Sawall, **L. Klein**, E. Wehrse, C. Amato, J. Maier, C. H. Ziener, H.-P. Schlemmer, S. Heinze, and M. Kachelrieß, "Dose reduction in photon–counting CT by ultra–high resolution acquisitions compared to today's iterative reconstructions: Combined benefits of the "iodine effect" and the "small pixel effect"," *Proceedings of the European Congress of Radiology (ECR)*, 2021.

[9] E. Wehrse, **L. Klein**, L. T. Rotkopf, W. L. Wagner, A. Tavakoli, C. P. Heußel, P. Mayer, C. H. Ziener, S. Delorme, M. Kachelrieß, H.-P. Schlemmer, and S. Sawall, "Subsolid nodule detection in low–dose photon–counting chest CT," *Proceedings of the European Congress of Radiology (ECR)*, 2021.

[10] J. Steidel, **L. Klein**, J. Maier, S. Sawall, and M. Kachelrieß, "Dose reduction potential using patient–specific prefilters in single–energy CT within the performance limits of current diagnostic CT systems," *Proceedings of the European Congress of Radiology (ECR)*, 2021.

[11] P. Trapp, A. Byl, **L. Klein**, S. Heinze, H.-P. Schlemmer, S. Sawall, and M. Kachelrieß, "Bin–combination-based noise reduction for metal artifact reduction in photon counting CT," *Proceedings of the European Congress of Radiology (ECR)*, 2021.
This contribution was awarded the "**Best Research Presentation Abstract Award** within the topic Physics in Medical Imaging" at the ECR 2021.

[12] J. Hardt, A. Byl, **L. Klein**, J. Maier, H.-P. Schlemmer, E. Wehrse, L. Rotkopf, C. H. Ziener, S. Heinze, M. Kachelrieß, and S. Sawall, "Erkennbarkeit von Niedrigkontraststrukturen in der photonenzählenden Ganzkörper Computertomographie – Eine Phantomstudie," *Abstractband der 51. Jahrestagung der Deutschen Gesellschaft für Medizinische Physik*, 2020.
This abstract was selected for the **Young Investigator Forum** at the 51th Annual Meeting of the German Physical Society (DGMP 2020).

[13] S. Heinze, K. Yen, A. Tsaklakidis, **L. Klein**, A. Byl, M. Kachelrieß, H.-P. Schlemmer, and S. Sawall, "Forensische Bildgebung 2.0," *Tagungsband der 99. Jahrestagung der Deutschen Gesellschaft für Rechtsmedizin*, 2020.

[14] S. Sawall, **L. Klein**, C. Amato, E. Wehrse, J. Maier, H.-P. Schlemmer, C. Ziener, S. Heinze, and M. Kachelrieß, "Threshold–dependent dual energy performance and spectral separation in a clinical whole-body photon–counting CT," *Proceedings of the European Congress of Radiology (ECR)*, 2020.

[15] E. Wehrse, **L. Klein**, M. Kachelrieß, H.-P. Schlemmer, C. Ziener, M. Wennmann, S. Delorme, M. Uhrig, and S. Sawall, "First experience in man with an ultra–high resolution whole–body photon–counting CT for oncologic imaging," *Proceedings of the European Congress of Radiology (ECR)*, 2020.

[16] A. Byl, J. Hardt, **L. Klein**, E. Wehrse, H.-P. Schlemmer, S. Heinze, M. Uhrig, S. Sawall, and M. Kachelrieß, "Dedicated metal artifact reduction for photon counting CT," *Proceedings of the European Congress of Radiology (ECR)*, 2020.

[17] E. Wehrse, S. Petra, **L. Klein**, L. Rotkopf, C. H. Ziener, M. Kachelrieß, H.-P. Schlemmer, and S. Sawall, "Structured regularization for material decomposition of photon counting CT data using collaborative total variation," *6th International Meeting on Imaging Formation in X–Ray Computed Tomography (CT–Meeting)*, 2020.

[18] C. Amato, **L. Klein**, J. Maier, S. Sawall, N. Gehrke, D. Franke, S. Gkoumas, T. Thüring, A. Briel, C. Brönnimann, and M. Kachelrieß, "Decomposition of multiple contrast agents in photon–counting micro–CT: Iodine and bismuth," *6th International Meeting on Imaging Formation in X–Ray Computed Tomography (CT–Meeting)*, 2020.

[19] A. Byl, **L. Klein**, J. Hardt, S. Sawall, H.-P. Schlemmer, S. Heinze, and M. Kachelrieß, "Metal artifact reduction in photon counting CT using pseudo-monochromatic images," *6th International Meeting on Imaging Formation in X–Ray Computed Tomography (CT–Meeting)*, 2020.

Acknowledgments

An dieser Stelle möchte ich mich bei allen bedanken, die mich während meiner Promotion unterstützt haben:

Prof. Dr. Jürgen Hesser für die Übernahme des Erstgutachtens, die Hilfsbereitschaft und die Betreuung im Rahmen der Graduiertenschule.

Prof. Dr. Marc Kachelrieß für die Möglichkeit in seiner Arbeitsgruppe zu promovieren, die wissenschaftliche Betreuung meiner Promotion und die Übernahme des Zweitgutachtens.

Prof. Dr. Michael Lell, Prof. Dr. Andreas Maier und Chang Liu für die erfolgreiche Zusammenarbeit während des DFG Projekts "CT-Belichtungsautomatik mit patientenspezifischer Echtzeitberechnung der Dosisverteilung durch neuronale Netze und Minimierung der effektiven Dosis" und für die zahlreichen hilfreichen Diskussionen.

Weiterhin gilt mein Dank auch der Deutschen Forschungsgemeinschaft, die durch ihre finanzielle Förderung des Forschungsprojekts, die Arbeit erst ermöglicht hat.

Allen Kollegen aus der Arbeitsgruppe „Röntgenbildgebung und Computertomographie" für die gute Zusammenarbeit und die angenehme Arbeitsatmosphäre. Besonderer Dank gilt dabei Dr. Joscha Maier und Dr. Stefan Sawall für die fachliche Unterstützung und Hilfsbereitschaft.

Prof. Dr. Matthias Bartelmann und Prof. Dr. Norbert Frank für die Übernahme der mündlichen Prüfung.

Zu guter Letzt möchte ich mich auch besonders bei meiner Familie für die andauerende Unterstützung während meines Studiums bedanken.

I hereby assure, that I composed this work by myself and did not use any other than the listed resources.

Heidelberg, September 1, 2023